

The University of Nottingham

UNITED KINGDOM · CHINA · MALAYSIA

Department of Electrical and Electronic Engineering

Faculty of Engineering

Design of Short Time Duty Permanent Magnet Electrical Machines

Claudio Sciascera

Submitted to the University of Nottingham for the degree of Doctor of Philosophy,

September 2017

ABSTRACT

Recent progresses of the aviation industry toward the More Electric Aircraft have increased the demand for high performance Electro-Mechanical Actuators. In this context, extensive research is being conducted for the design of high torque density electrical machines able to meet the high reliability standards required. For low-rate duty applications (e.g. landing gear extension, retraction and steering; flight control surfaces), this can be achieved also by exploiting the characteristic that the motor does not reach a thermal equilibrium. In this work, the principal aim is to investigate the main limits in the design of low-rate duty, high torque density electrical machines and to propose methods for the improvement of the performance and reliability of such machines. This is achieved through detailed analysis of the motor design issues, of its thermal performance, as well as of the most critical ageing phenomena during operations. A structured design procedure for surface mounted permanent magnet machines is presented. A novel thermal model which features high accuracy and low computational cost is presented. A novel winding insulation lifetime consumption model which relates the winding time to failure to its temperature profile during operations is proposed. As vessel to address the thesis' objectives, a fault tolerant electrical machine, which is an integral part of an actuator for the extension and retraction of a helicopter landing gear, is designed, built and experimentally tested. The tests are aimed at validating the design procedure and the thermal model accuracy. A series of accelerated ageing tests is conducted on samples of the motor windings, which serve to analyse the insulation degradation processes under different stress levels and to validate the proposed lifetime consumption model.

A nonna Maria

TABLE OF CONTENTS

Abstract iii

Table of Contents v

List of Figures ix

List of Tables xv

Acronyms xvii

Glossary of Symbols xix

Chapter 1 Introduction ..... - 1 -

1.1 Introduction ..... - 2 -

1.2 The SPEARE project overview ..... - 3 -

1.3 The electrical machine ..... - 4 -

1.4 Thesis's aim and objectives ..... - 5 -

1.5 Thesis's structure ..... - 7 -

1.6 List of publications related to this work ..... - 9 -

Chapter 2 Literature review ..... - 10 -

2.1 Electro-Mechanical Actuators for Aerospace Applications ..... - 11 -

2.2 Fault tolerant electrical machines ..... - 14 -

2.2.1 Considerations on PMAC and SR machines ..... - 14 -

2.2.2 PMAC machines ..... - 16 -

2.3 Electrical machines for Short Time Duty Applications ..... - 19 -

2.4 Thermal modelling techniques ..... - 21 -

2.5 Reliability of electrical machines ..... - 25 -

2.5.1 Mechanical failures ..... - 25 -

2.5.2 Electrical faults ..... - 26 -

2.6 Conclusions ..... - 29 -

Chapter 3 SMPM motor for a short time duty application ..... - 31 -

3.1 The helicopter's landing gear electro-mechanical actuator specifications- 32 -

3.2 Trade-off study for the weight minimization of the electro-mechanical actuator ..... - 36 -

3.2.1 The motor weight ..... - 36 -

3.2.2 The motor inductance ..... - 40 -

3.2.3 The system weight ..... - 41 -

3.3 Design of the SMPM motor ..... - 43 -

3.3.1 Fault tolerance capability of the motor ..... - 43 -

3.3.2 SMPM motor design considerations ..... - 46 -

3.3.3 Slot current density maximization ..... - 49 -

3.4 Performance analysis of the SMPM motor ..... - 52 -

3.5 Experimental validation of SMPM motor's performance ..... - 62 -

3.5.1 The test setup ..... - 62 -

3.5.2 The back-emf ..... - 63 -

3.5.3 The torque constant ..... - 65 -

3.5.4 Short circuit conditions ..... - 66 -

3.5.5 Comparison between simulation and experimental results ..... - 68 -

3.6 Conclusions ..... - 69 -

Chapter 4 Thermal Modelling of Electrical Machines ..... - 72 -

4.1 Introduction ..... - 73 -

4.2 The Lumped Parameter Thermal Network model ..... - 73 -

4.2.1 Developing the LPTN ..... - 74 -

4.2.2 Thermal network parameters definition ..... - 79 -

4.2.3 SMPM machine operating temperature estimations ..... - 83 -

4.3 Experimental evaluation of SMPM thermal performance ..... - 86 -

4.3.1 Preliminary thermal experiments results ..... - 87 -
4.3.2 Thermal evaluation during operations ..... - 93 -
4.4 LPTN parameters fine tuning ..... - 98 -
4.4.1 The tuning procedure ..... - 99 -
4.4.2 Tuning of the proposed LPTN ..... - 102 -
4.4.3 Performance of the tuned LPTN ..... - 107 -
4.5 Low Computational Cost Thermal Model ..... - 111 -
4.5.1 LPTN Analytical Solution ..... - 112 -
4.5.2 Low Computational Cost Thermal Model ..... - 118 -
4.5.3 Lower order models ..... - 123 -
4.6 Conclusions ..... - 129 -
Chapter 5 Lifetime consumption of windings electrical insulation ..... - 132 -
5.1 Winding electrical insulation lifetime prediction model ..... - 134 -
5.1.1 Literature review on ageing models ..... - 135 -
5.1.2 Multi-stress Lifetime Consumption model for the winding electrical insulation of the SMPM motor ..... - 138 -
5.1.3 Evaluation of the lifetime consumption model ..... - 145 -
5.2 Accelerated ageing tests for the tuning of the lifetime consumption model parameters ..... - 149 -
5.2.1 Accelerated ageing tests' review ..... - 150 -
5.2.2 Thermal cycling accelerated ageing test for the tuning of the lifetime consumption model ..... - 158 -
5.2.3 Tuning of the lifetime consumption model on the base of the accelerated ageing tests results ..... - 171 -
5.2.4 Sensitivity analysis of the tuned parameters of the lifetime consumption model ..... - 180 -
5.3 Applications of the lifetime consumption model ..... - 188 -

5.3.1 Online maintenance scheduling ..... - 189 -

5.3.2 Motor rating using the lifetime consumption model..... - 191 -

5.4 Conclusions..... - 197 -

Chapter 6 Conclusions..... - 200 -

6.1 Summary of the undertaken work..... - 200 -

6.2 Major contributions to research ..... - 204 -

6.3 Future works ..... - 205 -

References..... - 208 -

Figure 1.1: Diagram of the rotary EMA of the landing gear for the Speare project..- 3 -

Figure 2.1: Architecture of an EHA (left) and of an EMA (right).....- 12 -

Figure 2.2: Cross section of SMPM (left) and IPM (right) rotors. .....- 16 -

Figure 2.3: Load and motor temperature profiles for the case of short-time duty (left) and intermittent duty (right) [50] .....- 19 -

Figure 3.1: Architecture of the EMA for the retraction and extension of the helicopter landing gear. .....- 34 -

Figure 3.2: Speed profile at the pivot during the retraction of the landing gear. .....- 35 -

Figure 3.3: Torque profile at the pivot during the retraction of the landing gear. ...- 35 -

Figure 3.4: d-axis inductance value for different gear ratios and for different DC-Link voltages. (a): 28VDC case, (b): 270VDC case. .....- 41 -

Figure 3.5: EMA weight estimation for each combination of DC-Link voltage and gear ratios considered for the trade-off study. .....- 42 -

Figure 3.6: Cross section of the motor designed and phases distribution. .....- 47 -

Figure 3.7: Scheme of the design procedure for the slot current density maximization. .....- 50 -

Figure 3.8: B-H curve for M270-35A material.....- 51 -

Figure 3.9: Flux density distribution (shaded) and flux paths in the motor under no load conditions. .....- 54 -

Figure 3.10: Flux density distribution (shaded) and flux paths in the motor when one star is fed with 3.12 A. .....- 54 -

Figure 3.11: Flux density distribution (shaded) and flux paths in the motor when both stars are fed with 3.12 A. .....- 55 -

Figure 3.12: back-emf in one three-phase star at rated speed (2500 rpm). .....- 55 -

Figure 3.13: d-axis and q-axis inductances vs phase current for one three-phase star. .....- 57 -

Figure 3.14: Torque vs q-axis current curve for one three-phase star. .....- 58 -

Figure 3.15: One three-phase short circuit steady-state current vs rotor speed. .....- 60 -

Figure 3.16: Braking torque due to one three-phase short circuit vs rotor speed. ...- 60 -

Figure 3.17: Test bench used for testing the motor of the EMA. .....- 62 -

Figure 3.18: Comparison between experimental (continuous line) and finite element (dashed line) line-to-neutral back-emf when the rotor speed is equal to 2500 rpm. .....- 64 -

Figure 3.19: Comparison between experimental (red) and finite element (blue) FFTs of the line-to-neutral back-emf at 2500 rpm.....- 65 -

Figure 3.20: Experimental (green dots) and finite element (blue line) torque vs. q-axis current curve for one three-phase star. .....- 66 -

Figure 3.21: Analytical (blue line) and experimental (orange dots) one three-phase short circuit steady-state current vs. rotor speed. .....- 68 -

Figure 3.22: Analytical (blue line) and experimental (orange dots) one three-phase short circuit steady-state braking torque vs. rotor speed. .....- 68 -

Figure 4.1: Schematic of the LPTN which models the SMPM under investigation. .....- 76 -

Figure 4.2: Correlation between LPTN nodes and portion of motor interested. .....- 78 -

Figure 4.3: Motor losses distribution during operations.....- 79 -

Figure 4.4: DC Current profiles applied for the evaluation of the motor temperature during operations.....- 85 -

Figure 4.5: Winding temperature predicted by LPTN for the three operating modes of the SMPM motor designed.....- 86 -

Figure 4.6: Winding temperature profiles for the SMPM at 2500 rpm when 1.41A AC are applied (red) and for the static motor when 1A DC is applied.....- 89 -

Figure 4.7: Difference between the two temperature profiles depicted in Figure 4.6. .....- 89 -

Figure 4.8: Winding temperature profiles for the SMPM at 2500 rpm when 1.41A AC are applied (red) and for the static motor when 1A DC is applied, during the first 60 seconds transient. .....- 90 -

Figure 4.9: Winding temperature profiles for the SMPM at 2500 rpm when 0.71A AC are applied (red) and for the static motor when 0.5A DC is applied. .....- 91 -

Figure 4.10: Difference between the two temperature profiles depicted in Figure 4.9. ..... - 91 -

Figure 4.11: Winding temperature for the star fed with 2.2A DC and for the disconnected star. ..... - 93 -

Figure 4.12: Temperature rise in the open star when a current is applied to the other star. ..... - 93 -

Figure 4.13: Espec Test Chamber employed for simulating operative ambient temperature. ..... - 94 -

Figure 4.14: SMPM motor placed in the test chamber. ..... - 95 -

Figure 4.15: Comparison of winding temperature rise for the case of motor placed on the wooden plate and of motor attached to the rig endplate. ..... - 96 -

Figure 4.16: Experimental winding temperature profiles for the three operating modes considered, when the motor is placed in the test chamber at 70 °C. ..... - 97 -

Figure 4.17: SMPM motor test setup for the temperature profiles acquisitions to be used as input of the LPTN critical parameters tuning procedure. ..... - 104 -

Figure 4.18: Best solutions found using the SQP algorithm for the corrective factors of $Rel20$, keq, hag and ceq. ..... - 105 -

Figure 4.19: Best solutions found using the SQP algorithm for the corrective factors of $hext$, $kiron$ and $chous$. ..... - 105 -

Figure 4.20: Measured winding temperatures (m.) compared to the temperatures predicted by the tuned LPTN for the case of DC current equal to 0.4, 0.5, 0.9 and 1A. ..... - 108 -

Figure 4.21: Test DC current applied for investigating thermal model's performance. ..... - 109 -

Figure 4.22: Measured and predicted using the LPTN winding temperature, when three consecutive steps of current equal to 0.9, 0.7 and 0A are applied to the phases of the SMPM motor. ..... - 110 -

Figure 4.23: Comparison between the winding temperature experimental measurements and the LPTN predictions, for the case of DC current applied equal to 1.5,, 2.2, 3.6 and 4.2A. ..... - 110 -

Figure 4.24: 7-node LPTN (on the right) equivalent to the thermal network depicted in Figure 4.1 (on the left).....- 113 -

Figure 4.25: Last four elements of the diagonal of K respect to current I normalized by their value for I=0.....- 119 -

Figure 4.26: Measured winding temperature and predicted temperature using second and third order thermal models. .....- 124 -

Figure 4.27: 3-node LPTN equivalent circuit.....- 126 -

Figure 4.28: Measured winding temperatures (m.) compared to the temperatures predicted by the 3rd order analytical model for current I equal to 0.4, 0.5, 0.9 and 1A DC.....- 127 -

Figure 4.29: Measured winding temperature and temperature predicted with the 3rd order analytical model for three consecutive current steps of 0.9, 0.7 and 0A DC. .....- 127 -

Figure 5.1: Generic winding temperature profile during one duty cycle.....- 146 -

Figure 5.2: Lifetime vs. duty cycle period, for different values of k, when N is equal to 1 and the temperature cycle temperature range is fixed. .....- 147 -

Figure 5.3: Lifetime vs. duty cycle period, for different values of N,, when k is equal to 1 and the temperature cycle temperature range is fixed. .....- 148 -

Figure 5.4: Average endurance of the Magnebond CB-180 magnetic wires for different temperatures applied [168]. .....- 161 -

Figure 5.5: One specimen of the winding tested through accelerated thermo-mechanical ageing tests, composed of two coils wound together. .....- 162 -

Figure 5.6: Specimens placed in the sealed box for the accelerated ageing test....- 163 -

Figure 5.7: Setup of the accelerated ageing tests.....- 166 -

Figure 5.8: Accelerated ageing tests scheme. .....- 166 -

Figure 5.9: Specimens temperature acquisition when the constant target temperature is equal to 265 °C.....- 168 -

Figure 5.10: Temperature profile for the case of thermal cycling accelerated ageing test, where the dotted red lines represent the temperature limits $Tmin$ and $Tmax$.....- 169 -

Figure 5.11: Time to failure of the specimens aged at constant temperature equal to 260 °C.....- 172 -

Figure 5.12: Time to failure of the specimens aged at constant temperature equal to 240 °C.....- 172 -

Figure 5.13: Temperature profile of the specimens during the first accelerated ageing test for the tuning of the free parameters k and N, with an applied DC current equal to 4.5 A. .....- 174 -

Figure 5.14: Time to failure of the specimens aged under thermal and thermo-mechanical stress applying the temperature profile of Figure 5.12.....- 175 -

Figure 5.15: Temperature profile of the specimens during the first accelerated ageing test for the tuning of the free parameters k and N, with an applied DC current equal to 8 A. .....- 176 -

Figure 5.16: Time to failure of the specimens aged under thermal and thermo-mechanical stress applying the temperature profile of Figure 5.14.....- 176 -

Figure 5.17: two sets of pairs (k, N) for which the lifetime model predictions and the experimental results match.....- 178 -

Figure 5.18: Temperature profile of the specimens during one cycle for the accelerated ageing test conducted for validating the lifetime consumption model.....- 179 -

Figure 5.19: Time to failure of the specimens aged under thermal and thermo-mechanical stress applying the temperature profile of Figure 5.17.....- 179 -

Figure 5.20: Percentage error of the lifetime prediction for different values of the parameter k respect to the lifetime calculated with the tuned parameters, for the temperature profile of Figure 5.12.....- 182 -

Figure 5.21: Percentage error of the lifetime prediction for different values of the parameter N respect to the lifetime calculated with the tuned parameters, for the temperature profile of Figure 5.12.....- 182 -

Figure 5.22: Percentage error of the lifetime prediction for different values of the parameter k respect to the lifetime calculated with the tuned parameters, for the temperature profile of Figure 5.14.....- 183 -

Figure 5.23: Percentage error of the lifetime prediction for different values of the parameter N respect to the lifetime calculated with the tuned parameters, for the temperature profile of Figure 5.14.....- 183 -

Figure 5.24: Temperature cycle considered for the sensitivity analysis of the lifetime prediction model for the case of operating stress levels. ..... - 185 -

Figure 5.25: Percentage error of the lifetime prediction for different values of the parameter k respect to the lifetime calculated with the tuned parameters, for the temperature profile of Figure 5.23. ..... - 186 -

Figure 5.26: Percentage error of the lifetime prediction for different values of the parameter N respect to the lifetime calculated with the tuned parameters, for the temperature profile of Figure 5.23. ..... - 186 -

Figure 5.27: Percentage error of the lifetime prediction for different values of the parameters k and N respect to the lifetime calculated with the tuned parameters, for the temperature profile of Figure 5.23. ..... - 187 -

Figure 5.28: Winding temperature profiles calculated with the LPTN for the three motor operating modes. ..... - 193 -

Figure 5.29: Winding temperature profiles calculated with the LPTN for the three motor operating modes for the case of motor rated for 20,000 hours lifetime. ..... - 196 -

Figure 5.30: Percentage motor power rating increase for different lifetime constraints of the emergency operating modes. ..... - 197 -

Table 2.1: Winding factor for different combinations of number of slots and pole pairs, allowing the realization of a three-phase machine with balanced concentrated winding [45]. - 18 -

Table 3.1: EMA specifications for the landing gear application. - 33 -

Table 3.2: Torque to be produced by the electric motor for each considered combination of gear ratios. - 37 -

Table 3.3: Motor shaft rotational speed for each considered combination of gear ratios. - 37 -

Table 3.4: Gearbox weight estimation for each considered combination of gear ratios. - 38 -

Table 3.5: Motor weight for each gear ratios combination. - 39 -

Table 3.8: Main motor geometrical parameters. - 48 -

Table 3.9: Main geometrical dimensions of the SMPM motor. - 52 -

Table 3.10: Main motor quantities under healthy operating conditions. - 53 -

Table 3.11: Values of the parameters derived with the Finite Element method for the analytical computation of the short circuit current and braking torque. - 61 -

Table 3.12: Comparison between simulations and experimental results. - 69 -

Table 4.1: Meaning of the symbols in Figure 4.1. - 77 -

Table 4.2: Thermal properties of the motor's materials. - 81 -

Table 4.3: Comparison between predicted and experimental winding temperatures during the three application's duty cycles. - 98 -

Table 4.4: Optimized value for the critical parameters - 107 -

Table 4.5: Maximum absolute temperature prediction error for each DC current considered - 111 -

Table 4.6: Values of the resistances [°C/W] and capacitances [J/°C] of the 7-node thermal network. - 113 -

Table 4.7: Mean relative and maximum absolute winding temperature prediction error with the LPTN and the LCC model, for different DC current loads. - 122 -

Table 4.8: Comparison between mean relative and maximum absolute winding temperature prediction error of reduced dimensions analytical models and original LPTN for different DC currents applied. .....- 128 -

Table 4.9: Computational time required for the temperature prediction at each iteration for the thermal models considered. .....- 129 -

CFD	Computational Fluid Dynamics
DSP	Digital Signal Processor
EHA	Electro-Hydraulic Actuator
EMA	Electro-Mechanical Actuator
EMF	Electromotive Force
FEA	Finite Element Analysis
FFT	Fast Fourier Transform
GPIO	General Purpose Input-Output
IEC	International Electrotechnical Commission
IEEE	Institute of Electrical and Electronics Engineers
IPM	Interior Permanent Magnet
LCC	Low Computational Cost
LPTN	Lumped Parameter Thermal Network
MEA	More Electric Aircraft
NEMA	National Electrical Manufacturers Association
PEMC	Power Electronics, Machines and Control
PM	Permanent Magnet
PMAC	Permanent Magnet synchronous
PS	Power Supply
RMS	Root Mean Square
SMPM	Surface Mounted Permanent Magnet
SPEARE	Small Platform Electrical Actuation Retraction Extension
SQP	Sequential Quadratic Programming

SR	Switched Reluctance
THD	Total Harmonic Distortion
UoN	University of Nottingham

%PM	PMs pole pitch
%SO	Slot opening as slot pitch percentage
α_0	Copper thermal coefficient of resistivity
η_{HD}	Efficiency of the Harmonic Drive
η_{SG}	Efficiency of the Spur Gear
λ_{aPM}	Fundamental of the PM flux linking the phase a
λ_{bPM}	Fundamental of the PM flux linking the phase b
λ_{cPM}	Fundamental of the PM flux linking the phase c
Φ_m	Peak flux penetrating the winding
Ψ_{PM}	Permanent magnets flux linkage
Ψ_d	d-axis flux linkage
Ψ_q	q-axis flux linkage
$\sigma_{rot,tang}$	Tangential stress in the airgap
τ	Motor torque
τ_M	Maximum torque at the motor shaft
τ_{pivot}	Maximum torque at the pivot
τ_{SH}	Braking torque produced by a shorted three-phase star
ω	Rotor speed
ω_{el}	Electrical speed
Ω_M	Maximum rotational speed at the motor shaft
Ω_{pivot}	Maximum rotational speed at the pivot
c_{hous}	Housing specific heat capacity
C_i	LPTN i-th capacitance

$C_{i,j}$	j-th thermal mass in the stator iron
$C_{r,j}$	j-th thermal mass in the rotor
$C_{s,j}$	j-th thermal mass in the stator slot
d_{rotor}	Rotor external diameter
$d_{stator,ext}$	Stator external diameter
$d_{stator,int}$	Stator internal diameter
E_a	Phase a back-emf
E_{apeak}	Peak value of the phase a back-emf
E_b	Phase b back-emf
E_c	Phase c back-emf
E_m	RMS value of the phase back-emf
err_i	Mean relative error between predicted temperature and i-th temperature profile
F	Measure of insulation lifetime remaining
f_{obj}	SQP algorithm objective function
h_{ag}	Airgap convection coefficient
h_{ext}	External convection heat transfer coefficient
I	Winding rms electrical current
I_d	d-axis stator current
I_{dSH}	d-axis current in shorted three-phase star
I_q	q-axis stator current
I_{qSH}	q-axis current in shorted three-phase star
I_{SH}	Current in the shorted three-phase star
J_{loss}	Joule losses heat source

J_{slot}	Slot current density
k	Free parameter of thermo-mechanical ageing model
k_{copper}	Copper thermal conductivity coefficient
k_{eq}	Slot equivalent thermal conductivity coefficient
K_{FF}	Slot fill factor
k_{ins}	Winding insulation thermal conductivity coefficient
k_{iron}	Stator lamination thermal conductivity coefficient
k_{ω}	Winding factor
L_d	d-axis inductance
L_q	q-axis inductance
L_{stack}	Motor stack length
$\mathcal{L}$	Insulation lifetime under thermal and thermo-mechanical stresses
$\mathcal{L}_0$	Insulation lifetime at reference temperature T_0
$\mathcal{L}_M$	Insulation lifetime under thermo-mechanical stress
$\mathcal{L}_T$	Insulation lifetime under thermal stress
$\mathcal{L}_V$	Insulation lifetime under electrical stress
N	Free parameter of thermo-mechanical ageing model
N_{turns}	Number of turns per phase
Q	Free parameter of thermal ageing model
R	Phase resistance

$R_{ag,j}$	j-th conduction resistance in the airgap between rotor and stator
$R_{conv,j}$	j-th convection resistance between ambient and housing external surface
R_{el20}	Phase electrical resistance at 20°C
R_{HD}	Gear ratio of the Harmonic Drive
$R_{h,j}$	j-th conduction resistance in the housing
R_i	LPTN i-th resistance
$R_{i,j}$	j-th conduction resistance in the stator iron
R_{radial}	Radial conduction thermal resistance
$R_{r,j}$	j-th conduction resistance in the rotor
$R_{rot,ext}$	Rotor external diameter
R_{SG}	Gear ratio of the Spur Gear
R_{shaft}	Axial conduction resistance in the shaft
$R_{s,j}$	j-th conduction resistance in the stator slot
$R_{tangential}$	Tangential conduction thermal resistance
s^2	Sample variance
t	Time
T	Winding temperature
T_0	Reference insulation temperature
$t_{0,i}$	Temperature profile initial temperature
t_{ag}	Airgap thickness
T_{amb}	Ambient temperature
$t_{f,i}$	Temperature profile final temperature

T_{final}	Maximum winding temperature at the end of the duty cycle
T_M	Winding insulation thermal class
$T_{mea,i}$	Measured winding temperature
$T_{mod,i}$	Predicted winding temperature
t_{PM}	PM thickness
t_{tooth}	Stator tooth thickness
t_{yoke}	Thickness of stator back-iron
v	Winding temperature variation respect to time
v_d	d-axis voltage
v_q	q-axis voltage
$\bar{x}$	Sample mean

Chapter 1
Introduction

This chapter acts as a general introduction to the whole project that is described in this thesis. The rationale, the main objectives and the challenges of the project are presented, as well as the main contributions to research that helped achieve the projects' objectives.

1.1 Introduction

Over the last fifteen years, the Power Electronics, Machines and Control (PEMC) research group of the University of Nottingham (UoN) has been actively engaged with the More Electric Aircraft (MEA) initiative [1], [2]. While covering most of the relevant areas of the MEA, such as landing gear, electric power systems (EPS), de-icing and avionics, a main point of interest within the group has been that of actuation, including actuation for primary flight control surfaces and also for secondary control systems.

For this latter, a number of projects related to the development of high performance actuators related to the aircraft of the future are being taken forward by the research group. An important consideration is that a significant number of these projects involves the use and development of Electro-Mechanical Actuators (EMAs), including high profile projects within the MEA community, such as [3] and [4].

The most recent project featuring an EMA development for aerospace applications is the Small Platform Electrical Actuation Retraction and Extension (SPEARE) project, which is concerned with the development of an actuation system for a helicopter landing gear application. The project's overarching aim is to develop a high power density and highly reliable rotary EMA to be installed in the helicopter's nose landing-gear, which performs the required extension/retraction of the latter. The work described in this thesis is part of the development of this system. In the next section, an overview of the SPEARE project is provided.

1.2 The SPEARE project overview

The SPEARE project has been developed by the UoN in partnership with Triumph Group Inc. and Heroux-Devtek, two leading companies in the production of systems and components for the aviation industry. The overarching aim of the project is to research, develop and experimentally validate a working prototype of the required EMA, in order to analyse the feasibility of this solution as a viable alternative to the electro-hydraulic actuators usually employed for the actuation of the helicopters' landing gear. A schematic diagram of the whole system is shown in Figure 1.1.

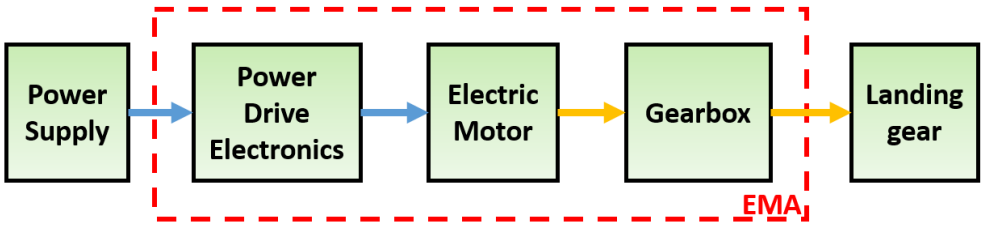


Figure 1.1: Diagram of the rotary EMA of the landing gear for the Speare project.

The development of the EMA for the SPEARE project has been jointly carried out by the UoN and its partners. The project's technical and system-level lead was Heroux-Devtek, which, as the main system integrator (development of the landing gear), was responsible for all the system requirements specifications. Triumph Group Inc. was responsible for the design and development of the gearbox and the EMA's assembly procedures. The team within the UoN was responsible for the design, development and prototyping of the power converter,

the electric motor and the control system of the EMA. The thesis work presented herein describes the design and development of the electric motor for the EMA.

1.3 The electrical machine

Any component being developed for an aerospace application is usually designed with two main objective functions, i.e. system weight minimisation and reliability. In other words, the SPEARE electric motor needed to be designed in such a way as to maximize its torque density and at the same time to ensure that its components comply with the required reliability measures during operations.

Permanent Magnet (PM) machines are often employed due to their inherent high torque density, despite the reliability issues related to the presence of the magnets. In order to minimize the risk of single points of failure, fault tolerant solutions are often preferred for the motor. These solutions are characterized by the adoption of redundant phases for the motor windings which allow the motor to operate after a single fault in its electrical system. However, the increase of reliability provided by such solutions penalizes the motor torque density.

An important aspect of the SPEARE project is that it is a short time duty application. In fact, the actuator operates only for few seconds during the retraction and extension of the landing gear. The main characteristic from the motor side, for this type of applications, is that the temperature distribution will not reach a steady state condition during operations. Considering that the maximum temperature reached will be lower than the steady state temperature, higher current densities can be employed for the motor windings with a

consequent increase of the motor torque density. However, an excessive increase of the operating temperatures could expose the motor to early windings failures due to the rapid deterioration of their electrical insulation.

Thus, in order to maximize the motor torque density whilst complying with the reliability requirements, it is necessary to develop a design methodology which exploits the short time duty nature of the application. Clearly, this involves a good knowledge of the machine thermal behaviour, as well as of the ageing processes acting on its most critical components during operations. To this end, a major part of the thesis work investigates the design of electrical machines for short time duty applications.

1.4 Thesis's aim and objectives

The main aim of the thesis is to propose a design methodology for short time duty cycle, PM machines that allows significant improvements in the machine's torque density performance without compromising its reliability expectations. As vessel to investigate this challenge, a surface mounted permanent magnet (SMPM) fault tolerant machine for a helicopter landing gear EMA application is considered.

Since the characteristics of these type of applications are exploited by employing high current densities for the stator windings, the windings' electrical insulation system will experience critical temperature cycles during operations. In light of this aspect, two main topics have been addressed in this work, namely:

- Thermal modelling of the stator windings during low-rate duty operations;
- Ageing of the windings' electrical insulation system under thermal and thermo-mechanical stresses.

A number of objectives and milestones were identified in order to achieve the mentioned aim, including:

- a structured methodology for the design of fault tolerant SMPM machines for low-rate duty applications;
- an analytical thermal model which features high accuracy for the winding temperature prediction along with low computational cost;
- a winding insulation lifetime consumption model which relates the winding's time to failure to the winding temperature profile during operations.

The proposed machine design methodology allows increasing the windings' current density (and thus the torque density) whilst guaranteeing the required reliability, through an analysis of the motor temperature distribution and the related ageing processes during both healthy and emergency operations. In particular, with respect to the standard design methodology where a maximum winding temperature constraint is set for reliability reasons [5], such constraint is removed by exploiting the winding insulation lifetime consumption model for verifying that the reliability requirements are respected.

Starting from a standard LPTN, a novel tuning procedure based on experimental temperature acquisitions is proposed, which allows increasing the accuracy of the temperature predictions. Furthermore, a simplified analytical thermal model is derived from the initial LPTN, which features similar accuracy of the original model but a sensibly lower computational cost.

A novel winding insulation lifetime consumption model which includes the effects of both thermal and thermo-mechanical ageing for the evaluation of the insulation degradation is presented. The main novelty is that it provides a direct relationship between winding temperature profile and lifetime consumption. The model is tuned on the base of a number of accelerated ageing tests, which have been specifically designed for the proposed model.

1.5 Thesis's structure

The thesis consists of six chapters, which reports the work conducted in order to achieve the objectives mentioned above.

Chapter 1 serves as an introduction to the investigated applications' challenges. Chapter 2 is a literature review of EMAs for aerospace applications, advancements in electrical machines thermal models and reliability aspects.

Chapter 3 presents the EMA project considered and the application specifications. A structured motor design procedure is proposed for short-time duty SMPM machines, which makes use of the Finite Element method for modelling the electromagnetic performance and of a LPTN for the thermal analysis. A prototype of the designed motor has been manufactured and the

results of the tests conducted on such motor are analysed and employed for validation of the simulations predictions.

Chapter 4 investigates the thermal modelling of the SMPM motor. A LPTN model is firstly presented. The limits of the model are evaluated through a comparison with experimental thermal tests conducted on the motor prototype. A novel tuning procedure for the most critical LPTN parameters is presented, which allows increasing the accuracy in the winding temperature prediction. A novel simplified thermal model is derived from the considered LPTN, which shows similar accuracy but sensibly lower computational cost respect to the original LPTN.

Chapter 5 concerns with the winding electrical insulation system ageing processes. A literature review on the advancements in insulation ageing modelling under different stress factors is reported. A novel lifetime prediction model is proposed which attempts to relate the time to failure of the electrical insulation to the winding temperature profile during operations. An accelerated ageing test procedure is proposed with the aim of investigating the windings endurance under different stresses. The results of the tests are employed for the tuning of the proposed model free parameters. Finally, an investigation on the possible applications of the lifetime prediction model is conducted.

Chapter 6 presents general conclusions of this thesis work, overall discussions and provides insights for possible future works.

1.6 List of publications related to this work

C. Sciascera, P. Giangrande, L. Papini, C. Gerada and M. Galea, "Analytical Thermal Model for Fast Stator Winding Temperature Prediction," *IEEE Transactions on Industrial Electronics,* vol. 64, no. 8, 2017.

C. Sciascera, M. Galea, P. Giangrande and a. C. Gerada, "Lifetime consumption and degradation analysis of the winding insulation of electrical machines," in *8th IET International Conference on Power Electronics, Machines and Drives (PEMD 2016),* Glasgow, 2016.

C. Sciascera, P. Giangrande, C. Brunson, M. Galea and a. C. Gerada, "Optimal design of an electro-mechanical actuator for aerospace application," in *IECON 2015 - 41st Annual Conference of the IEEE Industrial Electronics Society,* Yokohama, 2015.

Chapter 2
Literature review

This chapter presents a comprehensive literature review of the main topics treated in this thesis work. An assessment of the state of the art in the design of EMAs for aerospace applications is conducted. The main fault tolerant solutions employed for the electrical machine of such systems are reviewed. The principal challenges faced in the design of short time duty motors are evaluated. A review of the most advanced thermal modelling techniques and of the most common motor failure modes is provided.

2.1Electro-Mechanical Actuators for Aerospace Applications

In recent years, the More Electric Aircraft (MEA) initiative has led to significant progresses in the area of aircraft power systems [6]. The main objective of the MEA is the conversion of the non-propulsive power, which is historically divided between pneumatic, mechanical, hydraulic and electrical power, into only electrical power [7], [8]. This is predicted to potentially result in better management of total on-board power, with benefits in terms of fuel consumption and CO2 emissions [2], [9]. Another perceived advantage of such aircraft systems is the predicted system complexity reduction, due to the elimination of bulky and complex pneumatic and hydraulic circuits and the resulting benefits related to maintenance costs, weight and downtimes [10]. However, even after more than 20 years of the MEA initiative, these electrical systems have still not found a complete and systematic integration and implementation in today's and tomorrow's aircraft. A major bottleneck is the overall system weight but probably the most constraining factors are those related to the strict aerospace reliability requirements. Apart from all the challenges with certification and validation, an important "goodness factor" for new and innovative systems is the fact that full acceptance (both from the industry's perspective and also from the general public's impression) can only be achieved after significant times of in-service experience [11], [12]. For this reason, current utilization of electrical systems is often limited to secondary flight control surfaces, where their implementation would not be considered safety or flight critical. In light of the above, it is also true that such systems are today more present in non-commercial platforms such as for example military applications [13].

One of the main areas of interest of the MEA, is that of actuation, where Electro-Hydraulic Actuators (EHAs) and Electro-Mechanical Actuators (MEAs) are proposed as a viable alternative to the traditional hydraulic actuators [14]. The principal aerospace applications for EMAs include primary and secondary flight control surfaces actuation ([15], [16]), as well as landing gear extension, retraction and steering ([17], [18]).

An EHA is composed of a reversible pump driven by an electric motor, which supplies a local hydraulic actuator [19]. The most typical EMA architecture is a high performance electric motor driven by a power converter. The motor is often coupled to a gearbox and/or a rollerscrew in order to transmit the required torque/axial force to the load [20]. In order to be a viable alternative to the traditional actuating systems, both the EMAs and the EHAs must feature high torque/weight ratio and meet the high aerospace reliability requirements [21]. The basic architectures of an EHA and of a EMA are reported in Figure 2.1 [20].

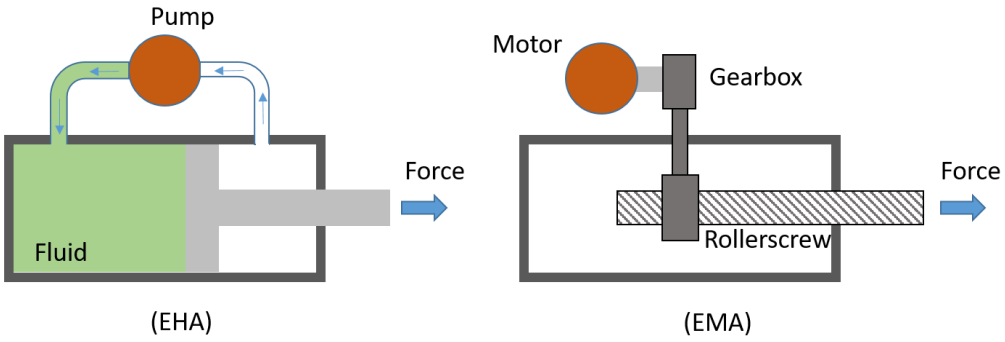


Figure 2.1: Architecture of an EHA (left) and of an EMA (right).

EHAs are inherently more reliable than EMAs and, due to the presence of fluids, can also pack significantly high force density values. However, the overall system weight when considering the presence of the local hydraulic circuit and

also the higher maintenance costs do represent two EHA aspects which have always been considered as the main two drawbacks.

EMAs on the other hand have the advantage of removing the dependency on such hydraulic circuits and can be roughly considered as stand-alone schemes. This, combined with the fact that EMAs also can reach very high and appropriate power and force density values has projected the EMA towards an ever-increasing role of importance in the aerospace actuation industry [20].

However, a main point of concern with EMAs is the possibility of mechanical jams. It is well-known and common practice [22] to try to enhance a system's through the elimination of any single point of failure. Various methodologies exist to achieve this for the electric system (electric motor and converter) such as the implementation of fault tolerant solutions [23], [4]. However, for the mechanical system, including the main gearbox and the ball-screw, this is still a critical issue. While the mechanical advantage related to the presence of the gearbox reduces the overall actuator weight, its presence also results in it being one of the most critical components in terms of reliability. The gearbox, the roller-screw and the motor bearings are considered to be single points of failure of such EMA systems [24].

Over the years, a number of solutions have been proposed and investigated in relation to achieving EMAs that can be considered jam tolerant, including the implementation of direct drives [1] which do not require a gearbox, redundant systems combined with safety power-off brakes and disconnect devices [25], linear motors [26] which do not require any intermediate mechanical component for the conversion of the torque in axial force and are therefore virtually jam-

free. However, all these known solutions generally lead to an increase of the overall weight and volume, which could then have a significant impact on the actuator's suitability for the application.

2.2 Fault tolerant electrical machines

In order to meet the reliability level required in aerospace applications, the electrical drive system of the EMA must include excellent fault tolerance capabilities. While fault tolerance is in general a vague and subjective term, in the context of the work described in this thesis, it is considered to be the ability to provide the specified full torque and speed even after a failure [27], [28]. This particular definition of fault tolerance, implies a projection towards designs that are either developed to sustain operation at much higher than rated values or designs that incorporate redundancy in the system. Usually in the context of aerospace applications, fault tolerance by redundancy is a common and widely-used option. In particular, multi-phase fault tolerant machines driven from separated power converters are often preferred [29], [30].

2.2.1 Considerations on PMAC and SR machines

PMAC machines and Switched Reluctance (SR) machines are traditionally the most common solutions for motors used in the MEA concept [31].

The main advantages of SR machines are related to their robust and single material rotor configuration. Another advantage is their inherent fault tolerance capabilities related to the fact that the phases are electrically isolated from each other and thus the failure of one phase does not prejudice the operations of the

other healthy ones [32]. On the other hand, SR machines cannot compete with PMAC machines in terms of torque density and can be roughly 50% larger than an equivalent PMAC machine [31].

While the use and implementation of PMs has resulted in the PMAC machine achieving the best performance values in terms of power/torque density and efficiency, it also results in a number of significant challenges, including:

- the risk of PM demagnetization, due to high temperatures and/or magnetic field distributions;
- the presence of the back electromotive force (back-emf) in the stator windings, induced by the rotating magnetic field which is generated by the PMs. This back-emf creates undesired currents in shorted faulty phases, affecting the motor fault tolerance capabilities [33];
- The high cost of PM material, due to the increasing market price for rare-earth magnets [34].

However, similar fault tolerance capabilities as for the SR machines can be achieved by PMAC machines, mainly through [35]:

- The use of single layer concentrated configuration for the windings, in order to physically isolate different phases, as well as to reduce their mutual inductance;
- Increase of the phase inductance in order to limit the short circuit current of a faulty phase;

- Implementation of dedicated control strategies for torque compensation under faulty operations [36].

Considering the intrinsic higher torque density, the potential (by design) for similar reliability figures and lower torque ripple, than it is clear why PMAC machines are often preferred to SR machines, in spite of the higher cost deriving from the employment of rare-earth PMs [37]. For this reason, the rest of the thesis is only concerned with PM machines.

2.2.2 PMAC machines

PMAC machines can be divided in two different categories, according to the position of their PMs. The first are Surface Mounted Permanent Magnet (SMPM) machines, which are characterized by permanent magnets mounted on the rotor surface. The second are Interior Permanent Magnet (IPM) machines, where the permanent magnets are inserted inside the rotor. A sketch of the rotor cross section for the two configurations is shown in Figure 2.2.

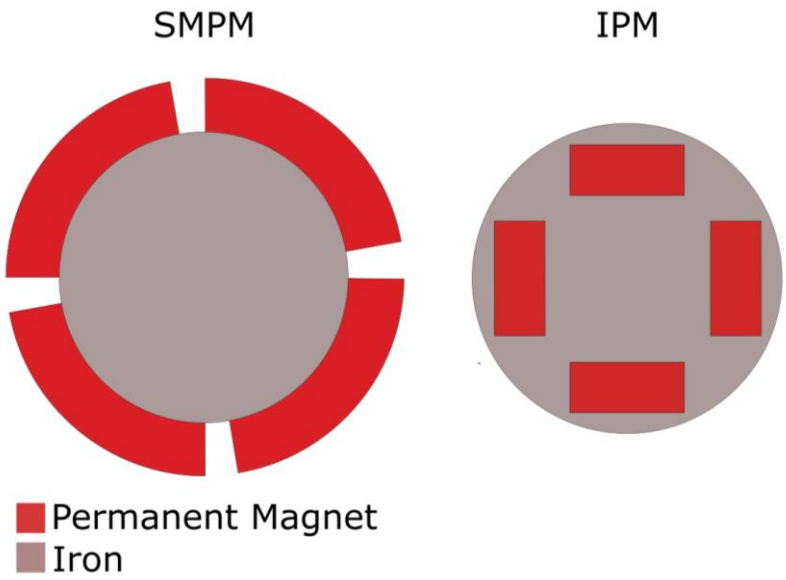


Figure 2.2: Cross section of SMPM (left) and IPM (right) rotors.

Both configurations shown in Figure 2.2 have been extensively analysed in literature [38], [39], [40], [41]. In general, SMPM machines can achieve higher torque density respect to IPM machines, with consequent system-level mass and volume reduction [42]. SMPM machines are also more efficient, mainly due to the inherent lower rotor losses, as well as lower stator iron losses thanks to a smoother flux density waveform [38]. They are also characterized by lower torque ripple [41]. The main disadvantage of SMPM machines is the necessity of a retaining sleeve, especially for high speed applications, whose function is to protect the permanent magnets from external contamination and to prevent the risk of their detachment from the rotor [38].

IPM machines have higher inductances with respect to SMPM machines, which is an important feature for fault tolerant applications, since in this way the magnitude of short circuit currents in the stator windings is reduced [41]. Another perceived advantage of IPM machines is the higher saliency ratio, which makes them more suitable for advanced sensorless control techniques [43], as well as for applications where field-weakening capabilities are required [44].

As stated above, for PMAC machines, single layer concentrated configuration is typically chosen for the stator windings for fault tolerance reasons. The advantages of this configuration include the end-winding copper volume

reduction, which as a consequence allows reducing the Joule losses generated in the windings, as well as simplifying the manufacturing procedure [45] [46].

In order to increase the PMAC motor torque density, fractional slot per pole per phase configurations are adopted [47]. In fact, with such configurations, high winding factor (which is defined as the ratio of flux linked by all the turns of a winding over the total flux [48]) values can be achieved. Table 2.1, the source of which is [46], shows, for a list of realizable three-phase machines with balanced concentrated windings, the winding factor related to the flux fundamental component, for different combinations of number of slots *S* and of poles *p*.

S \ *2p*	**2**	**4**	**6**	**8**	**10**	**12**	**14**	**16**	**18**	**20**	**22**	**24**
3	.866	.866		.866	.866		.866	.866		.866	.866	
6		.866		.866	.866		.866	.866		.866	.866	
9			.866	.945	.945	.866	.945	.945		.945	.945	
12				.866	.966		.966	.966		.866	.966	
15					.866		.866	.866		.866	.951	
18						.866	.945	.945		.945	.902	.866
21							.866	.932		.953	.953	
24								.866		.966	.957	

Table 2.1: Winding factor for different combinations of number of slots and pole pairs, allowing the realization of a three-phase machine with balanced concentrated winding [46].

From Table 2.1, the maximum winding factor achievable is 0.966. The simplest configuration is the one with 12 slots/10 poles, which is employed in several fault tolerant applications present in literature [41], [4], [49], [50].

2.3 Electrical machines for Short Time Duty Applications

Some of the aerospace applications of the EMAs are characterized by a low-rate duty cycle. For instance, the actuator of a landing gear typically operates for few seconds during deployment/retraction operations, followed by a long period of inactivity (short-time duty cycle). Similarly, most of the primary and secondary flight control surface actuators are designed for intermittent duty cycles.

For a motor, a short-time duty cycle can be defined as a constant load applied for a given amount of time, shorter than the time required for the motor to reach thermal equilibrium, followed by a no load period long enough for the motor temperature to decrease back to the coolant temperature. Similarly, for intermittent duty, a sequence of identical short-time duty cycles is applied, where the maximum temperature during each cycle remains always lower than the motor thermal equilibrium temperature [51]. Figure 2.3, whose source is [51], shows the typical temperature profiles Θ for the two duty cycles types.

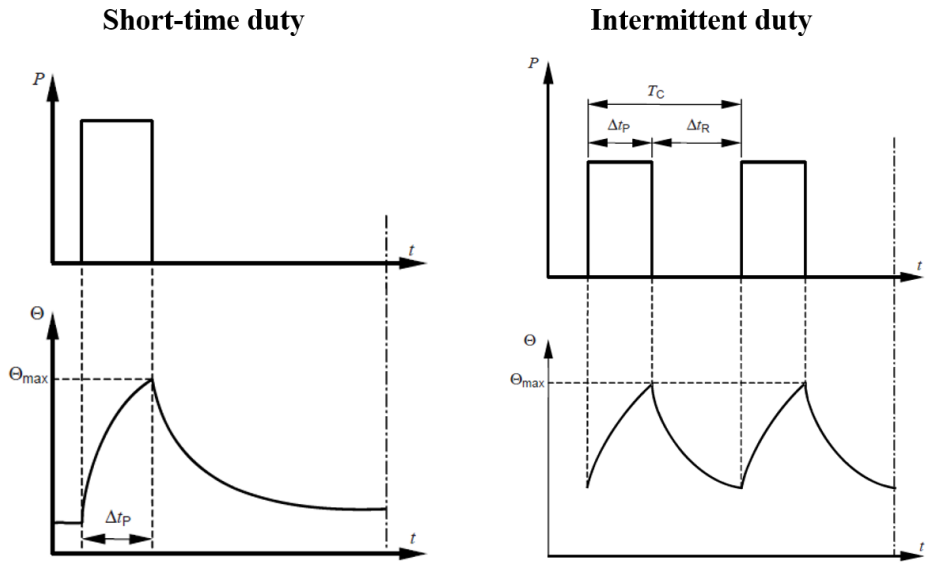


Figure 2.3: Load and motor temperature profiles for the case of short-time duty (left) and intermittent duty (right) [51] .

As described above, for these types of applications the main characteristic for the electric motor is that it does not reach a thermal equilibrium during operations [51]. A main consequence is that it is not trivial to determine the effect of thermal related stresses on the lifetime of the motor, as the temperature is time variant and does not reach a steady state value. For this reason, in order to guarantee the reliability level required, it is common practice to design the motor in such a way that the maximum temperature does not exceed the rated temperature of the materials [52], [53]. In particular, since the Joule losses in the stator are one of the main heat sources for this type of applications, the current densities of the windings are carefully selected in order to minimize the motor weight whilst respecting the reliability figures [54].

This strategy could still lead to oversizing of the motor as the maximum temperature is reached only for few seconds during the duty cycle [55]. On the other hand, identifying the design boundaries is complicated by the fact that:

- The lifetime of the stator windings' electrical insulation system, which is the most stressed component by thermal ageing, is not easily assessed due to the presence of time varying temperatures [56];
- The high current densities in the windings typically involved in these applications cause steep temperature transients, which due to thermo-mechanical ageing can significantly shorten the lifetime of some components [57]. Predicting and modelling these effects in lifetime consumption models is a very difficult task;

- The motor transient temperature distribution is difficult to be modelled, causing uncertainties in the prediction of temperature related stresses acting during operation [58].

For these reasons, a thorough analysis of the temperature dynamics and of the ageing processes during operations is mandatory in order to exploit the characteristics of low rate duty applications.

2.4 Thermal modelling techniques

Thermal analysis of electrical machines has become a fundamental part of the motor's design, also due to the increasingly demanding requirements in terms of torque density and costs reduction in the aerospace and automotive fields [59]. During the design process of the motor, a multi-physics approach is often preferred, where a thermal analysis of the motor is carried out in parallel with the electromagnetic one, with the aim of optimizing its performance [60]. In this way, both the magnetic limitations and the thermal limits set by the materials properties are taken into account, and high performance solutions can be achieved [52].

Three types of thermal models are mainly used for the analysis of the motor temperature distribution, which are:

- Finite Element Analysis (FEA);
- Computational Fluid Dynamics (CFD);
- Lumped Parameter Thermal Networks (LPTN).

FEA is a numerical method which can be employed for the calculation of an approximated solution of the partial differential equations governing the heat transfer within the motor. The method is based on the discretization of the motor spatial domain in small subdomains (the finite elements) and on the calculation of a numerical solution of the heat equation over the discretized domain [61]. FEA can provide accurate prediction of the temperature distribution within the motor [62], [63]. Although FEA can only model heat transfer of solid materials, empirical equations can be employed for approximating the convection heat transfer with the external ambient and in the airgap annulus [59].

CFD is another numerical method which can achieve high temperature distribution accuracy [64], [65]. Relative to the FEA, it allows to model also the heat transfer in fluids. Thus, it is a useful tool for the analysis of the heat flow in critical areas such as the housing surface and the end-windings region [66], [67].

LPTN models represent the heat transfer in the motor with an equivalent circuit. In this model, the motor is divided in portions, each one associated to a node of the circuit. In particular, the nodes' potential represents the average temperature in the respective motor portion. Thus, by using well-known algorithms for the resolution of circuits, it is possible to obtain the temperature dynamics in the most important motor spots. Typically, LPTNs are composed of a small number of nodes, which represent the thermal behaviour in the motor areas with similar temperature and thermal characteristics [59], [68].

LPTNs are often preferred to numerical methods because of their considerably lower computational cost and setup time. Also, with the appropriate methodologies, LPTNs can be developed to achieve excellent accuracy [59],

[69]. In particular, LPTNs can be suitable for online temperature prediction algorithms [70], as well as for joint electromagnetic/thermal analysis, thanks to the speed of operations [71], [72]. On the other hand, their nature indicates that when more complex motor geometries are investigated, then the more sophisticated CFD and FEA methods are required, which allow for detailed maps of the temperature distribution within the motor [73], [74]. Alternatively, hybrid combinations of LPTNs informed by FEA or CFD can be proposed, e.g. when the numerical models are employed for tuning the parameters of the LPTN model with the aim of enhancing its accuracy [59].

In general, the accuracy of any thermal model for an electrical machine relies upon a fine tuning of a number of uncertain parameters [75]. These uncertainties can be related to the materials properties, manufacturing tolerances, assembly process and interaction with other drive system components [76]. The most critical motor areas, whose thermal behaviour is more difficult to be modelled, include:

- Stator slots: their thermal modelling is complicated by the heterogeneity of the materials (conductor, insulation coating, impregnation, slot liner) and their complex distribution in the slots, especially for the case of random wound windings where the wires spatial location in the slots is not defined [77]. In order to simplify the modelling problem, the slots are often considered as an equivalent homogeneous material whose thermal properties approximate the behaviour of the original materials [63], [78], or by simplifying the materials distribution with easier to model equivalent layered distributions [75].

- Surface between stator laminations and housing: the heat transfer between solid bodies in contact depends on several factors such as contact pressure, surface roughness and surface cleanliness [79]. The heat conduction between stator laminations and housing is difficult to be modelled due to uncertainties deriving from the manufacturing process, as well as to the contact pressure variation caused by different thermal expansion rate of the materials involved [75].
- Airgap: the convective heat transfer between rotor and stator through the airgap can be modelled using well-known equations for the convection in the annulus of concentric rotating cylinders [80], [81]. However, inaccuracies can derive from the presence of the slot openings, the non-uniform temperature distribution along the annulus surfaces, as well as difficulties in predicting the relationship between air turbulence and rotor speed [82].
- Housing: Complex geometries are often adopted for the housing, which include the presence of fins in order to increase the external surface and thus to enhance the heat exchange with the surrounding ambient [83]. Although empirical formulas exist for the approximation of the heat dissipation performed by the housing [79], inaccuracies can derive from issues in determining the correct non-homogeneous temperature distribution within the housing due to its complex geometry, the heat exchange rate between the housing external surface and ambient which depends on the surface temperature and geometry, as well as the heat dissipation through the housing supports [84], [85], [86].

- End windings: the determination of the convection coefficient between the end windings and the end caps is complicated by the complex geometry of the region and due to the difficulties in predicting the air flows, especially in the case of forced air cooling systems [87].

Another important factor for the achievement of an accurate thermal model is the correct determination of the losses (heat sources) distribution within the motor [88]. Although Electromagnetic FEA models allow for accurate estimation of the main heat sources, empirical formulas are usually implemented for the estimation of the losses under different operating conditions in order not to excessively increase the computational cost of the thermal model [70], [89].

2.5 Reliability of electrical machines

Electrical machines failure modes' surveys present in literature reveal that the majority of the faults are related to the stator windings insulation system or to mechanical failures [90], [22], [91], [92].

2.5.1 Mechanical failures

Bearings mechanical failure are principally caused by wear or fatigue. Typically, the root causes of failures are machine overloading, loss of lubricant, excessive vibrations or undesired electric current flow in the bearings [93]. Bearing faults can be categorized in [94]:

- Single-point defect, which is a localized defect (e.g. pit, spall) on the undamaged bearing surface.

- Generalized roughness, which is a large degraded area of the bearing surface and it is due to ageing, contamination or loss of lubricant.

An incipient mechanical failure of the bearing can be diagnosed through vibrations monitoring techniques [95], which have the disadvantage of requiring the employment of an accelerometer, or more commonly through spectral analysis of the stator currents [96], thus using the current sensors which are already implemented in the machine. Most of these monitoring techniques are focused only on the detection of single-point defects, since they generate characteristic fault frequencies which are easy to be detected. However, sophisticate techniques based on noise suppression algorithms allow detecting with a certain accuracy also generalized roughness faults [97].

2.5.2 Electrical faults

The typical faults of the windings are due to the degradation of the electrical insulation, which can result in turn-to-turn, phase-to-phase or phase-to-ground short circuits [98]. An early failure of the winding electrical insulation can be due to a manufacturing defect such as a void or a scratch, or due to an unexpected over stress which can be generated in case of motor overloading [99]. Apart from these extraordinary causes, the failure of the winding electrical insulation is usually consequence of the ageing of its materials, which is due to the degradation caused by the stresses applied during operations [100].

The stresses which can deteriorate the electrical insulating materials can be divided in:

- Thermal stress: High temperature can trigger chemical reactions which eventually deteriorate the insulating material. Typically, the main chemical reaction is oxidation, which causes delamination and cracks of the insulating materials [101].
- Thermo-mechanical stress: High temperature variations cause expansion of the materials which generate a mechanical stress on the insulating materials. This stress is more severe when the temperature in the slot is non-homogeneous as well as when bonded materials have significantly different thermal expansion coefficients. For example, in enamelled magnetic wires the winding conductor is in adhesive contact to the insulating coating, thus in case of steep windings temperature variations, a proportional shear stress is exerted on the contact surface between conductor and insulation [102].
- Electrical stress: It is mainly related to partial discharge activity in the voids of the insulating materials. Partial discharges are typically more intense for the case of motor fed by pulse width modulated voltages [103]. This is consequence of the fact that fast voltage rise times cause a non-homogeneous voltage distribution along the stator windings, thus creating higher voltage differences than expected between adjacent coils [104]. Also, fast voltage transients could magnify the effect of impedance mismatch between the power supply and the motor windings, which can cause peak voltages up to two times the DC-Link voltage [105], [106].
- Mechanical stress: There are multiple sources of mechanical stress on the winding insulation. Apart from the thermo-mechanical stress which has

been mentioned above and the residual stress due to the fabrication process of the magnetic wire, the windings are stressed by vibrations. These vibrations are generated either by the spinning rotor which transmits mechanical vibrations to the stator through the bearings, as well as by means of Lorentz forces generated between different wires in the same slot [107].

- Environmental stress: It includes radiations, moisture and chemicals contamination. In particular, moisture can decrease the dielectric breakdown voltage and create conductive paths over the insulation external surface, facilitating the partial discharge activity [108].

It is then crucial to select the insulating system in such a way that the ageing due to the abovementioned stresses do not lead to an early failure of the winding. In order to limit thermal ageing, the insulating materials must be selected in a thermal class higher than the maximum operating temperature [109]. Partial discharge activity can be prevented by proper selection of the insulation thickness [110]. Impregnation of the windings in varnish or resin helps reducing their mechanical vibrations, improves the heat dissipation capability and serves as a protection from moisture and contamination [111].

Different condition monitoring techniques can be implemented for the detection of incipient winding faults. These techniques include injection of high frequency signal and analysis of the resulting currents [112] [113], or analysis of the negative-sequence stator currents [114]. However, there are concerns about the effectiveness of such techniques since in most cases a winding insulation failure starts from turn-to-turn faults, which often remain undetected [115].

2.6 Conclusions

In this chapter, a literature review of the main topic concerning the design of electrical machines for short time duty applications with focus on reliability and life-time aspects has been presented.

An overview of the state of art in the electrical actuation for aerospace applications has been provided. The main advantages and issues in the employment of EMAs have been discussed, showing that the main challenges in the design of such actuators are the high reliability constraints and the need of achieving low weight solutions.

Concerning the electrical machine for EMAs, such requirements lead to the need for high torque dense fault tolerant solutions. From the literature review, it has been observed that multi-phase PMAC machines driven from separate converters can achieve the required fault tolerance and high torque density thanks to the presence of the PMs. A detailed analysis and design procedure for PMAC machines is conducted in Chapter 3.

Since the application considered in this thesis is characterized by a short time duty cycle, a review of the main features of the electrical machines for this type of applications has been done. In particular, the review highlights how the employment of high current densities for short "burst" of time can be used in order to maximize the torque density. As a main consequence, the main issues in the design of such machines concern the resulting high windings temperatures and most importantly the extremely high temperature variations which can cause

high stress levels on the windings' insulation systems. Thus, accurate thermal management of the machine and a good knowledge of the winding insulation ageing rate are required for the achievement of high reliability and high torque density. These aspects are extensively covered in Chapter 4 and Chapter 5.

Finally, a review of the main thermal modelling techniques, of the machine failure modes and of the windings insulation main ageing factors has been conducted, which serves as starting point for the improvements proposed in this thesis for the design of electrical machines for short time duty applications.

Chapter 3
SMPM motor for a short time duty application

This chapter deals with the design and optimization of a SMPM motor. The machine is part of a rotary electro-mechanical actuator (EMA) for an aerospace application. The actuator is responsible for the extension and retraction of a mid-lift helicopter's landing gear. Since the actuator operates only for a short amount of time during take-off and landing of the helicopter, the application is classified as short-time duty application. Thus, the motor presented in this chapter will be considered as the main platform for the study with which this thesis is mainly concerned.

The specifications for the EMA are reported in Section 3.1. The main challenge of the project is to minimize the weight of the EMA whilst respecting the high level of reliability required in the aerospace field. Weight minimization is important because it contributes to the overall performance of the helicopter in terms of fuel consumption. However, it is still quite common for machine and system suppliers to achieve the required reliability by employing either

redundancy and/or over-engineering, which in turn have a negative effect on the overall weight.

An EMA is a complex system, composed of interacting mechanical and electrical subsystems. The design choices for a component can heavily influence the design constraints on the other subsystems. Thus, for an optimal design of the EMA, a synchronised design methodology is required [116]. For this reason, a preliminary trade-off study has been conducted for the definition of a number of crucial parameters of the actuator. The results of this study are reported in Section 3.2.

As this thesis relies heavily on the electric motor of the EMA, in Section 3.3 the design solutions adopted for the motor of the EMA are presented. In Section 3.4 the performance of the motor designed is thoroughly analysed, by means of numerical methods for modelling the electromagnetic behaviour of the machine. Finally, in Section 3.5 the performance of the motor designed is experimentally validated. The experimental results are evaluated and compared to the results of the Finite Element analysis.

3.1 The helicopter's landing gear electro-mechanical actuator specifications

In this section, the EMA requirements are provided. The actuator must safely perform the extension and retraction of the helicopter's landing gear. Since the main objective is to realize a competitive system respect to the electro-hydraulic

actuators typically adopted for this application, both minimization of the actuator's weight and high level of reliability must be assured.

The main specifications for the EMA, as defined for the project requirements, are reported in Table 3.1.

EMA specifications
Maximum time required for the retraction of the landing gear: **10 seconds**
Maximum time required for the extension of the landing gear: **10 seconds**
Ambient temperature range: **-55 to 70 °C**
Capability to perform three consecutive extension/retraction cycles
Operating lifetime: **20,000 hours**

Table 3.1: EMA specifications for the landing gear application.

The architecture of the EMA is shown in Figure 3.1. The system is composed of a SMPM motor which includes two set of three-phase stars. Each star is fed by a separate power converter. Each power converter converts the DC input voltage into the multi-phase AC voltage required by the motor. The chosen architecture for the converter is a standard two-level inverter, because of the loads low power level, and its well-known modulation and control characteristics. The design solutions concerning the electric motor are explained in detail in Section 3.3. The redundancy of the electrical system is recommended for enhancing the reliability of the actuator and for eliminating potential single points of failure. In particular, the redundancy of the power lanes allows the EMA to operate even if a converter or a three-phase star experience a failure.

The torque is transmitted to the pivot of the landing gear through a two stage gearbox designed and developed by the project partners, which is composed of a Spur Gear coupled to a Harmonic Drive. The Harmonic Drive is chosen because of its low weight, high gear ratio and near-zero backlash. The spur gear further increases the total gear ratio.

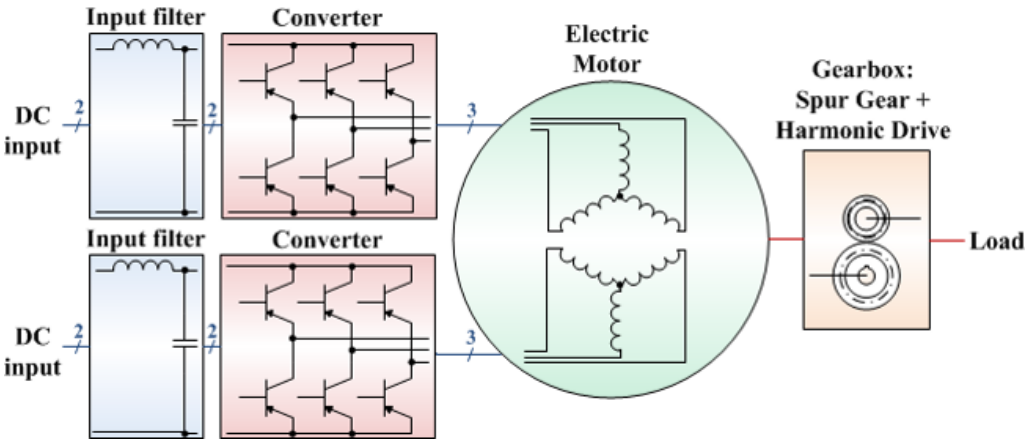


Figure 3.1: Architecture of the EMA for the retraction and extension of the helicopter landing gear.

The torque and speed profiles needed at the output of the actuator for the retraction of the landing gear were derived according to the abovementioned system requirements. The maximum torque to be provided can be thus obtained from the torque profile. Figure 3.2 shows the rotational speed profile during the retraction of the landing gear, whereas Figure 3.3 shows the torque profile during the same operation. From the load profiles, it can be seen that the maximum torque required from the EMA is 401 Nm and the maximum rotational speed is 15.3 deg/s. Because of the high torque and low speed demand, it is evident that to achieve a dense and compact system, the gearbox in the drive train plays a crucial role for the actuator's weight reduction.

In the next section, the results of a trade-off study, carried out for evaluating the best total gearbox ratio value and DC-Link voltage for which the overall system's weight is minimized, are presented. The analysis will provide an optimal value for a set of crucial parameters of the actuator.

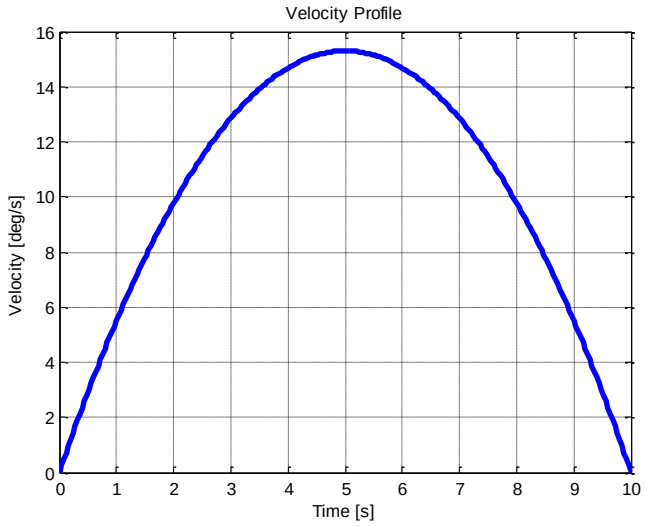


Figure 3.2: Speed profile at the pivot during the retraction of the landing gear.

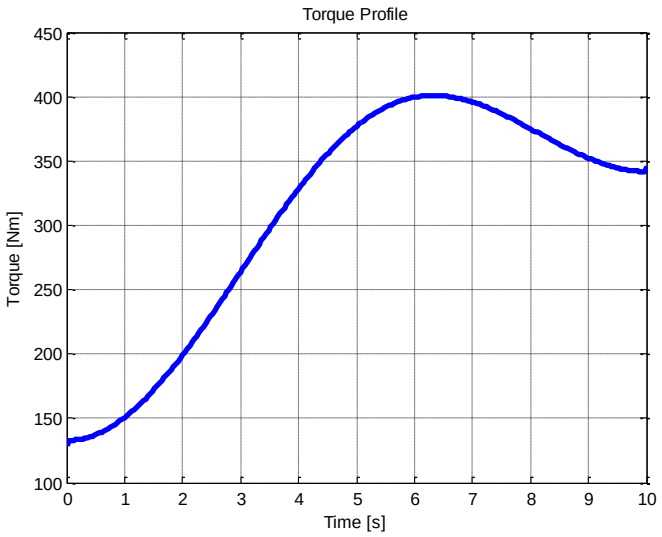


Figure 3.3: Torque profile at the pivot during the retraction of the landing gear.

3.2 Trade-off study for the weight minimization of the electro-mechanical actuator

A trade-off study has been conducted with the aim of finding the best configuration which minimizes the actuator's weight. The results of this analysis are presented in this section.

3.2.1 The motor weight

The variables selected for the trade-off study are the input DC voltage for the converters and the gear ratios of the Harmonic Drive and of the Spur Gear. In fact, for the helicopter considered, both the 28V and 270V DC buses are available. To start off, a set of possible gear ratio values for the gearbox components were considered, which are:

- 2:1, 4:1, 6:1 and 8:1 for the Spur Gear;
- 50:1, 70:1, 80:1, 100:1 and 160:1 for the Harmonic Drive.

For each combination of DC voltage and gear ratios considered, a qualitative study of the weight distribution for the EMA's components was conducted. The components whose weight was estimated were the gearbox, the electric motor, the power converters and the input filters of the power converters.

The actuator is required to provide the maximum torque τ_{pivot} at the maximum speed Ω_{pivot}, whose values are obtained from the retraction operation load profiles. For each combination of gear ratios of the Harmonic Drive and of the Spur Gear, the torque τ_M and speed Ω_M required at the motor shaft can be computed using (3.1) and (3.2), respectively, where η_{SG} represents the efficiency

of the Spur Gear, η_{HD} the efficiency of the Harmonic Drive, whereas R_{SG} and R_{HD} are the gear ratios of the Spur Gear and Harmonic Drive, respectively.

$$\tau_M = \frac{\tau_{pivot}}{R_{SG} R_{HD} \eta_{SG} \eta_{HD}} \tag{3.1}$$

$$\Omega_M = \Omega_{pivot} R_{SG} R_{HD} \tag{3.2}$$

The worst case efficiency for the gearbox components is considered, which is η_{SG} equal to 0.5 for the Spur Gear and η_{HD} equal to 0.9 for the Harmonic Drive. Table 3.2 shows the torque to be produced by the motor for each gear ratios combination. Similarly, Table 3.3 shows the rotational speed of the motor shaft for each considered gearbox configuration.

		Spur gear			
	Motor torque [Nm]	**2:1 ratio**	**4:1 ratio**	**6:1 ratio**	**8:1 ratio**
Harmonic drive	**50:1 ratio**	8.89	4.44	2.96	2.22
	70:1 ratio	6.35	3.17	2.12	1.59
	80:1 ratio	5.56	2.78	1.85	1.39
	100:1 ratio	4.44	2.22	1.48	1.11
	160:1 ratio	2.78	1.39	0.93	0.69

Table 3.2: Torque to be produced by the electric motor for each considered combination of gear ratios.

		Spur gear			
	Motor speed [rpm]	**2:1 ratio**	**4:1 ratio**	**6:1 ratio**	**8:1 ratio**
Harmonic drive	**50:1 ratio**	255	510	765	1020
	70:1 ratio	357	714	1071	1428
	80:1 ratio	408	816	1224	1632
	100:1 ratio	510	1020	1530	2040
	160:1 ratio	816	1632	2448	3264

Table 3.3: Motor shaft rotational speed for each considered combination of gear ratios.

The estimated weight of the gearbox for different gear ratios were provided by the project partners and are reported in Table 3.4.

		Spur gear			
	Gearbox mass [Kg]	**2:1 ratio**	**4:1 ratio**	**6:1 ratio**	**8:1 ratio**
Harmonic drive	**50:1 ratio**	8.6	7.25	7.25	7.25
	70:1 ratio	6.6	5.25	5.25	5.25
	80:1 ratio	3.75	3.75	3.75	3.41
	100:1 ratio	3.75	3.75	3.41	3.41
	160:1 ratio	2.85	2.51	2.51	2.51

Table 3.4: Gearbox weight estimation for each considered combination of gear ratios.

For each combination of overall gear ratios and DC-Link voltages considered in the trade-off study, a simplified motor design procedure has been implemented for the estimation of the motor weight. At this stage, most of the motor design parameters have been fixed, in order to reduce the computational effort of the trade-off study. In particular, the current density in the slots has been fixed equal to 5 A/mm^2, which is a typical value for natural air-cooled motors.

A 2D Finite Element model has been implemented for modelling the electromagnetic performance of the motor. The model has been used for determining the motor dimensions for each case considered in the trade-off study. In particular, considering that the torque required at the motor shaft varies for different gear ratios, for each case of the trade-off study the stack motor length and the rotor external diameter have been varied accordingly. Indeed, the torque produced by the motor is proportional to the stack length L_{stack} and to

the square root of the rotor external diameter $R_{rot,ext}$, as shown in (3.3), where $\sigma_{rot,tang}$ is the tangential stress in the airgap [117].

$$\tau_M = 2\sigma_{rot,tang} R_{rot,ext}^2 L_{stack} \tag{3.3}$$

The number of turns N_{turns} per phase has been also varied for each combination of the trade-off study, as its value depends on the rotor speed Ω_M, which varies for different gear ratios, and on the DC-Link voltage, whose value sets the maximum AC phase voltage that the power converter is able to provide. Thus, N_{turns} can be defined as in (3.4), where E_m is the RMS value of the phase back-emf, k_ω the winding factor and Φ_m the peak of the flux penetrating the winding.

$$N_{turns} = \frac{\sqrt{2} E_m}{\Omega_M k_\omega \Phi_m} \tag{3.4}$$

For each combination of DC-Link voltage and gear ratios evaluated in the trade-off study, the weight of the motor has been estimated. The estimated motor weights are reported in Table 3.5. As expected, the motor mass decreases proportionally with the required torque. Thus, the motor will be lighter for higher values of total gear ratios.

		Spur gear			
	Motor mass [Kg]	**2:1 ratio**	**4:1 ratio**	**6:1 ratio**	**8:1 ratio**
Harmonic drive	**50:1 ratio**	6.78	4.08	2.72	2.49
	70:1 ratio	4.84	2.89	2.38	2.33
	80:1 ratio	4.24	3.12	2.07	2.03
	100:1 ratio	4.08	2.49	1.66	1.62
	160:1 ratio	3.12	2.03	1.36	1.34

Table 3.5: Motor weight for each gear ratios combination.

3.2.2 The motor inductance

The motor weight is not affected by the value of the DC-Link voltage. However, the DC-Link voltage influences the number of turns. For different values of N_{turns}, the windings inductances value changes. The inductance value is a very important design parameter as it affects both the converter and input filter weights, but also has a significant effect on the fault tolerance (current limiting) capability of the machine.

Figure 3.4 shows how the motor d-axis inductance varies for each combination of the trade-off study. The inductances value has been calculated as in (3.5) [118], where L_d and L_q are the d-axis and q-axis respectively, Ψ_d and Ψ_q are the d-axis and q-axis flux linkages respectively, Ψ_{PM} the permanent magnets flux linkage, whereas I_d and I_q are the d-axis and q-axis stator currents respectively. The values of the quantities of (3.5) are calculated using the well-known direct-quadrature-zero transformation [119].

$$L_d = \frac{\Psi_d - \Psi_{PM}}{I_d}$$

$$L_q = \frac{\Psi_q}{I_q} \tag{3.5}$$

The d-axis inductance only has been considered in the study because its values are similar to the ones of the q-axis inductance due to the low saliency of the machine [39].

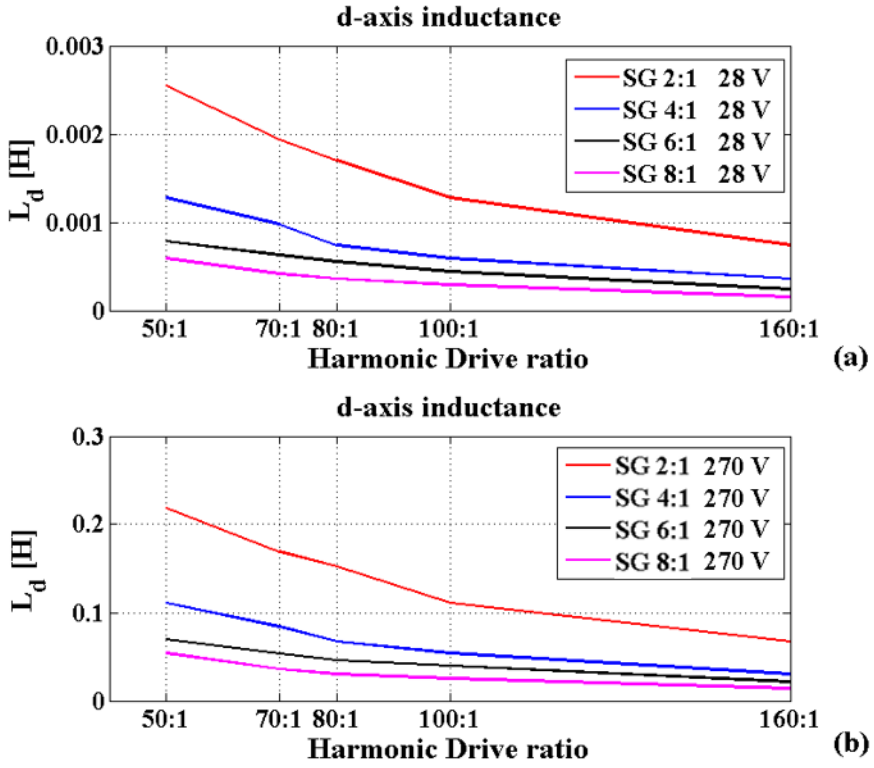


Figure 3.4: d-axis inductance value for different gear ratios and for different DC-Link voltages. (a): 28VDC case, (b): 270VDC case.

The estimated weight of the power converters could be estimated by the converter designer on the base of the DC-Link voltage and of the calculated motor inductances value.

3.2.3 The system weight

An estimation for the weight of the EMA for each combination of the trade-off study can be obtained as sum of the estimated weights of the single EMA's components. The computed values for each combination of DC-Link voltage and gear ratios considered in the analysis are shown in Figure 3.5. The graph shows that the lightest configuration for the actuator is obtained for the case of a total gear ratio equal to 960:1, which is obtained when the Spur Gear ratio is equal to 6:1 and the Harmonic Drive ratio is equal to 160:1. For this total gear ratio, the

estimated weight of the EMA is similar for both the 28 and 270 DC-Link voltages, with a slightly lighter system for the 28 V case.

However, the weight of the cable harness was not included in the analysis for the system weight's estimation. The cable harness weight is proportional to the system input DC current, which is approximately ten times bigger in the 28 VDC DC-Link voltage case respect to the 270 VDC one. For this reason, following the trade-off study, a total gear ratio of 960:1 for the gearbox and a 270 VDC voltage for the power converter supply have been chosen for the final design.

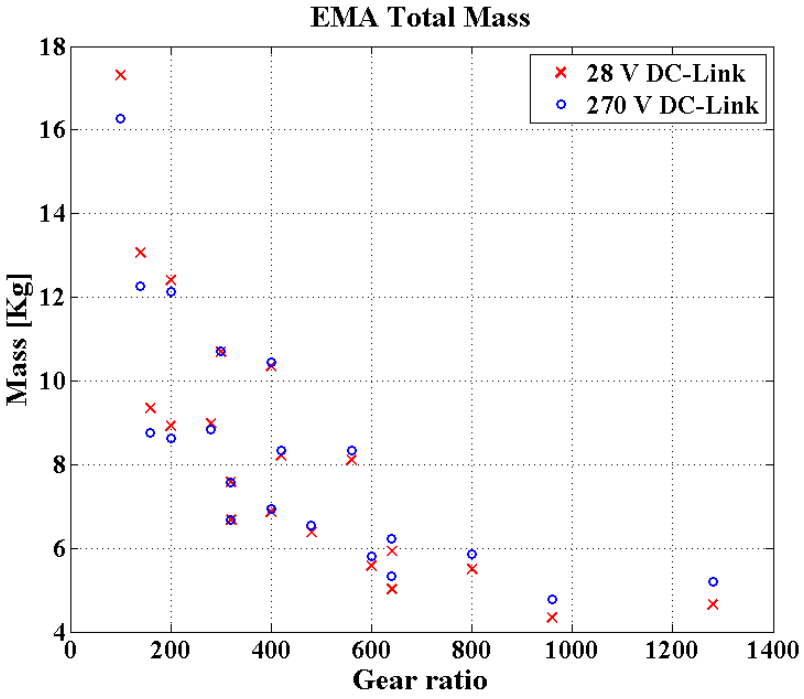


Figure 3.5: EMA weight estimation for each combination of DC-Link voltage and gear ratios considered for the trade-off study.

In the next section, the design procedure of the motor for the EMA is presented. The parameters of the EMA will be set as obtained from the trade-off analysis.

3.3 Design of the SMPM motor

Following the trade-off study of Section 3.2, where the first indications at system level of how the final system will look were derived, this section focuses on the design of the electrical machine of the EMA for the helicopter landing gear. At this design stage, an optimization of the main motor parameters have been conducted. A thermal analysis of the motor has also been integrated due to the significant effects that thermal aspects have on the characteristics of a machine being developed for a short time duty application, where high current densities are applied in the slots. The motor's fault tolerance capability is investigated as well.

3.3.1 Fault tolerance capability of the motor

As introduced in Section 3.1, the motor for the EMA is required to exhibit fault tolerance capabilities. This eliminates the risk of single point of failures for the motor, and thus sensibly increases the reliability of the machine. For this reason, the windings' configuration adopted is a double three-phase star scheme, where each star is fed by a separate power converter. With this architecture, redundancy is obtained.

The motor must produce the torque required even after a failure, which implies a design methodology that needs to be based around the identified failure modes of the system. For such short-time duty application, where thermal equilibrium (steady state) will not be reached, then a common practice is to design the motor based around high current densities for short periods of time. This means that

severe thermal cycles are experienced by the windings' electrical insulation, causing temperature related stresses on the latter. This makes the windings failures one of the most probable cause of interruption of operations.

In order to accomplish fault tolerance capability, the motor has been designed to maintain full rated operations after a:

- Open circuit fault for a three-phase star;
- Short circuit fault for a three-phase star.

These two conditions account for other windings fault types. In fact, in case of open or short circuit of one phase only, the other two phases of the same three-phase star can be externally opened or shorted as well, in order to avoid unbalanced forces; the required torque is then produced by the remaining operating star [120]. Similarly, the effects of a turn-to-turn short circuit can be partially mitigated by applying a three-phase short circuit to the faulty three-phase star [121], [122]. The case of one phase-to-ground fault is mitigated by opening the corresponding three-phase windings. Finally, also the case of failure of one converter is covered, as it causes an interruption of operations of one motor's three-phase star only.

The design strategy adopted for minimizing the weight of the motor whilst guaranteeing the required reliability consists in maximizing the current density in the slots in a manner that the slot temperature does not exceed the windings' insulation rated temperature during operations. In this way, the effect of thermal ageing is under control, since the lifetime of the windings' insulation relative to thermal ageing will be longer than 20,000 hours under these conditions [123].

According to the application's specifications, the actuator is required to perform three consecutive extension/retraction cycles, whose total duration is 60 seconds. For simplicity reasons, the motor has been designed in such a way to produce the maximum torque required without experiencing over temperatures during this period.

In order to accomplish the required fault tolerance, both healthy and faulty operating conditions have been considered. In particular, the motor has been designed for safely performing the following three operating modes:

1. Healthy operations: Both the three-phase stars contribute to the torque production;
2. Open star emergency operations: One three-phase star only contributes to the torque production while the other three-phase star is open;
3. Shorted star emergency operations: One three-phase star compensates for the braking torque produced by the shorted star and contributes to the torque production.

It follows that, with respect to an equivalent non-fault tolerant machine, the motor will be oversized in order to comply with the emergency operating modes 2 and 3. In fact, the current flowing in the operating star in mode 2 will be at least twice the current flowing in the same star during heathy operations. This current will be even higher for the operating mode 3, where also the opposition of the braking torque produced by the shorted star needs to be compensated, during the retraction of the landing gear. On the contrary, during the extension

operation, the braking torque contributes to slow down the deploying landing gear.

All this suggests that, in order to exploit the short time duty characteristics of the application, careful analysis of the thermal behaviour during both healthy and emergency operations needs to be conducted. Thus, a multi-physics approach is recommended for the design of the machine, where both the electromagnetic and thermal behaviours of the machine are taken into account.

3.3.2 SMPM motor design considerations

The literature review done for this work has informed the first stage of the design of the motor with a number of important considerations, including:

- SMPM motor type in order to achieve high torque density [124];
- 12 slots/10 pole configuration because of its low torque ripple and high winding factor, as shown in [46];
- Single layer concentrated random-wound windings configuration, in order to physically isolate different phases, as suggested in [35], for improving the fault tolerance capability.
- Non-forced air cooling in order not to add the risk of failures related to the cooling system, which would decrease the reliability of the overall system.

For the windings configuration chosen, in each slot there are the coils of one phase only. In this way different phases are thermally and electrically insulated and their magnetic interaction will be minimal. Thus, a fault in one phase is less likely to propagate to other phases or to disturb their operations.

The following materials were selected for the motor components:

- Electrical steel M270-35A for the stator laminations;
- Recoma26 (samarium-cobalt alloy) for the permanent magnets;
- 17-4 PH Stainless steel for the shaft and the rotor;
- Class 180 °C copper enamelled wires for the windings;
- Carbon fibre for the permanent magnets' retaining sleeve.

A retaining rotor sleeve has been included for protecting the permanent magnets both from external corrosive contaminants and from the risk of detachment, thus enhancing the motor reliability [125].

Figure 3.6 shows a cross-section of the first design of the motor, along with the phases' distribution along the stator slots. The rotor has been shaped with castellation in order to facilitate the insertion of the PMs during the manufacturing process.

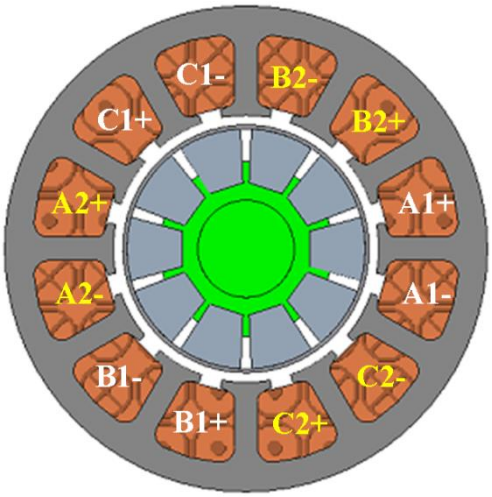


Figure 3.6: Cross section of the motor designed and phases distribution.

A parametric approach has been used for the definition of the motor geometry. The main geometrical parameters are listed in Table 3.6. A starting value for these parameters has been chosen following the guidelines for the design of SMPM motors presented in [48].

d_{rotor}: rotor external diameter
$d_{stator,int}$: stator internal diameter
$d_{stator,ext}$: stator external diameter
t_{PM}: PM thickness
$\%PM$: pole pitch percentage occupied by PMs
t_{ag}: airgap thickness
$\%so$: slot opening as slot pitch percentage
t_{tooth}: stator tooth thickness
t_{yoke}: thickness of stator back-iron
L_{stack}: motor stack length

Table 3.6: Main motor geometrical parameters.

Since there is a high number of free parameters, the following constraints have been applied to the motor geometry:

- Minimum airgap thickness 1 mm because of the manufacturing tolerances;
- Slot fill factor equal to 0.4, which is a conservative choice since its value is typically between 0.4 and 0.6 depending on the winding type and slot geometry [126];

- Motor stack length constrained to be at least 1.5 times bigger than the stator external diameter in order to neglect the end-effects in the electro-magnetic analysis of the motor.
- Split ratio, defined as the ratio between internal and external stator diameters, equal to 0.55 (it is typically between 0.55 and 0.7 [127]).

The electromagnetic performance of the motor has been analysed through the use of a 2D Finite element method, which has been implemented using MagNet software, by Infolytica. The results of the Finite Element simulations have been post processed using Matlab platform. The thermal behaviour of the motor during operations have been modelled through the implementation of a Lumped Parameter Thermal Network (LPTN) using Matlab platform. A detailed description of the LPTN is provided in Chapter 4, where thermal modelling of electrical machines is investigated.

3.3.3 Slot current density maximization

One of the scopes of the project is to minimize the overall weight of the actuator. Since the motor is designed for a short-time duty application, a procedure for the slot current density maximization has been implemented with the aim of reducing the motor weight by exploiting the application features. An iterative design procedure has been adopted for maximizing the slot current density J_{slot}, where both the electromagnetic and the thermal models were implemented. The procedure is illustrated in the flow chart shown in Figure 3.7.

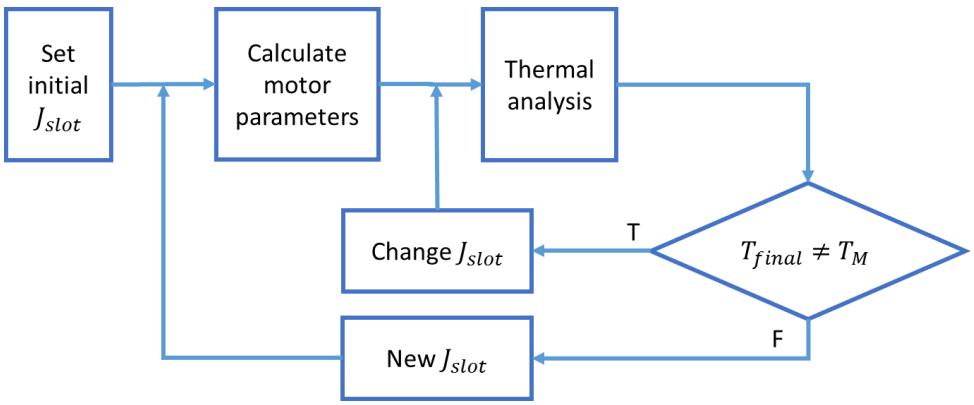


Figure 3.7: Scheme of the design procedure for the slot current density maximization.

The process starts by selecting an initial value for J_{slot}. The motor geometrical parameters are calculated for that value of J_{slot}, following the design procedure presented in [48]. The parameters are refined by using the Finite Element electromagnetic model, in order to avoid the saturation of the ferromagnetic components and in such a way that the torque required is delivered for the value of current density selected. Considering that the stator material is M270-35A, which is characterized by the B-H curve of Figure 3.8, during the motor design procedure, a maximum value of 1.7 T was set for the magnetic field in the stator in order to avoid excessive saturation.

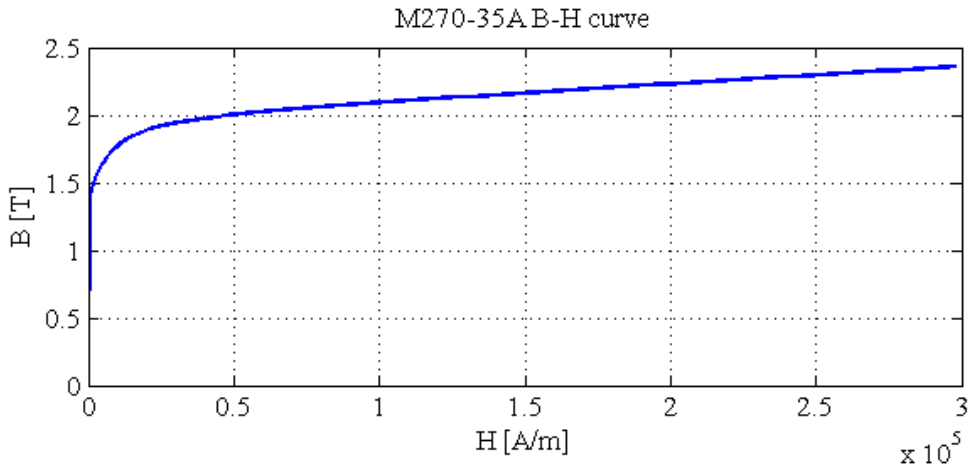


Figure 3.8: B-H curve for M270-35A material.

A thermal analysis is then conducted using the LPTN, and an estimation of the maximum slot temperature T_{final} reached by the motor at the end of the duty cycle is obtained. It is important to note that the thermal model's parameters depend both on the motor geometry parameters and on J_{slot} [128].

Since the aim is to maximize the current density while preventing any over-temperatures during operations, then the winding temperature T_{final} obtained from the thermal analysis is compared to the maximum temperature T_M allowed by the winding insulation thermal class, whose value is reported in the datasheet of the wire used. If T_{final} differs from T_M, then the current density value is tuned in order that the output of the thermal model and T_M are similar. In particular if T_{final} is bigger/smaller than T_M, then J_{slot} is decreased/increased accordingly. The whole design process is repeated with the new calculated J_{slot} as the initial input. At convergence of the algorithm, the electromagnetic performance will be as required by the application and the temperature reached during operations will

be the maximum allowed by the thermal class of the windings' electrical insulation.

3.4 Performance analysis of the SMPM motor

In this section, a detailed analysis of the electric motor designed is conducted. The electromagnetic properties of the machine have been simulated through the use of the 2D Finite Element method.

The main motor's geometrical dimensions are reported in Table 3.7.

Stator outer diameter	50 mm
Stator inner diameter	27.5 mm
Stator yoke thickness	2.76 mm
Stator tooth thickness	2.4 mm
Airgap thickness	1 mm
PM span	0.85
PM thickness	5.55-5.8 mm
Rotor iron external diameter	18 mm
Stack length	83 mm

Table 3.7: Main geometrical dimensions of the SMPM motor.

The most significant quantities under healthy operating conditions are reported in Table 3.8. With respect to the trade-off study, where the slot current density was equal to 5 A/mm^2, which is a reasonable value for continuous operations, its

value is increased to 12.5 A/mm^2 as result of the optimization procedure which exploited the short-time duty characteristics of the application.

The phase resistance has been calculated including the end-windings resistance as shown in [129], where an estimation of the end-winding resistance for concentrated windings configuration is presented.

Electrical/Mechanical power	310.4/262.2 W
Phase peak current	1.56 A
Phase resistance	5.24 Ω
Fundamental frequency	208.33 Hz
Number of turns	167
Motor weight	0.941 Kg
Motor volume	1.63 L
Slot current density	12.5 A/mm^2
Nominal torque	1 Nm
Nominal speed	2500 rpm

Table 3.8: Main motor quantities under healthy operating conditions.

The magnetic flux density distribution and the flux path within the motor, under no load conditions, when one star is fed only and when both stars are fed, were calculated using the Finite Element method and are shown in Figure 3.9, 3.10 and 3.11, respectively.

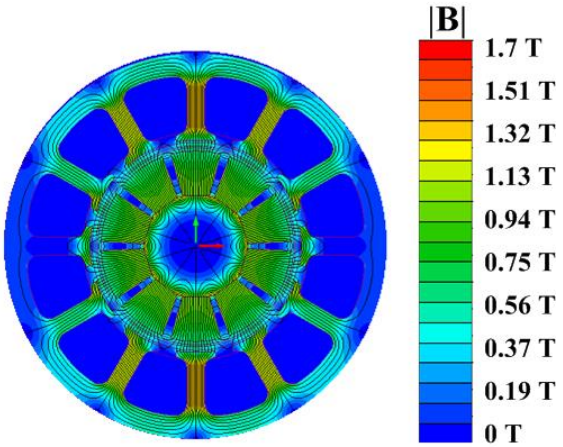


Figure 3.9: Flux density distribution (shaded) and flux paths in the motor under no load conditions.

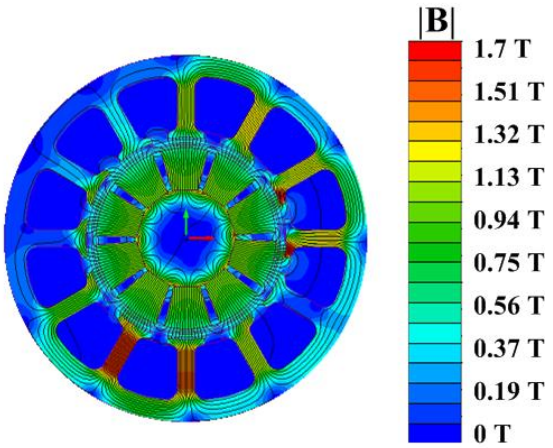


Figure 3.10: Flux density distribution (shaded) and flux paths in the motor when one star is fed with 3.12 A.

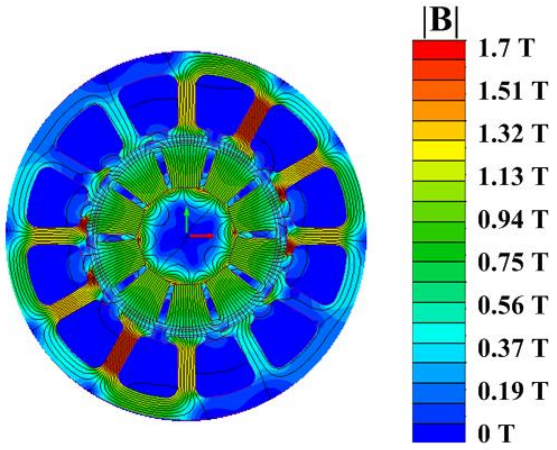


Figure 3.11: Flux density distribution (shaded) and flux paths in the motor when both stars are fed with 3.12 A.

Figure 3.12 shows the back-emf induced in one three-phase star at rated speed. The back-emf's curves for the second three-phase star are not represented, as they overlap the ones of the first star. This because the windings are distributed in such a way that there is no phase displacement between the two stars. The Total Harmonic Distortion (THD) of the line-to-neutral voltage is 5.3% of the first harmonic amplitude.

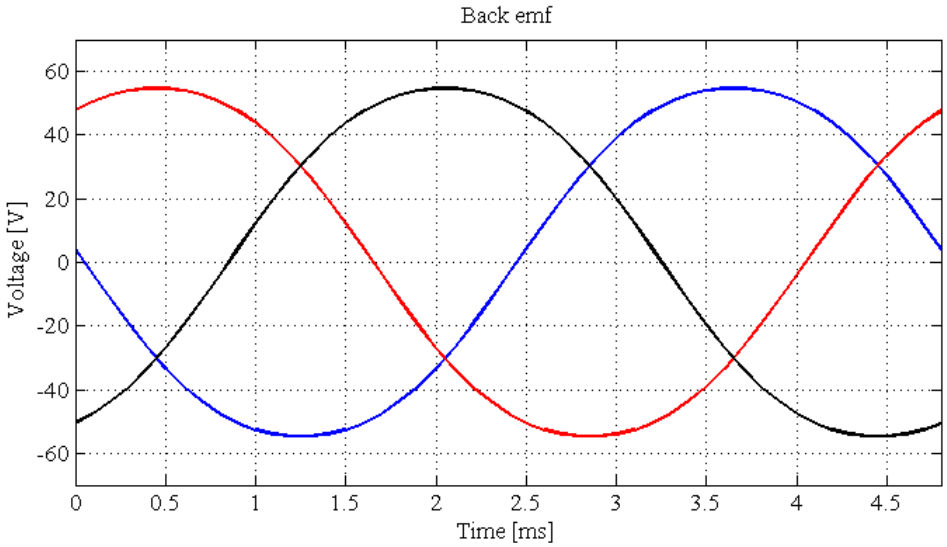


Figure 3.12: back-emf in one three-phase star at rated speed (2500 rpm).

The amplitude of the back-emf is small if compared to the DC Power Supply voltage, which is equal to 270 VDC. This is consequence of the fact that the number of turns of the windings could not be increased for manufacturing reasons. However, despite the consequent low modulation index of the converter could give rise to high current ripple, the large windings inductance and a high switching frequency for the converter contribute to attenuate such current ripple.

Considering a rotating reference frame synchronous with the rotor and having the d-axis aligned with the north pole of the permanent magnet (d-q reference frame), it is possible to calculate the d- and q- axis inductances (L_d and L_q) for different values of the stator current. In particular, the d-axis inductance L_d has been determined by keeping the q-axis current I_q equal to 0 A and varying the d-axis current I_d. The value of the d- and q-axis inductances can be then calculated as described by (3.5).

The d-axis and q-axis inductances as function of the current are shown in Figure 3.13. In can be seen that they are almost constant as a result of low magnetic saturation of the materials. The relatively large inductances value helps reducing the amplitude of the current ripple. The q-axis inductance is slightly different from the d-axis inductance mainly as a consequence of the rotor castellation which causes a minimal pole saliency.

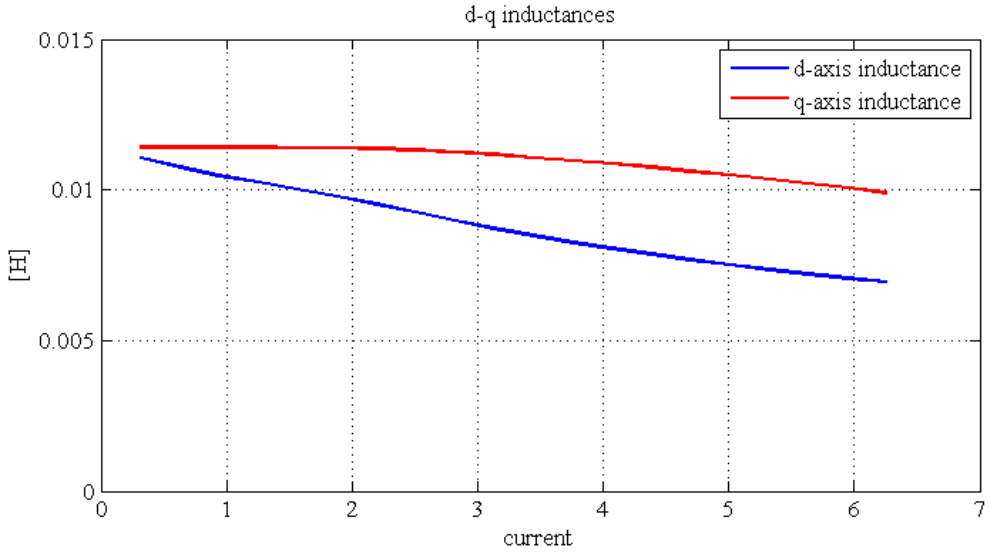


Figure 3.13: d-axis and q-axis inductances vs phase current for one three-phase star.

Figure 3.14 shows the torque versus q-axis current. This curve has been calculated by using the Finite Element model. Different values of I_q current have been applied while keeping I_d equal to zero, and the torque produced for each current have been derived. Since the relationship between torque and current is nearly linear, the torque constant can be calculated, which is the torque produce per unit of current. The torque constant is equal to 0.32 Nm for each ampere applied to one star.

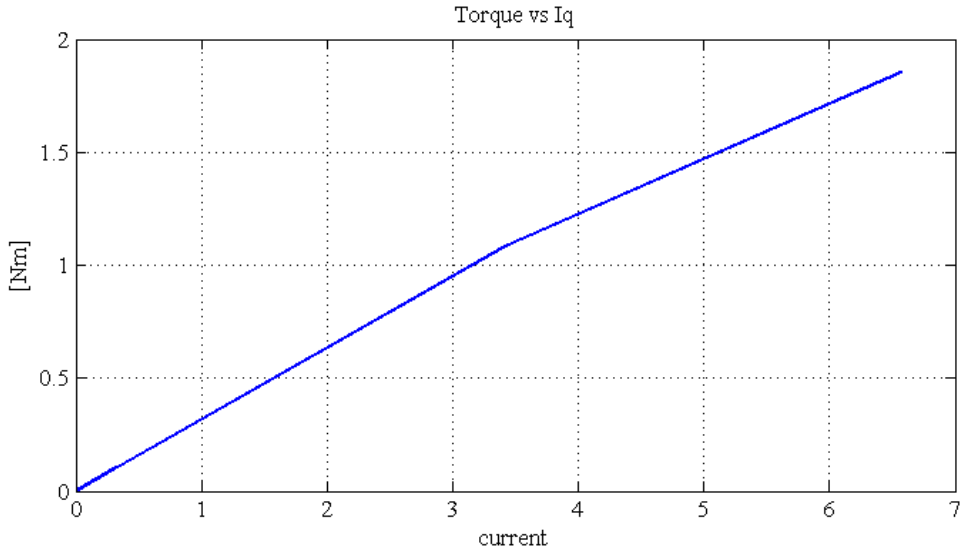


Figure 3.14: Torque vs q-axis current curve for one three-phase star.

Finally, the faulty condition where a three-phase star is shorted has been evaluated. When a three-phase star is shorted, a short circuit current will be circulated in the shorted phases by the rotating magnetic flux of the permanent magnets. A braking torque, whose magnitude is non-linear function of the rotor speed, will be produced by the shorted star [130]. The amplitude of the steady-state current I_{SH} flowing in the shorted star and the braking torque τ_{SH} produced have been calculated analytically.

An analytical representation for the short circuit current and the braking torque can be derived starting from the expression for the voltages v_d and v_q in the d-q reference frame, as reported in (3.6), where *R* is the phase resistance and ω the rotor speed [130].

$$v_d = Ri_d + \frac{d\Psi_d}{dt} - \omega\Psi_q$$

$$v_q = Ri_q + \frac{d\Psi_q}{dt} + \omega\Psi_d \tag{3.6}$$

Under the condition of three-phase short circuit $v_d = v_q = 0$, and using (3.5-3.6), the short circuit d-q currents I_{dSH} and I_{qSH} at steady state can be demonstrated being as in (3.7).

$$I_{dSH} = -\frac{\omega^2 L_q \Psi_{PM}}{R^2 + \omega^2 L_d L_q}$$

$$I_{qSH} = -\frac{\omega \Psi_{PM} R}{R^2 + \omega^2 L_d L_q} \tag{3.7}$$

Thus, the magnitude of the steady-state current I_{SH} flowing in the shorted star is calculated from (3.7) and it is expressed as function of ω in (3.8).

$$I_{SH} = \sqrt{I_{dSH}^2 + I_{qSH}^2} = \frac{\sqrt{\left(\omega^2 L_q \Psi_{PM}\right)^2 + (\omega \Psi_{PM} R)^2}}{R^2 + \omega^2 L_d L_q} \tag{3.8}$$

The torque τ produced by the motor can be calculated as in (3.9), where p is the number of poles.

$$\tau = \frac{3}{2}\frac{p}{2}\left(\Psi_d i_q - \Psi_q i_d\right) \tag{3.9}$$

Thus, by substituting (3.7) for the d-q currents in (3.9), an expression for the short circuit braking torque τ_{SH} as function of the rotor speed ω is obtained as reported in (3.10).

$$\tau_{SH} = -\frac{3}{2}\frac{p}{2} R \Psi_{PM}^2 \omega \frac{\left(R^2 + \omega^2 L_q^2\right)}{\left(R^2 + \omega^2 L_d L_q\right)^2} \tag{3.10}$$

Figure 3.15 shows the short circuit current as function of ω, calculated using (3.8), whereas Figure 3.16 shows the braking torque as functions of ω, calculated

using (3.10). The parameters used in the equations are derived from the Finite Element simulations and are reported in Table 3.9.

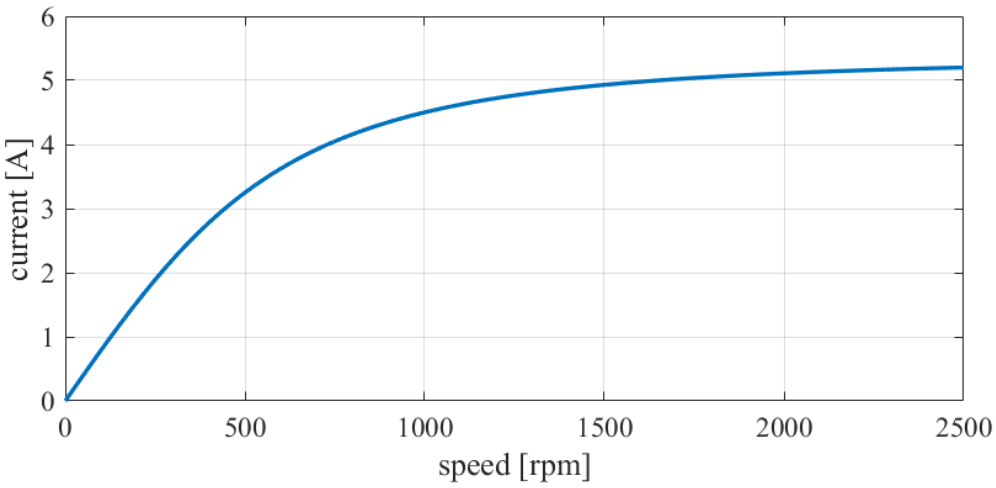


Figure 3.15: One three-phase short circuit steady-state current vs rotor speed.

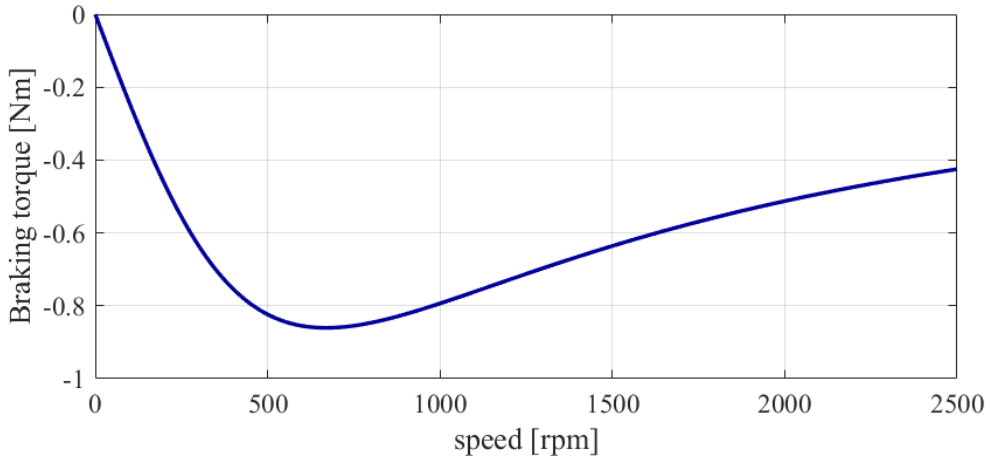


Figure 3.16: Braking torque due to one three-phase short circuit vs rotor speed.

Parameter	**Value**
Phase resistance R	5.24 Ω
Permanent Magnet Flux Ψ_{PM}	0.0418 Wb
d-axis inductance L_d	7.78 mH
q-axis inductance L_q	10.47 mH
Pole Pair number p	5

Table 3.9: Values of the parameters derived with the Finite Element method for the analytical computation of the short circuit current and braking torque.

Figure 3.15 shows that the maximum short circuit current at steady-state is equal to 5.2 A, which is reached for the rated rotor speed of 2500 rpm. Although the current is more than 3 times higher respect to the current flowing during healthy conditions, the possible over-temperatures in the interested slots would not influence the temperature in the healthy phases. Indeed, since the motor operates for a short amount of time and in each slot there are the coils of one phase only, then different slots can be considered as thermally isolated, as it will be shown in Chapter 4.

From Figure 3.16 it can be seen that the maximum braking torque is equal to 0.86 Nm, which is for the case of rotor speed equal to 670 rpm. Thus, the healthy three-phase star needs to produce in the worst case 1.86 Nm, which is produced when a peak phase current equal to 5.91 A flows in the healthy star. However, this high value of current is required only during the retraction of the landing gear, because during the extension operation the braking torque helps decelerating the deployment of the dispositive.

The results of the analysis of the thermal behaviour of the motor are reported in Chapter 4, where an investigation on the thermal modelling of electrical machines for short time duty applications is carried out.

In the next section, the results of the experiments conducted on the manufactured motor for validating its performance are presented.

3.5 Experimental validation of SMPM motor's performance

In this section, the results collected from a series of tests performed on the motor designed for the EMA are presented. The aim of the tests is to experimentally evaluate the performance of the motor, as well as to compare the experimental results to the finite element results determined in Section 3.4.

3.5.1 The test setup

The test bench used for testing the motor is shown in Figure 3.17. An Industrial Parker Internal Permanent Magnet drive was used as load and was coupled to the designed motor. A dSpace platform was used to drive the motor of the EMA.

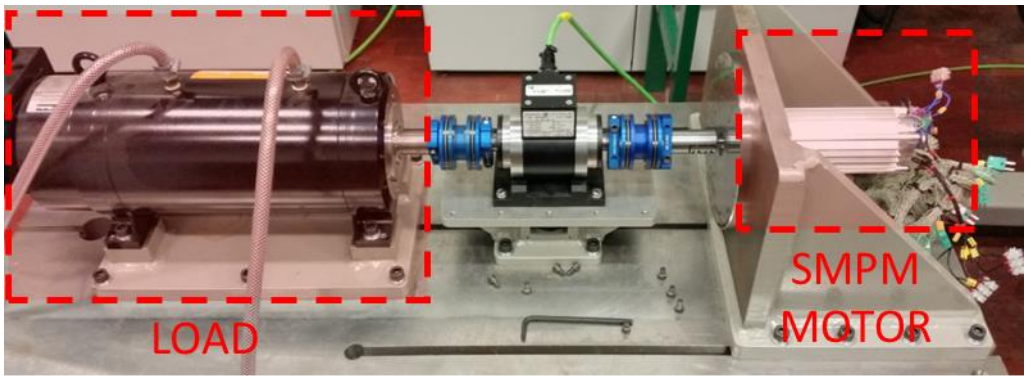


Figure 3.17: Test bench used for testing the motor of the EMA.

The phase resistance has been measured using a Fluke 8808A digital multimeter. The average measured phase resistance was 5.26 Ω respect to the predicted value of 5.24 Ω.

3.5.2 The back-emf

The first test conducted was aimed at measuring the back-emf induced in the windings. During this test the load motor has been mechanically coupled to the SMPM motor. The load motor was speed controlled at the maximum speed of the application, which is 2500 rpm, whilst the SMPM motor's phases were left open. Three differential voltage probes have been connected to the motor's terminals in order to measure the line-to-neutral voltage of the three phases of one star. Figure 3.18 shows the measured back-emf when the rotor is rotating at 2500 rpm, compared to the finite element simulation results.

Using the measured back-emf, it is possible to derive the permanent magnets flux. Indeed, the fundamental of the permanent magnet flux linking the three phases of one star can be expressed as in (3.11), where Ψ_{PM} is the peak of the permanent magnet flux, ω_{el} is the electrical speed which is equal to the mechanical speed multiplied by the pole pairs number, and *t* is the time.

$$\begin{aligned} \lambda_{aPM}(t) &= \Psi_{PM}\cos(\omega_{el}t) \\ \lambda_{bPM}(t) &= \Psi_{PM}\cos(\omega_{el}t - \frac{2}{3}\pi) \\ \lambda_{cPM}(t) &= \Psi_{PM}\cos(\omega_{el}t - \frac{4}{3}\pi) \end{aligned} \tag{3.11}$$

Since the phase voltage is equal to the time derivative of the flux linkage, the back-emf can be represented as in (3.12).

$$E_a = \frac{d\lambda_{aPM}}{dt} = -\Psi_{PM}\omega_{el}\sin(\omega_{el}t)$$

$$E_b = \frac{d\lambda_{bPM}}{dt} = -\Psi_{PM}\omega_{el}\sin\left(\omega_{el}t - \frac{2}{3}\pi\right) \quad (3.12)$$

$$E_c = \frac{d\lambda_{cPM}}{dt} = -\Psi_{PM}\omega_{el}\sin\left(\omega_{el}t - \frac{4}{3}\pi\right)$$

Thus, from (3.12), it follows that the peak of the fundamental of the permanent magnet flux linkage is as in (3.13), where E_{apeak} is the peak value of E_a.

$$\Psi_{PM} = \frac{E_{apeak}}{\omega_{el}} \quad (3.13)$$

Applying the measured peak value of the back-emf in (3.13), it is obtained Ψ_{PM} equal to 0.0419 Wb, in agreement with the results of the finite element analysis, where Ψ_{PM} was found equal to 0.0418 Wb.

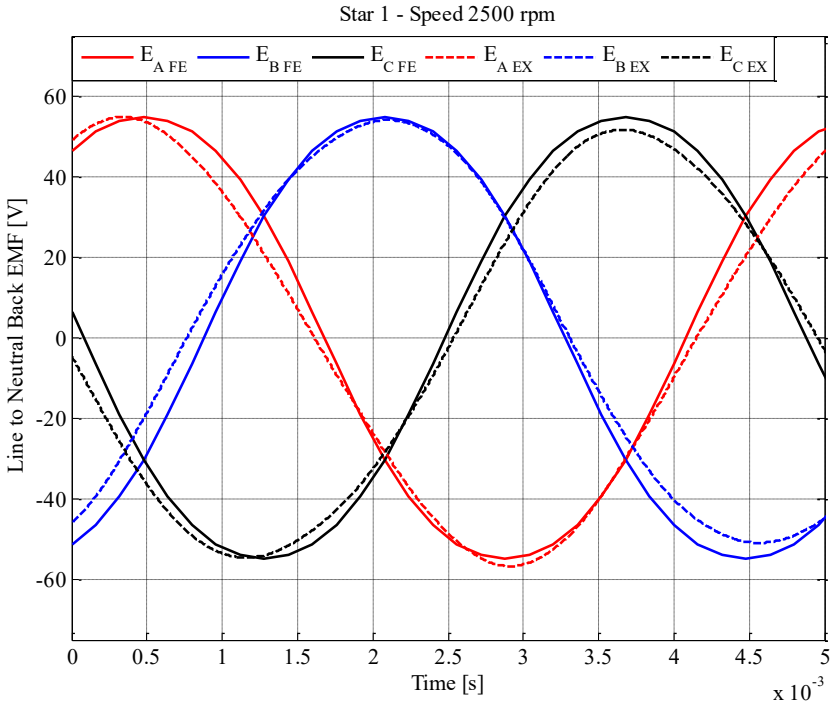


Figure 3.18: Comparison between experimental (continuous line) and finite element (dashed line) line-to-neutral back-emf when the rotor speed is equal to 2500 rpm.

The THD of the experimental back-EMF is equal to 2.4% of the fundamental. Figure 3.19 shows a comparison between the Fast Fourier Transform of the line-to-neutral back-emf measured from the experiment and computed from the Finite Element results. The small discrepancies can be safely associated to manufacturing and measurements tolerances.

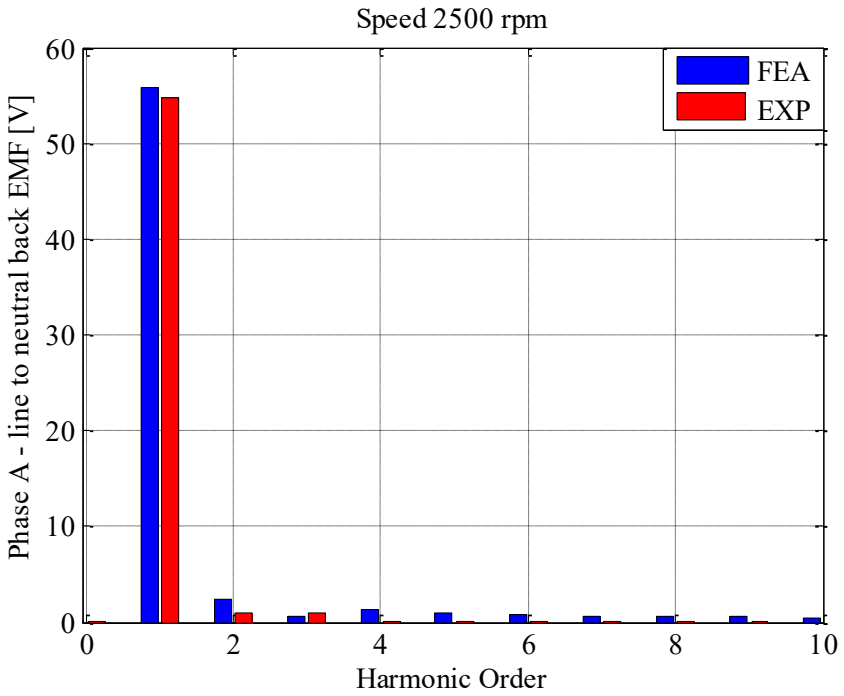


Figure 3.19: Comparison between experimental (red) and finite element (blue) FFTs of the line-to-neutral back-emf at 2500 rpm.

3.5.3 The torque constant

A specific test has been conducted for determining experimentally the torque constant of the motor. During this test, the load motor was coupled to the designed motor. The load motor was speed controlled at 2500 rpm. The motor under test was current controlled. The torque developed by the motor was

measured with a Magtrol torquemeter TMHS-309-111. A q-axis current was applied during the experiment and the torque produced was acquired. The test has been repeated for I_q from 0 to 4.5 A, with steps of 0.25 A. Figure 3.20 shows a comparison between the experimental results and the finite element modelling results for the torque vs. I_q curve. It can be noticed that the experimental results confirm the curve calculated from the simulations.

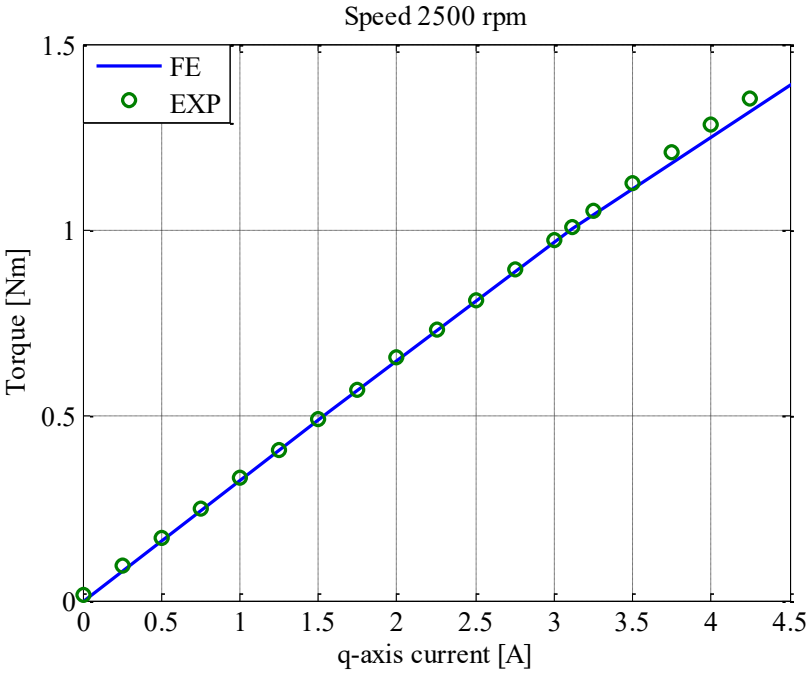


Figure 3.20: Experimental (green dots) and finite element (blue line) torque vs. q-axis current curve for one three-phase star.

3.5.4 Short circuit conditions

A final experiment has been conducted with the aim of validating the performance of the motor when a three-phase short-circuit is experienced by a three-phase star. In particular, the curves of the short circuit current and of the

braking torque as function of the rotor speed have been reproduced experimentally.

As for the previous test, the load motor has been mechanically coupled to the SMPM motor and has been speed controlled. One star of the designed motor was left unconnected, whilst the other star's terminals were connected to a switch whose function is to open or short circuit the three phases' terminals. The current in the three phases was measured using three current probes. The test has been repeated for different rotor speeds, from 0 to 1500 rpm, with steps of 75 rpm. For each test, the switch was initially open and a constant speed was imposed by the load motor. Then, the switch was closed in order to inject the three-phase short circuit of one star.

Figure 3.21 and Figure 3.22 show a comparison between the analytical estimation and the experimental results for the short circuit phase current and the braking torque, respectively. The discrepancy between experimental and analytical results can be partially justified by the increase of the winding temperature during the experimental tests, which causes an increase of the electric resistance. Consequently, there will be a reduction of the short circuit current and a different behaviour for the braking torque.

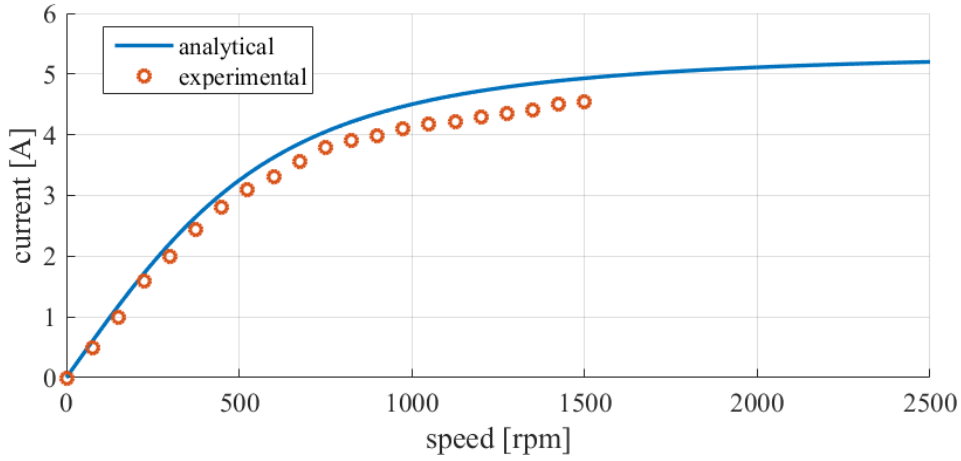


Figure 3.21: Analytical (blue line) and experimental (orange dots) one three-phase short circuit steady-state current vs. rotor speed.

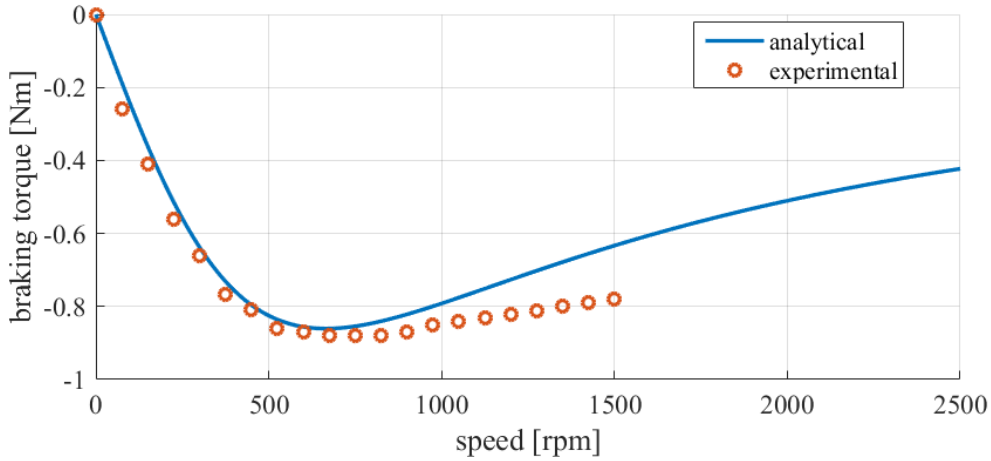


Figure 3.22: Analytical (blue line) and experimental (orange dots) one three-phase short circuit steady-state braking torque vs. rotor speed.

3.5.5 Comparison between simulation and experimental results

Table 3.10 shows a comparison between the results obtained from simulations and experimental tests. A detailed description of the thermal model adopted and of the experimental temperature measurements are provided in Chapter 4. At the design stage, the LPTN employed for the temperature estimations was the one with the parameters untuned.

	Simulation	Experimental
Torque constant per star [Nm/A]	0.32	0.32
Voltage constant [V/rpm]	0.0219	0.0218
back-emf fundamental amplitude @2000 rpm [V]	54.8	54.7
back-emf THD	0.053	0.024
PMs flux linkage [Wb]	0.0419	0.0418
Phase resistance [Ω]	5.24	5.26
Max. temperature during healthy operations [°C]	81.6	78.1
Max. temperature during emergency operations [°C]	174.2	185.7

Table 3.10: Comparison between simulations and experimental results.

3.6 Conclusions

In this chapter, the design of a SMPM motor for an EMA has been presented. The application of the actuator is the retraction and extension of a mid-lift helicopter landing gear. The main challenge was to optimize the actuator weight whilst assuring the high level of reliability required for aerospace applications.

A trade-off study was first conducted in order to identify the crucial parameters aimed at minimizing the overall weight of the actuator. The reliability of the electrical subsystem of the actuator has been enhanced by including redundancy of the power lanes, which reduces the risk of loss of operations for the actuator.

The motor has been designed by using the Finite Element method for modelling the electromagnetic field in the machine and a LPTN for modelling the temperature distribution in the motor. The experiments conducted on the manufactured motor allowed validating the performance predicted by the models.

As the actuation of the landing gear is a short-time duty application, the motor does not reach a thermal equilibrium during operations. At the design stage, this characteristic has been exploited by setting high values of current density in the stator slots for reducing the motor weight. In fact, with respect to an equivalent motor designed for continuous operations, where the current density is set in order to keep the steady-state slot temperature below a certain level, in short-time duty applications this threshold is imposed to the temperature reached at the end of the working cycle. Thus, the current density in the slots has been maximized in such a way that, during operations, the maximum temperature reached in the slot is below the thermal class temperature of the windings' electrical insulation.

Because of the high value of current density, steep thermal cycles will be experienced by the electrical insulation of the windings. Thus, an accurate thermal model is required for accurately predicting the transient thermal behaviour of the motor. For this reason, a thorough investigation on thermal modelling for transient temperatures has been conducted and the results are reported in Chapter 4.

The high temperatures and temperature gradients experienced by the electrical insulating materials, give rise to concerns about the reliability of the insulating system. In fact, although the degradation of the insulation caused by thermal ageing should not be excessive, having limited the maximum temperature in the slots, thermo-mechanical stress related to the thermal cycles could accelerate the insulation ageing and thus lead to early failures.

Since the effect of thermal cycling on enamelled wires of small dimensions is not extensively treated in literature, an investigation on the ageing due to thermal cycling for random wound magnetic wires has been conducted. The results of this analysis are reported in Chapter 5.

Chapter 4
Thermal Modelling of Electrical Machines

In this chapter, a LPTN is firstly presented, which has been developed for modelling the temperature distribution within the SMPM motor designed for the EMA of the helicopter landing gear, as shown in Section 4.2. An experimental evaluation of the thermal behaviour of the designed motor and a comparison with LPTN predictions are presented in Section 4.3. A fine-tuning procedure for enhancing the accuracy of the LPTN parameters, based on a Sequential Quadratic Programming (SQP) algorithm is then introduced in Section 4.4. Finally, in Section 4.5 a novel analytical thermal model has been derived from the presented LPTN, which features a reduced computational effort.

4.1 Introduction

The thermal analysis of the motor is particularly important for the application under study in this work. The system under investigation is designed for a short-time duty application. Hence, high current density values in the stator slots will be exploited to increase the torque density of the motor [54]. Thus, high temperatures and temperature gradients are experienced by the motor during operations. Since a high level of reliability is required for the actuator, it is important to estimate the motor temperatures. This is done, by the proposed thermal model, in order to verify that the instantaneous temperatures are always below the safety levels set by the materials properties.

A LPTN was chosen because of its perceived advantages related to the low computational effort required to operate the model. This is an important feature especially for applications where a thermal equilibrium is not reached. In fact, an evaluation of the temperature dynamics during operation is required, which makes prohibitive the implementation of numerical methods [65]. Also, for the application considered multiple simulations for different operating modes (healthy and emergency operations) are needed, making even more advantageous the employment of an efficient thermal model.

4.2 The Lumped Parameter Thermal Network model

In this Section, the work done to develop the LPTN implemented for modelling the thermal behaviour of the motor shown in Figure 3.6 is presented. During the design stage, the definition of the model's parameters has been based on the

physical properties of the materials involved, the geometry of the motor and empirical equations available in literature. This unavoidably causes limitations to the model accuracy. For this reason, conservative values have been chosen for the most critical parameters of the LPTN, in order to ensure an optimal design of the final motor.

4.2.1 Developing the LPTN

A LPTN models the heat flow and the temperature distribution inside the motor by means of a thermal circuit, which is composed of heat sources, thermal resistances and thermal capacitances. The thermal network can be considered as equivalent to an electric circuit, where the potential of each node represents the temperature in the portion of motor represented by that node. In the equivalent circuit, the capacitors model the thermal masses, the resistances constitute the opposition to the heat flow through the components, the current represents the heat flow through the motor components and the heat sources are modelled as current sources connected to the nodes where they are located. Each node of the LPTN corresponds to a portion of motor and its potential is the average temperature in that portion [68].

The higher the number of nodes, the more detailed is the temperature distribution estimation within the motor [58]. On the other hand, the computational effort of the model is higher for more complex networks. A trade-off study between accuracy and efficiency of the model is mandatory. In general, assuming uniform thermal properties in each portion of motor represented by a node, then the partitioning of the motor into sections is done in such a way take advantage of operational and geometrical similarity. The heat exchange between different

motor components is modelled by the resistors connecting different nodes. Therefore, the accuracy of the LPTN relies also on the selection of the most suitable nodes distribution.

In this work, a 7-node LPTN has been developed for the motor shown in Figure 3.6. A generic schematic of the thermal circuit is shown in Figure 4.1. The nodes labelled with the same red number are at the same potential (i.e. same temperature). The initial potential of the thermal masses is set equal to ambient temperature in order to correctly represent the temperature distribution of the motor before operations. At this stage, for the sake of clarity, the circuit is kept complete in order to emphasize the heat paths that each branch of the network is modelling. Table 4.1 lists the meaning of the parameters shown in Figure 4.1.

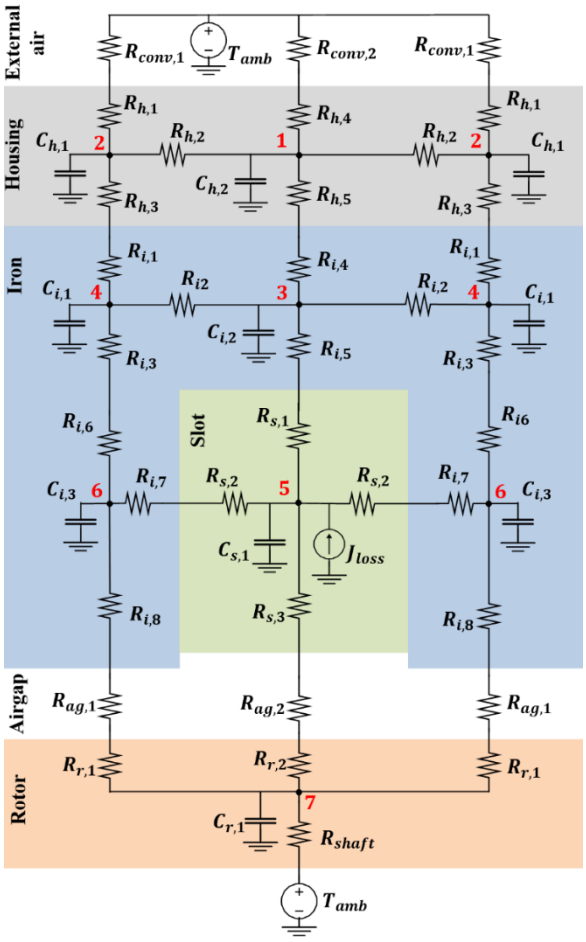


Figure 4.1: Schematic of the LPTN which models the SMPM under investigation.

Symbol	Meaning
$R_{conv,j}$	j-th convection resistance between ambient and housing external surface
$R_{h,j}$	j-th conduction resistance in the housing
$R_{i,j}$	j-th conduction resistance in the stator iron
$R_{s,j}$	j-th conduction resistance in the stator slot
$R_{ag,j}$	j-th conduction resistance in the airgap between rotor and stator
$R_{r,j}$	j-th conduction resistance in the rotor
R_{shaft}	Axial conduction resistance in the shaft
$C_{h,j}$	j-th thermal mass in the housing
$C_{i,j}$	j-th thermal mass in the stator iron
$C_{s,j}$	j-th thermal mass in the stator slot
$C_{r,j}$	j-th thermal mass in the rotor
J_{loss}	Joule losses heat source
T_{amb}	Ambient temperature

Table 4.1: Meaning of the symbols in Figure 4.1.

As mentioned above, the symmetries of the motor can be exploited and a full evaluation of the motor can be achieved by modelling only a section of the motor [131]. In this case, this led to model only a 12^{th} of the full motor. The section of motor shown in Figure 4.2, includes an entire slot pitch, which is the area of most interest for our investigation. In Figure 4.2, nodes 1 and 2 represent a portion of housing, nodes 3 and 4 portions of stator yoke, node 5 the stator slot, node 6 the stator tooth, and node 7 a portion of the rotor.

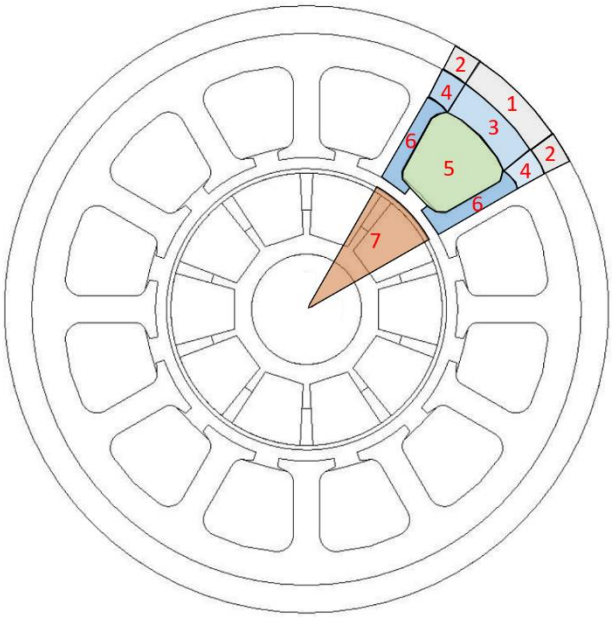


Figure 4.2: Correlation between LPTN nodes and portion of motor interested.

Since the motor considered has a random wound winding configuration, it is not easy to determine the actual distribution of different materials (copper, insulation, etc.) in the slot. For this reason, it is common practice to represent the slot as a lumped anisotropic material which represents all these different materials [78]. The rotor is considered as a single element because of the similar thermal properties of its main components, which are the PMs and the back iron.

The only heat source considered is the Joule loss produced by the electrical current flowing in the windings. This is because for the application at hand, all the other losses (iron and PM losses) are of a much smaller proportion than the I^2R loss of the copper. A FE analysis, using the model developed in Chapter 3 was done to confirm this and the loss components for the typical duty cycle of the machine is shown in Figure 4.3. This is mainly due to the high slot current density and relatively small rotating speed. Considering that the main scope of

this analysis is to predict the winding temperature, then it can be assumed that the contribution of other losses is negligible, especially because we are in the case of short-time duty applications [58]. This assumption has also been verified experimentally, as shown later in Section 4.3.

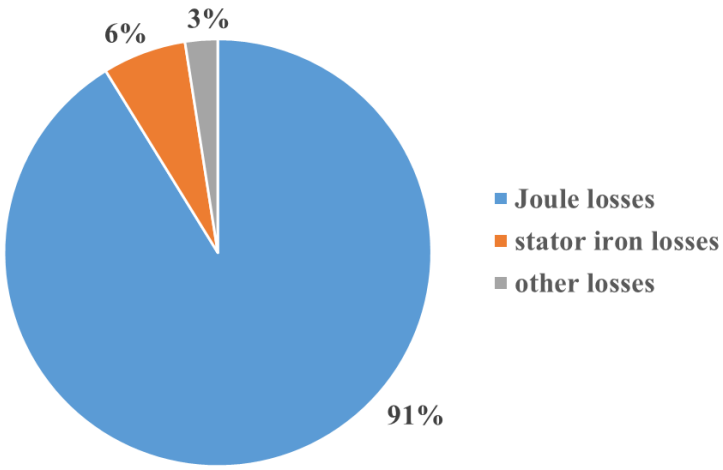


Figure 4.3: Motor losses distribution during operations.

It has to be remarked that for the LPTN considered herein, it is assumed that the heat dissipation in the axial direction is negligible [52]. Only an axial heat path through the rotor shaft is included for representing the heat dissipation from the rotor to the external ambient.

4.2.2 Thermal network parameters definition

The accuracy of any LPTN relies on a careful definition of its parameters. During the design stage, the parameters can only be chosen on the base of the properties of the materials involved and the geometry of the motor. The parameters do not take into account a number of uncertainties such as the thermal resistance due to

the contact surface between different materials and the non-uniform temperature distribution within the area covered by a single node. However, the effect of these uncertainties can be taken into account with specific tuning procedures based on experimental results [75], [70], as will be illustrated in Section 4.3. In this section, an overview of the calculation of both the thermal resistances and thermal capacitances shown in Figure 4.1 is provided. These calculations refer to the motor design stage, when a prototype of the motor was not available.

The heat transfer within the motor is exclusively by conduction. The heat transfer through the airgap between stator and rotor can also be modelled as a conduction problem [132]. This assumption is valid for low speed rotors and small airgaps, where the air has predominantly a laminar shear flow [133]. The heat dissipation from the housing outer surface to ambient is by convection only.

The value of the resistances representing the heat flow by conduction can be represented by (4.1) and (4.2), which are for the tangential and radial heat transfers, respectively [134].

$$R_{tangential} = \frac{l}{kA_{cond}} \tag{4.1}$$

$$R_{radial} = \frac{\ln\left(\frac{r_o}{r_i}\right)}{2\pi kL} \tag{4.2}$$

In (4.1), l is the path length of the portion of motor considered, k the thermal conductivity of the material, A_{cond} the conductive surface. In (4.2), r_o and r_i are the outer and inner radius of the portion of annulus considered and L is the stack length of the motor. Equation (4.1) is used also for calculating the axial heat

transfer resistance through the shaft, substituting half the shaft length in place of l and a 12th of the shaft cross-section area in place of A_{cond}.

The convective resistance $R_{conv;j}$ which represents the heat dissipation from the housing external surface to the ambient can be calculated using (4.3), where $A_{conv,j}$ is the housing external surface area, and h_{ext} is the convection heat transfer coefficient.

$$R_{conv,j} = \frac{1}{A_{conv,j} h_{ext}} \tag{4.3}$$

The thermal masses C have been calculated as in (4.4), where m is the mass of the portion of motor considered and c_h the specific heat of the material present in that portion.

$$C = mc_h \tag{4.4}$$

The coefficients k and c_h representing the thermal conductivity and the specific heat respectively, can be collected from the data sheets of the materials employed and are reported in Table 4.2.

Material	**Thermal conductivity [W/(m°C)]**	**Specific heat [J/(kg°C)]**
Aluminium (housing)	204	910
M270-35A (stator laminations)	31	450
Resin and insulation (slot)	0.2 – 0.26	1000 - 1300
Copper (slot)	385	386
Recoma26 (PMs)	12.8	390
17-4 PH Stainless steel (rotor)	17.9	460

Table 4.2: Thermal properties of the motor's materials.

The equivalent slot thermal conductivity coefficient k_{eq} can be estimated using the empirical (4.5) [135], where k_{copper} and k_{ins} are the thermal conductivity of the conductor and the insulating material inside the slot, respectively, whereas K_{FF} is the slot fill factor.

$$k_{eq} = k_{ins}\frac{(1+K_{FF})k_{copper}+(1-K_{FF})k_{ins}}{(1-K_{FF})k_{copper}+(1+K_{FF})k_{ins}} \tag{4.5}$$

The equivalent slot thermal capacitance $C_{s,1}$ is calculated according to (4.6) [58], where the sum of the thermal capacitances of the different materials present in the slot is taken into account. The end-winding mass is included in the calculation of the slot total mass m_{slot}. $c_{h,copper}$ and $c_{h,ins}$ are the specific heat coefficient of the conductor and the insulating materials, respectively.

$$C_{s,1} = K_{FF}m_{slot}c_{h,copper} + (1-K_{FF})m_{slot}c_{h,ins} \tag{4.6}$$

Since the rotor is considered as a single material body, the thermal conductivity coefficient for the resistances $R_{r,j}$ is selected equal to the smallest thermal coefficient between the one of the permanent magnets and the back iron materials. The rotor thermal mass $C_{r,1}$ is computed as sum of the permanent magnets and back iron thermal masses.

The Joule losses J_{loss}, which are generated in the slot by the electric current flowing in the windings, are calculated by using (4.7) [11], where R_{el20} is the winding electrical resistance at 20 °C, α_0 is the thermal coefficient of resistivity, T the conductor's temperature and I the rms value of electrical current flowing through the conductor.

$$J_{loss} = R_{el20}\big(1+\alpha_0(T-20)\big)I^2 \tag{4.7}$$

In particular, the temperature T of the conductor in (4.7), is considered uniform and equal to the temperature in the slot as calculated for the node 5 of the implemented LPTN.

4.2.3 SMPM machine operating temperature estimations

The LPTN proposed in Section 4.2.2 has been used during the motor design stage for predicting the operating temperature within the motor during three consecutive landing gear retraction/extension cycles. The temperature rise, during the three operating mode defined in Section 3.3.1, has been predicted. In particular, the following current profiles were selected for the simulation of the three operating modes:

- Healthy operations: a DC current equal to 1.1A (rms value of 1.56A AC) has been applied to both the three-phase stars for 60 seconds;
- Open star emergency operations: a DC current equal to 2.2A (rms value of 3.12A AC) has been applied to one star for 60 seconds;
- Shorted star emergency operations: three consecutive cycles composed of 10 seconds applying 4.18A DC (rms value of 5.91A AC) to one star followed by 10 seconds applying 0.88A DC (rms value of 1.25A AC) to the same star.

During the shorted star emergency operation, the DC current values in the healthy star have been selected on the base of the speed vs. braking torque curve of Figure 3.16. Specifically, during the retraction of the landing gear, the current is such that the torque produced by the healthy star accounts for the required torque and at the same time compensates for the maximum braking torque

generated by the faulty star (0.86 Nm). This means that during retraction the current required in the healthy star is higher than for the case of normal operation. For the extension part of the cycle, where the torque required is partially provided by the braking torque produced by the shorted star, then the current in the healthy star has been set equal to the current necessary for producing the remaining torque, assuming for the braking torque a constant contribution of 0.4 Nm, which is the lowest possible value according to Figure 3.16 for rotational speeds higher than 250 rpm. This simplifying assumption is not critical since the rotor speed is lower than 250 rpm only for 0.4 seconds of the extension period, during which the torque required is lower than the constant torque considered for the application, as it can be seen from the speed profile of Figure 3.2, the torque profile of Figure 3.3 and considering a gear ratio equal to 960:1.

Figure 4.4 shows the current profiles selected for the motor thermal evaluation during the three operating modes.

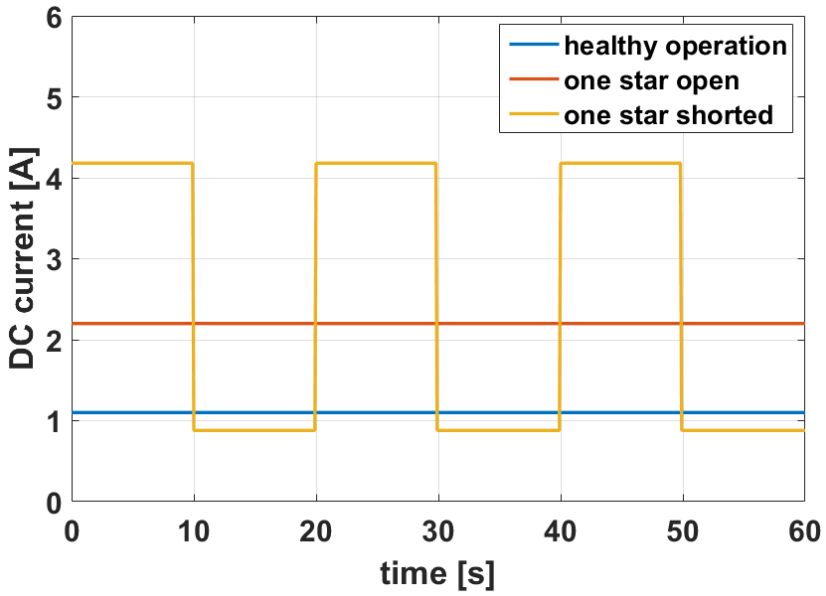


Figure 4.4: DC Current profiles applied for the evaluation of the motor temperature during operations.

For each simulation, the highest application ambient temperature, which is equal to 70°C, has been considered. The scope of the temperature prediction was to verify that the temperature in the slot does not exceed the rated temperature of the winding insulation.

Figure 4.5 shows the operating winding temperature predictions, obtained using the LPTN defined in the last section. It can be noted that in all the three operating modes the maximum temperature does not exceed the threshold value of 180 °C. In particular, during healthy operations the temperature remains below 100 °C, whilst the highest temperature rise is seen when one three phase star is shorted. It is important to note that if this last condition is true, then the shorted star will of course contribute to torque production by creating a braking torque. This means that a slightly higher current is required to circulate in the healthy star to

compensate for this opposition to the rotation of the shaft, which contributes to the increase in temperature of that star.

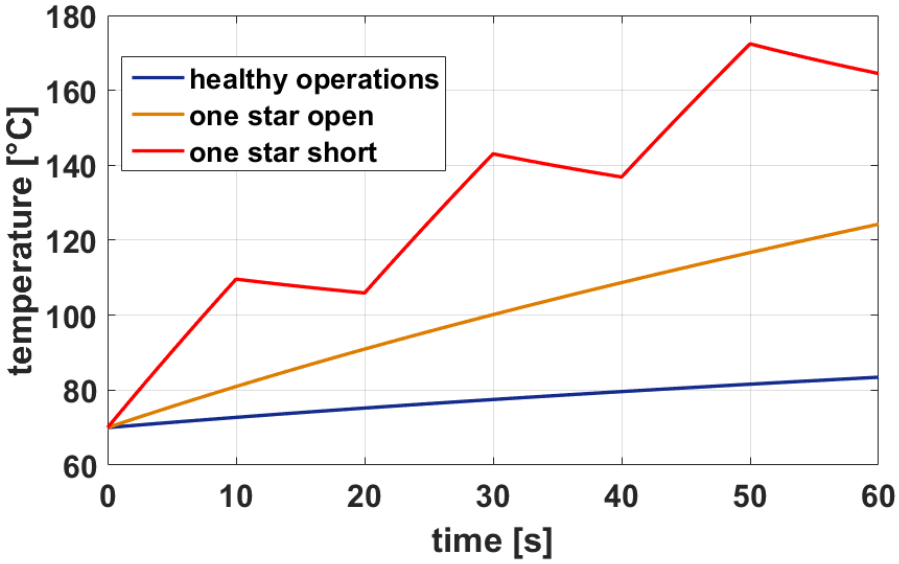


Figure 4.5: Winding temperature predicted by LPTN for the three operating modes of the SMPM motor designed.

4.3 Experimental evaluation of SMPM thermal performance

In this section, the results of the experiments conducted on the SMPM motor in order to evaluate its thermal performance are shown. A preliminary series of tests is first reported, whose scope was to demonstrate the validity of the assumptions made during the thermal modelling process. Subsequently, the results of the experiments carried on for experimentally validating the motor performance during operations are illustrated.

For each test, the temperature in the motor slots has been measured using six type-K thermocouples placed in the core of the slot and acquired with a TC-08 Data Logger at 1 second intervals. Each thermocouple was placed in a different

phase winding. Among the temperatures measured, the highest one was selected as the winding temperature. The use of several thermocouples helps reducing the risk of measurement errors due to poor contact between the thermocouple tip and the winding.

4.3.1 Preliminary thermal experiments results

In this section, the results of a series of preliminary experiments conducted on the SMPM motor for evaluating its thermal behaviour are reported. The scope of the tests is twofold. Firstly, they serve for validating the assumptions made during the definition of the thermal model for the SMPM motor. Secondly, the results are also used as the main basis for the design of an experiment aimed at reproducing the operating conditions of the motor for validation purposes.

4.3.1.1 Validating the assumptions

As described in Section 4.2, the major loss component for the application at hand is the copper loss, where Figure 4.3 highlights that the other losses can be assumed negligible.

In order to verify the validity of this assumption, two comparative tests have been carried out, one where all the losses are present in the motor and another test where only the Joule losses are generated in the motor. For these tests, the same test bench utilized for the work presented in Section 3.5 has been used.

During the first test, the load motor (which is mechanically coupled to the SMPM motor) was speed controlled at 2500 rpm, while the motor under analysis was current controlled and a set point equal to 1.41 A AC was applied. Thus, for

this test, all the heat sources that the motor will generate during operations are included. On the other hand, during the second test the motor is static and a DC current equal to the rms value of the AC current applied in the previous test flows in the windings. This ensures that the Joule losses in the slot are of the same magnitude for both the tests, but in the second test they are the only heat source present.

The windings temperatures were measured via K-type thermocouples distributed in the stator slots. The results from these tests are given in Figure 4.6. Since the two temperature profiles are nearly congruent, especially during the first transient, then it can be concluded that the assumption of considering only the Joule losses for the LPTN does not significantly affect the thermal performance of the machine. Figure 4.7 highlights the mismatch between the two temperature profiles shown in Figure 4.6, where it can be observed that the mismatch is less than 4°C. In particular, during the first 60 seconds of the transient for the temperature profiles of Figure 4.6, the temperature mismatch is less than 1°C, as shown in Figure 4.8. This result highlights the validity of the assumption made.

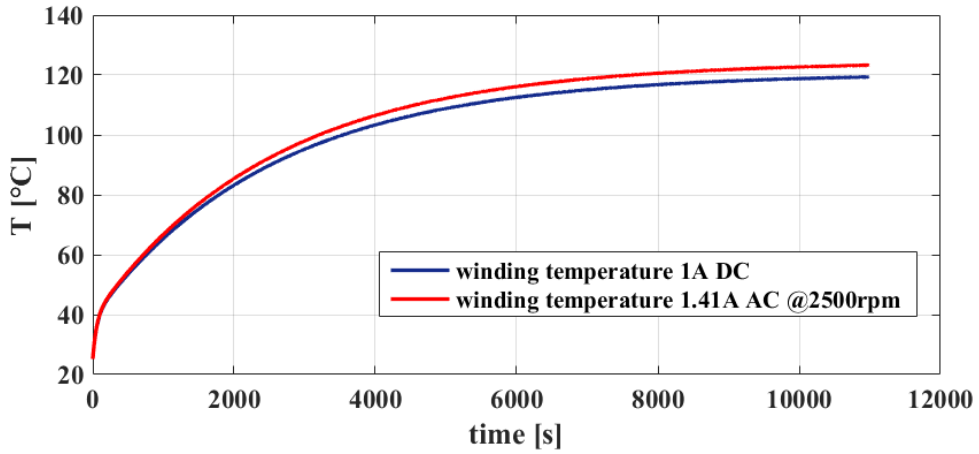


Figure 4.6: Winding temperature profiles for the SMPM at 2500 rpm when 1.41A AC are applied (red) and for the static motor when 1A DC is applied.

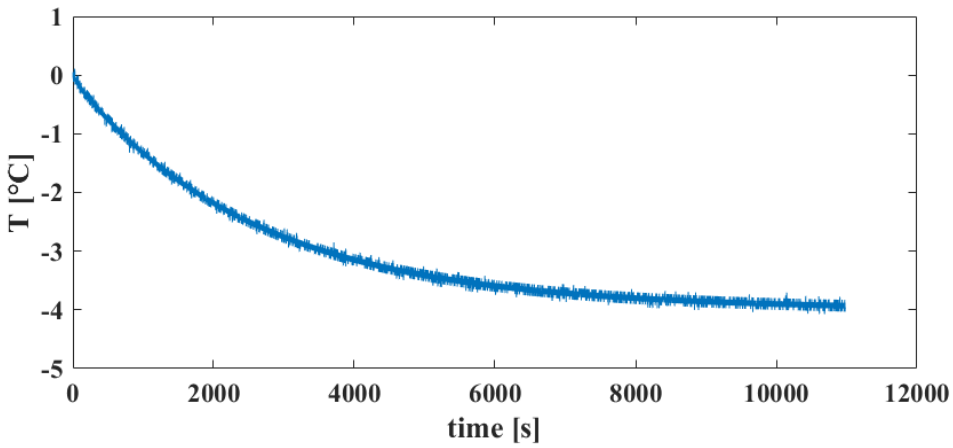


Figure 4.7: Difference between the two temperature profiles depicted in Figure 4.6.

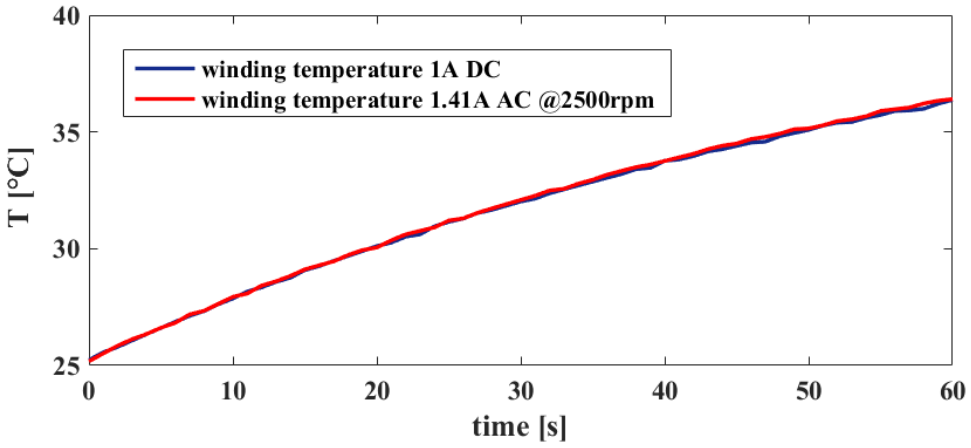


Figure 4.8: Winding temperature profiles for the SMPM at 2500 rpm when 1.41A AC are applied (red) and for the static motor when 1A DC is applied, during the first 60 seconds transient.

The same experiment has been repeated for different current values, where the winding temperature profile has been acquired for the case of rotor spinning at 2500rpm while 0.71 A AC were applied to the stator windings, and for the case of steady rotor and stator current equal to 0.5 A DC. The results of this experiment are shown in Figure 4.9 and Figure 4.10, where it can be noticed that similar results are obtained for different currents applied.

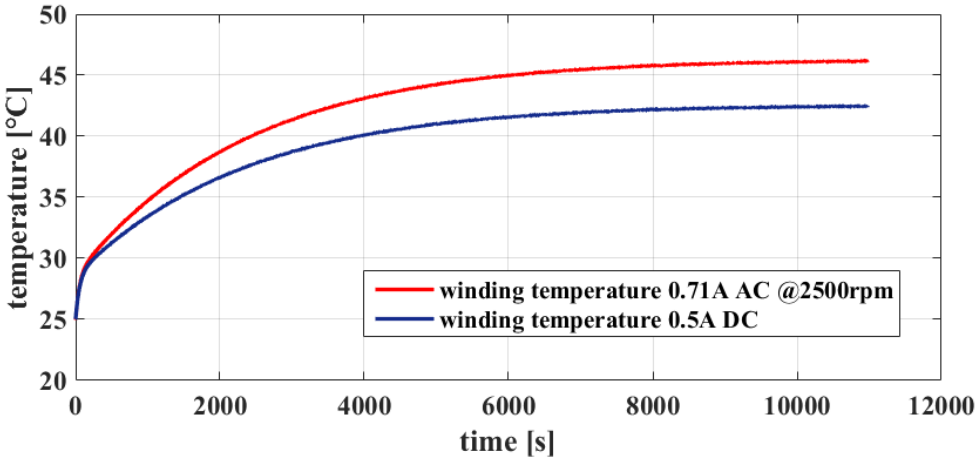


Figure 4.9: Winding temperature profiles for the SMPM at 2500 rpm when 0.71A AC are applied (red) and for the static motor when 0.5A DC is applied.

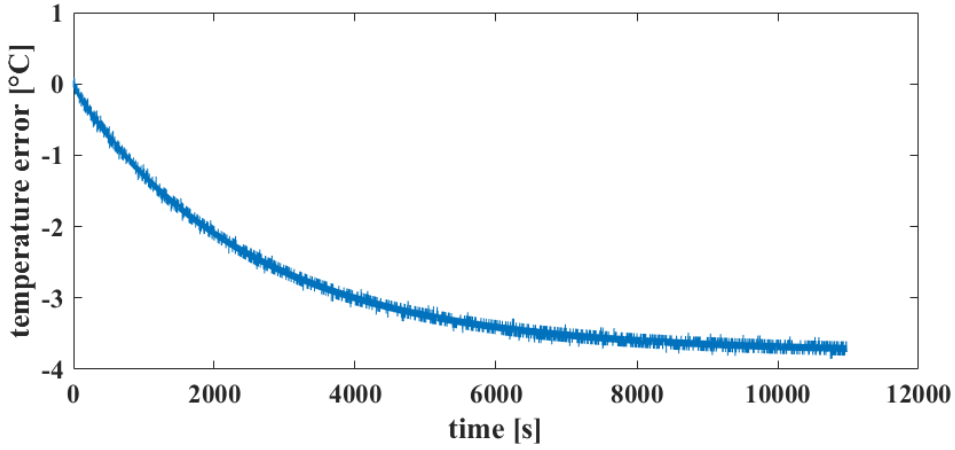


Figure 4.10: Difference between the two temperature profiles depicted in Figure 4.9.

From the results of the above experiments, it can be also deduced that in the Joule losses calculation proximity and skin effects, which can increase the electrical resistance of the conductor [136], are not relevant for the specific application. In other words, it has been checked that the winding temperature profiles are congruent when an AC current or an equivalent DC current, whose value is equal to the rms value of the introduced AC current, is flowing in the windings. This was partly expected, due to the small section adopted for the

windings' conductors and to the relative low fundamental frequency of the motor. Thus, the subsequent experiments have been conducted by applying the equivalent DC current for simplicity reasons.

4.3.1.2 Verifying thermal coupling between stars

The windings of the SMPM under investigation are divided between two independent three phase stars. During the design stage, the two stars have been considered as thermally isolated between each other, due to the winding topology (i.e. single layer concentrated winding). This assumption, if not valid, could cause issues especially during the emergency operations with a three phase star shorted. Indeed, high induced currents circulate in the shorted star and thus high temperatures are reached in the faulty phases. If the heat produced propagates to the healthy phases, this can cause unpredicted over-temperatures in the latter.

For this reason, an experimental investigation has been conducted in order to verify the temperature increase in an open star, due to the thermal effect of the other supplied star. For the experiment, the same test bench as in the previous tests have been used. During the test, a DC current equal to 2.2A has been applied to the phases of a star and the temperature in the slots of the unconnected star was acquired. Figure 4.11 shows the temperature rise both in the fed star and in the disconnected star. It can be seen that in the disconnected star the temperature increase is smaller than 5°C after 60 seconds, which is the duty period of the application. Similar results has been obtained applying different current values to one star, as it is shown in Figure 4.12, where the temperature transients in the open star when the other star is fed with different currents are illustrated. Thus,

the thermal model of the SMPM motor can be designed assuming that different phases are thermally isolated between each other.

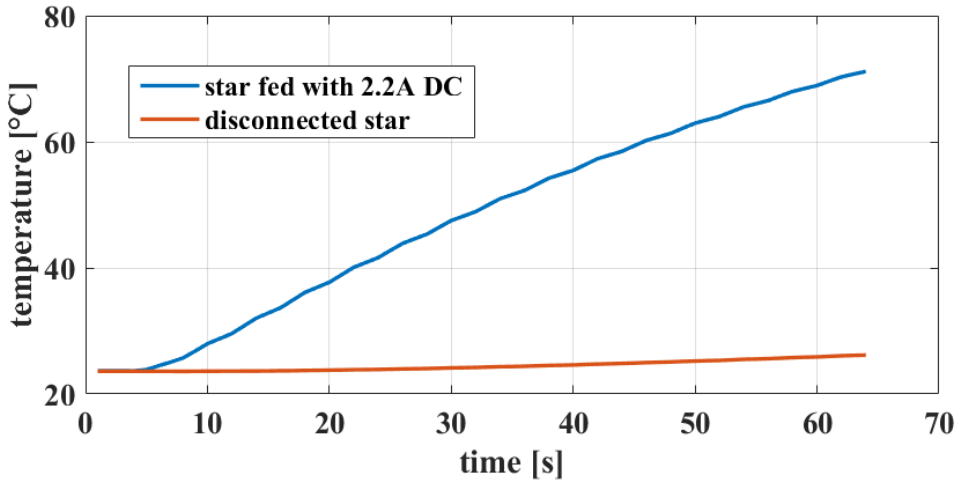


Figure 4.11: Winding temperature for the star fed with 2.2A DC and for the disconnected star.

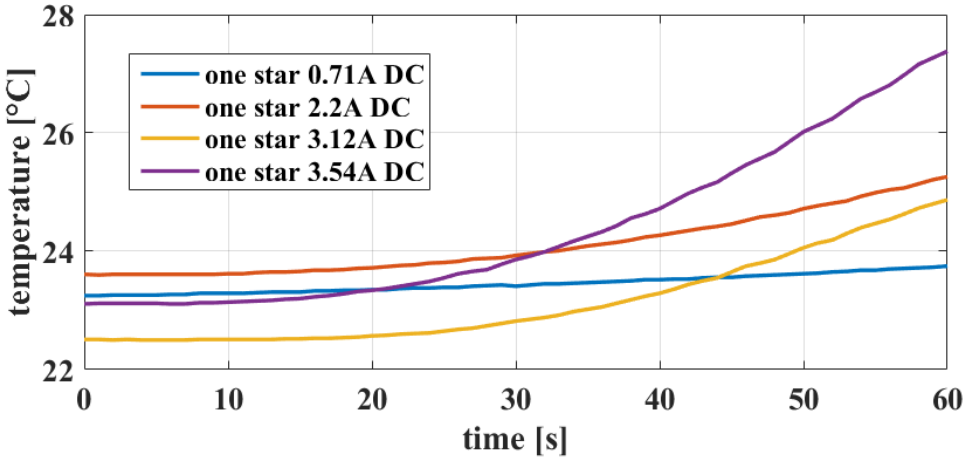


Figure 4.12: Temperature rise in the open star when a current is applied to the other star.

4.3.2 Thermal evaluation during operations

In this section, the results of the experiments conducted for evaluating the thermal performance of the motor during operations are presented. Since the motor is designed for working in a wide range of ambient temperatures, it is

essential to test the motor for the highest ambient temperature considered. Indeed, it is important to notice that for a fixed electric current, the value of the ambient temperature does not simply shift the motor temperature profiles, but also influences the shape of the temperature rise as the heat sources are temperature dependent.

In order to simulate an ambient temperature of 70°C (highest ambient temperature considered for the application), the Espec Test Chamber shown in Figure 4.13 has been used.



Figure 4.13: Espec Test Chamber employed for simulating operative ambient temperature.

4.3.2.1 Verifying the physical set-up

During the experiments, the motor was placed in the test chamber, as shown in Figure 4.14. The motor was placed over a wooden stand in order to minimize the heat dissipation through the metal grill. An interesting point to consider here is the effect of such a different physical setup has on the test-bench where the motor

is attached to the rig, via end-plate and adapter plates. In order to verify whether this aspect is significant, a series of tests were run for both cases. As shown in Figure 4.15, the thermal response of both cases perfectly match during the first 60 seconds transient, for the case of 2.2A DC applied, therefore showing that any results from the proposed setup of Figure 4.14 will be valid also for the machine in its "normal" assembly configuration.

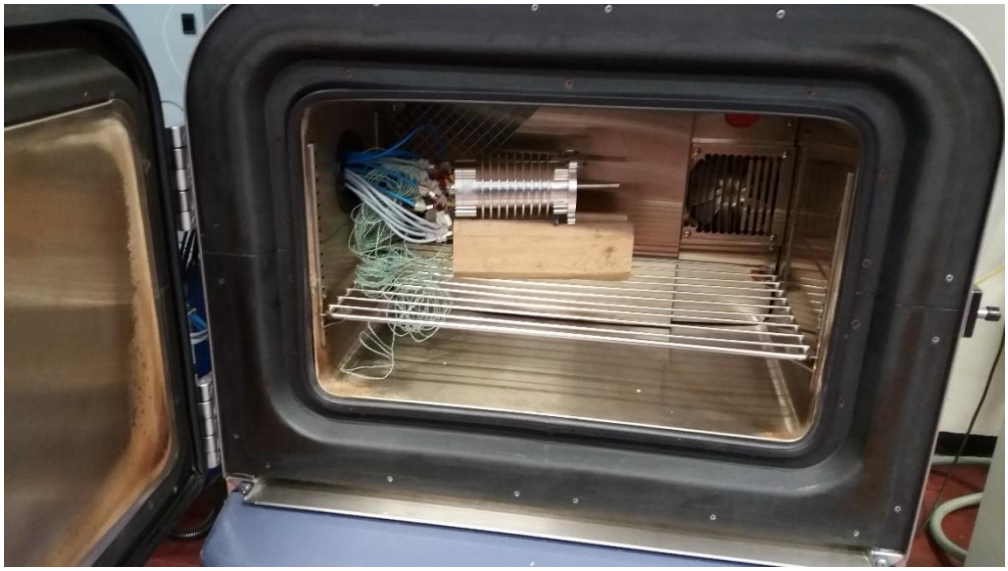


Figure 4.14: SMPM motor placed in the test chamber.

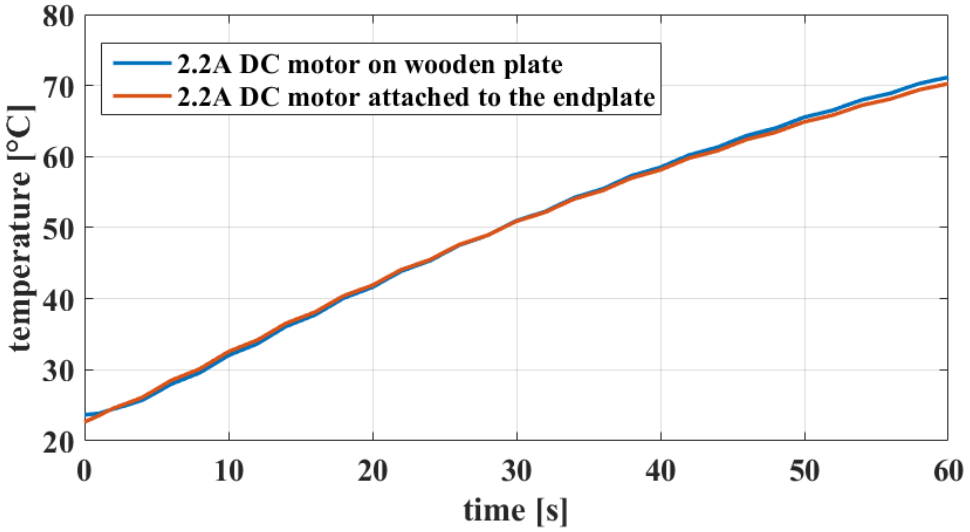


Figure 4.15: Comparison of winding temperature rise for the case of motor placed on the wooden plate and of motor attached to the rig endplate.

4.3.2.2 Tests at 70 °C ambient temperature

For each test, the chamber temperature was set equal to 70°C and the motor was brought to its thermal equilibrium. The three operating conditions introduced in Section 3.3.1 have been tested by applying the same current loads described in Section 4.2.3.

Figure 4.16 shows the winding temperature measured for the three temperature profiles. The initial temperature, which is equal to the ambient temperature, is slightly different for the three profiles (between 67 and 72 °C) because of the tolerances due to the test set-up, including the above-mentioned variances of the test chamber.

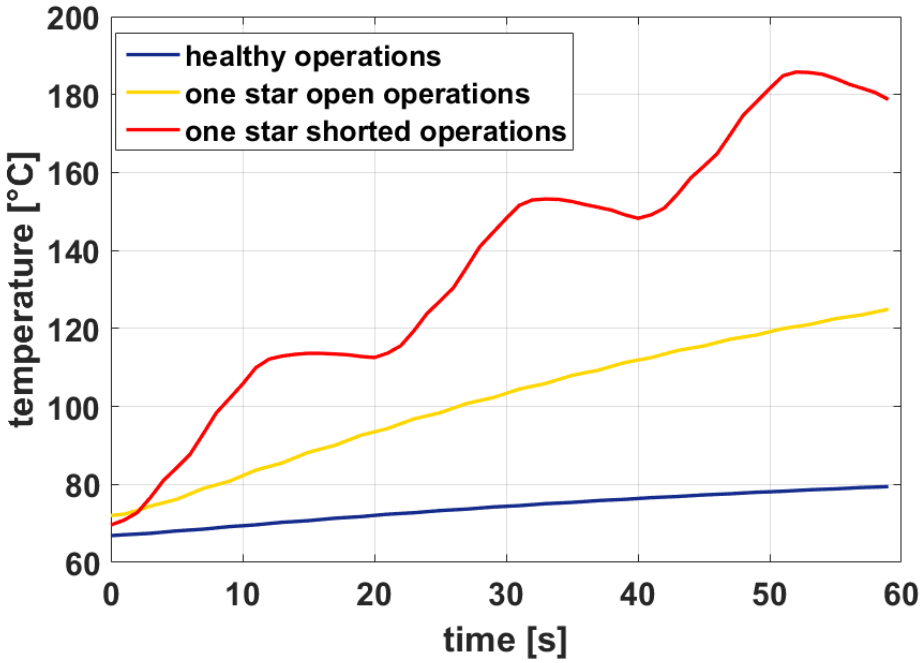


Figure 4.16: Experimental winding temperature profiles for the three operating modes considered, when the motor is placed in the test chamber at 70 °C.

Table 4.3 compares these results with those achieved from the thermal model of Figure 4.5, where it can be observed that the experimental results show a slightly different thermal behaviour of the motor, especially for the critical case of one star shorted operations. In fact, with respect to the maximum temperature predicted with the thermal model, which is equal to 174.2°C, the experimental results show that during the shorted star emergency operations the maximum temperature reached in the slot is 185.7°C. This discrepancy between predicted and measured temperatures could be associated to the thermal model parameters uncertainties introduced in Section 4.2.1. For this reason, in the next section a tuning procedure of the LPTN parameters, based on the experimental acquisitions, will be presented.

Time [s]	Predicted temperature [°C]	Experimental temperature [°C]
Healthy operations		
10	72.7	69.4
30	77.5	74.4
50	81.6	78.1
One star open operations		
10	81.0	82.2
30	100.2	103.4
50	116.7	119.2
One star shorted operations		
10	109.6	109.9
30	143.1	151.6
50	174.2	185.7

Table 4.3: Comparison between predicted and experimental winding temperatures during the three application's duty cycles.

4.4 LPTN parameters fine tuning

In order to improve the accuracy of the LPTN, a fine-tuning exercise can be done based on experimental temperature measurements. This is an often-used methodology that allows to calibrate and tune for some of the unknown aspects of the model. For example, in [75] specific experiments are conducted for identifying the value of single critical parameters, or in [70] a particle swarm optimization has been implemented for identifying all the parameters of a simple LPTN.

4.4.1 The tuning procedure

A tuning procedure for the uncertain parameters of the LPTN designed is proposed. The procedure capitalises on the availability of experimental winding temperature measurements. It allows a considerable improvement in the accuracy of the thermal network in terms of predicting the winding temperature under variable loads both during transient and at steady-state conditions.

The first step of the tuning procedure is the selection of the critical model parameters, which for the case at hand are:

- External convection coefficient h_{ext}
- Conductor electrical resistivity R_{el20}
- Lamination thermal conductivity k_{iron}
- Slot equivalent conductivity k_{eq}
- Slot equivalent specific heat capacity c_{eq}
- Housing specific heat capacity c_{hous}
- Airgap convection coefficient h_{ag}

4.4.1.1 Rationale

The tuning procedure concept is based on the seamless integration of corrective factors for all the parameters involved. The corrective factors multiplying h_{ext} and h_{ag} account for the uncertainties deriving from the heat transfer by convection, which is affected by air turbulences. The one multiplying R_{el20} tunes the Joule losses, which cannot be exactly predicted due to uneven temperature distribution in the slots. The coefficients k_{eq} and c_{eq} are also uncertain because of the complex materials distribution inside the slot and due to uncertainties on

the materials properties. The corrective factor multiplying k_{iron} incorporates the effect of the uncertain thermal resistance of the iron-slot and iron-housing contact surfaces. c_{hous} is multiplied by a corrective factor in order to account for uncertainties deriving from the uneven temperature distribution in the housing.

The main steps of the tuning procedure are:

- Experimental acquisition of winding temperature profiles for different loads (i.e. current values);
- Definition of an objective function representing the error between LPTN predictions and experimental temperature profiles;
- Use of a Sequential Quadratic Programming (SQP) algorithm that finds a set of optimal correction factors which minimize the objective function.

4.4.1.2 Concept

Several temperature profiles are acquired for different current loads with the motor initially at ambient temperature. Each experiment was performed by applying a constant DC current to each phase of the motor and the winding temperature rise was recorded from the initial time of application of the current until the motor reached the thermal equilibrium. In this way, the temperature dynamics either with short and long time constants are taken into account, in the tuning procedure. In order to force the tuning algorithm finding a set of corrective factors, which makes the LPTN accurate in a wide range of load conditions, several temperature profiles at different currents are considered during the test campaign.

An objective function f_{obj} can be defined as in (4.8), which represents the sum of the errors err_i between experimental and predicted winding temperatures for each temperature profile experimentally measured.

$$f_{obj} = \sum_i err_i \tag{4.8}$$

For each temperature profile, the error err_i can be defined as the mean relative error represented by (4.9), where *t* is the time, $t_{0,i}$ and $t_{f,i}$ are the initial and final time respectively for the temperature profile of the i-th current load, whereas $T_{mea,i}$ and $T_{mod,i}$ are the measured and predicted winding temperatures, respectively.

$$err_i = \frac{1}{t_{f,i} - t_{0,i}} \left(\int_{t_0}^{t_f} \left(\frac{T_{mea,i}(t) - T_{mod,i}(t)}{T_{mea,i}(t)} \right)^2 dt \right)^{\frac{1}{2}} \tag{4.9}$$

Thus, the scope of the tuning procedure is to find a set of values for the corrective factors of the uncertain parameters such that the objective function f is minimized. In order to find the optimal value for the corrective factors, a SQP iterative algorithm [137] has been implemented. Each corrective factor has been constrained between 0.1 and 100. The SQP algorithm solution is dependent on the initial value of the variables to be optimized. In fact, although the SQP algorithm is particularly suited for the minimization of non-linear multivariable cost functions, however its limitation is that it is only able to find local solutions. For this reason, the SQP algorithm has been launched several times starting from randomly selected initial corrective factors between 0.1 and 100. Among all the local solutions identified by the algorithm, only the ones which makes the cost

function smaller than a minimum value were kept. Since a unique solution is not guaranteed for the problem, then in case of multiple solutions for any corrective factor, its optimal value closest to 1 is arbitrarily selected.

4.4.1.3 Note

It is important to note that the tuned parameters obtained with this procedure could not have a physical meaning, as the only objective of the procedure is to minimize the winding temperature prediction error. For the same reason, the temperature predictions in the other nodes of the tuned network are not guaranteed to reflect the average temperature in the associated motor area. Finally, since the scope of the tuning procedure is to minimize the winding temperature prediction error with respect to the hottest temperature profile experimentally measured, then the winding temperature of the tuned LPTN cannot be considered as an average slot temperature.

4.4.2 Tuning of the proposed LPTN

The tuning procedure introduced in the last section, has been implemented for the LPTN of Figure 4.1, which has been used for predicting the winding temperature of the SMPM motor shown in Figure 3.6.

4.4.2.1 The test runs

Four experimental winding temperature profiles have been used in the procedure. For each experiment, a constant DC current was applied to all the motor phases which were series connected, and the winding temperature was recorded from the initial time of application of the current until the motor has reached a steady state value. The four currents applied are 0.4, 0.5, 0.9 and 1A

DC. The currents considered are smaller than the operating ones because it was imperative to maintain the winding temperature below 180°C at any physical point at steady state.

While for this application the temperature predictions when the ambient temperature is equal to 70°C (maximum ambient temperature) are of major interest, the temperature acquisitions were conducted outside of the chamber room, as shown in Figure 4.17. Thus, the ambient temperature during the tests was the laboratory air temperature. This choice is due to the consideration that the thermal chamber employed is not capable of strong temperature control. Thus, if long time tests are done with the set-up in this small enclosed environment, then the ambient temperature is sure to rise more than the prescribed setting and therefore this would affect negatively the temperature readings taken. In order to obtain a more realistic temperature profile where the ambient temperature is kept constant, a much larger test chamber would need to be employed, which unfortunately was not available at the time of conducting these experiments.

It is important to highlight that the temperature acquisitions conducted in the test chamber for short operating periods (60 seconds) are very reliable, since the chamber temperature rise time due to the motor heat dissipation can be assumed considerably bigger than 60 seconds.

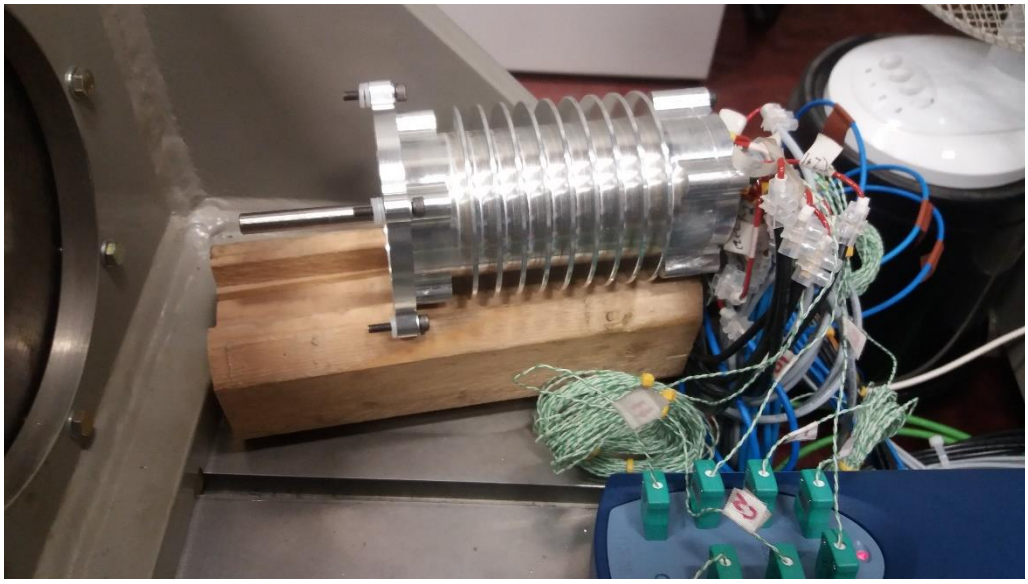


Figure 4.17: SMPM motor test setup for the temperature profiles acquisitions to be used as input of the LPTN critical parameters tuning procedure.

4.4.2.2 Employing the algorithm

The SQP algorithm was launched 10,000 times, starting from random initial sets of corrective factors, in order to find a set of local solutions which minimize the cost function of (4.8), which in turn represents the prediction error between the thermal model and the four temperature profiles considered herein. Figure 4.18 and Figure 4.19 show the corrective factors values for the 100 best solutions in terms of cost function minimization, ordered from the one with smallest prediction error to the one with the highest one. Their values were separated in two graphs for sake of clarity.

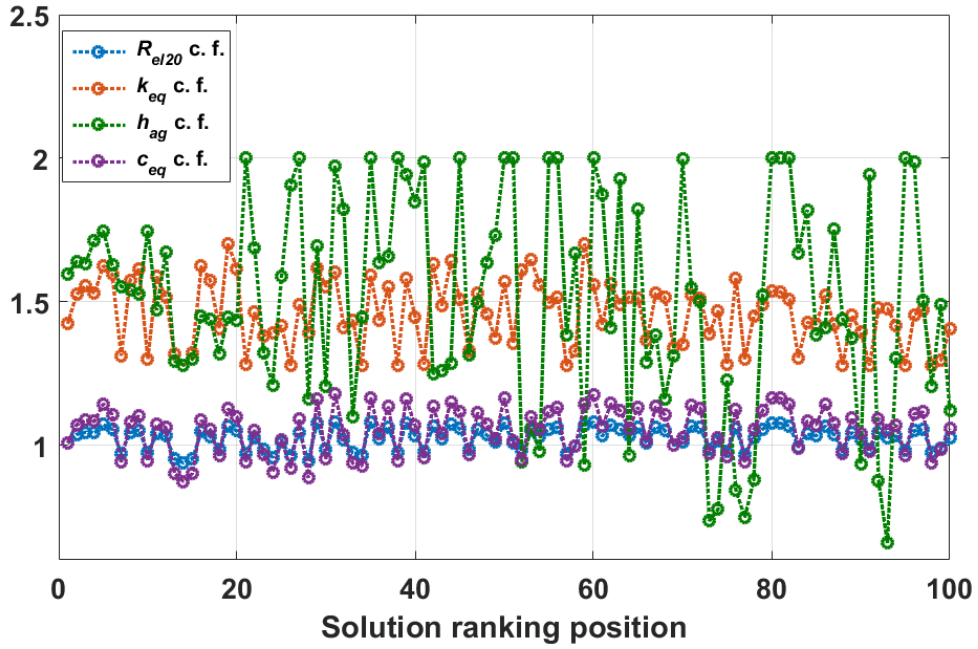


Figure 4.18: Best solutions found using the SQP algorithm for the corrective factors of R_{el20}, k_{eq}, h_{ag} *and* c_{eq}.

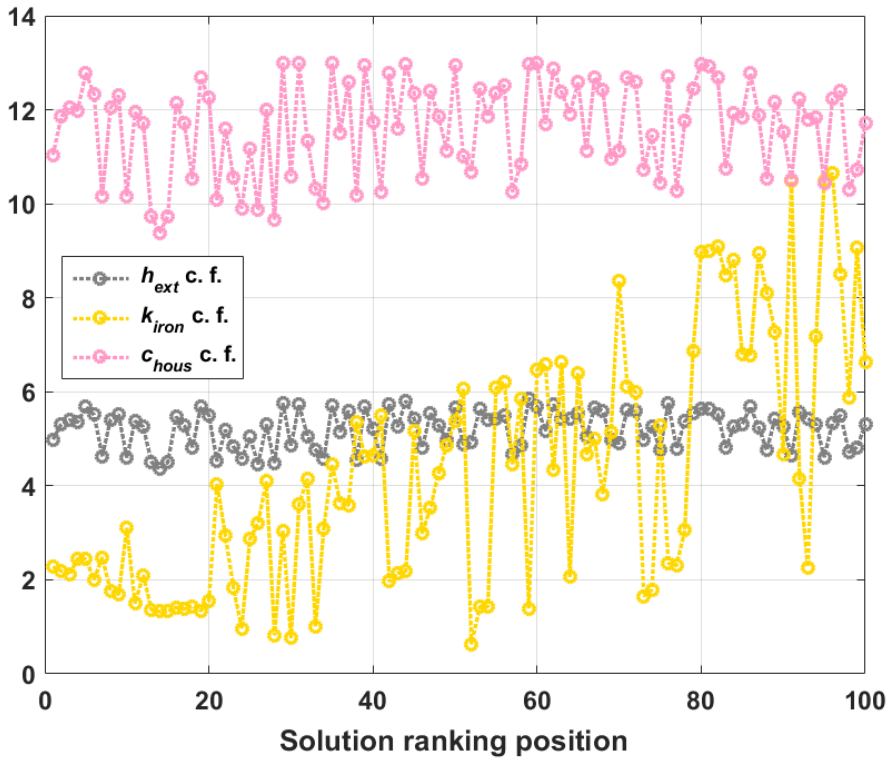


Figure 4.19: Best solutions found using the SQP algorithm for the corrective factors of h_{ext}, k_{iron} *and* c_{hous}.

From the optimal values of the corrective factors, it can be seen that the solution of the minimization problem is not unique. This can be explained by the fact that the only information provided is the winding temperature and some of the uncertain parameters are scarcely observable from it. On the other hand, this is not a main concern as this also means that those parameters are not relevant for the winding temperature prediction.

Analysing in detail the values determined by the SQP algorithm for each corrective factor, it can be seen that the value of the slot equivalent thermal mass c_{eq} and the electrical resistance R_{el20} were accurately calculated. In fact, their multiplicative corrective factors are close to 1. A corrective factor higher than 1 is instead identified for the parameters k_{eq}, c_{hous} and h_{ex} in order to improve the accuracy of the model. The corrective factors multiplying h_{ag} and k_{iron} are not uniquely determined, as it can be seen by the trend for the best 100 solutions obtained with the SQP algorithm. This means that these two parameters scarcely contribute in shaping the winding temperature profiles. An explanation of this is that h_{ag} is not relevant because most of the heat produced in the slot is dissipated through the housing, whereas the thermal resistances representing the heat opposition in the stator iron are small compared to the slot resistances and the external convection resistances.

Among the optimal corrective factors of these two parameters, the ones closest to one have been arbitrarily selected. The resulting optimized value for the critical parameters considered are reported in Table 4.4.

Parameter	Optimized value	Unit
h_{ext}	45.6	[W/ (m² °C)]
R_{el20}	5.05	Ω
k_{iron}	23.7	[W/ (m °C)]
k_{eq}	0.6	[W/ (m °C)]
c_{eq}	531	[J/ (kg °C)]
c_{hous}	1166	[J/ (kg °C)]
h_{ag}	10.5	[W/ (m² °C)]

Table 4.4: Optimized value for the critical parameters.

4.4.3 Performance of the tuned LPTN

The tuned values for the critical parameters shown in Table 4.4 have been employed in the LPTN. Figure 4.20 shows a comparison between the experimental winding temperature profiles used in the tuning procedure and the predicted winding temperatures obtained using the tuned LPTN. The maximum absolute prediction error is only 3 °C.

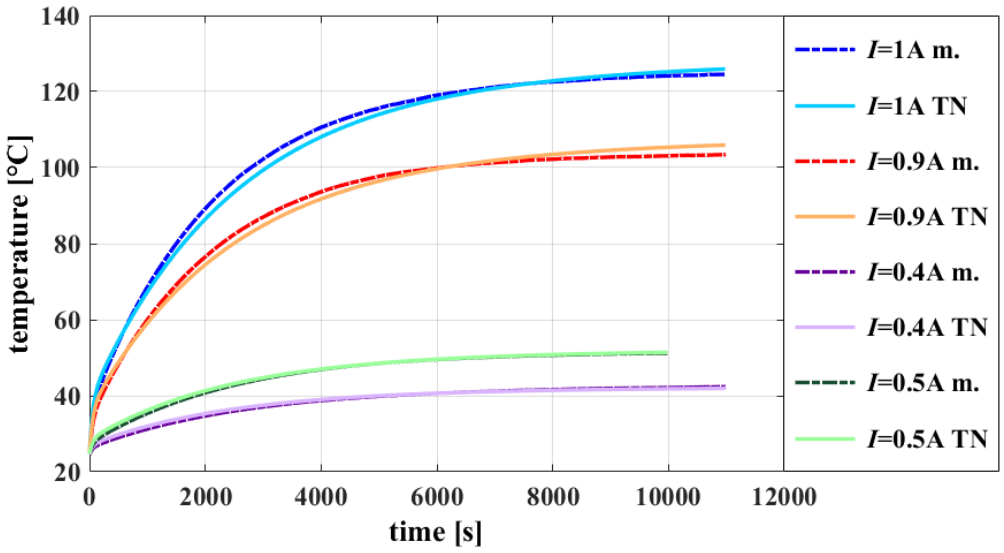


Figure 4.20: Measured winding temperatures (m.) compared to the temperatures predicted by the tuned LPTN for the case of DC current equal to 0.4, 0.5, 0.9 and 1A.

In order to confirm the "worthiness" of the tuned LPTN across the range of potential operational temperatures, then this was tested for a suite of temperature profiles purposely different from the ones used during the tuning procedure. The winding temperature has been recorded for the case of a current cycle shown in Figure 4.21, where three consecutive current steps were applied to each phase of the motor, equal to 0.9, 0.7 and 0A.

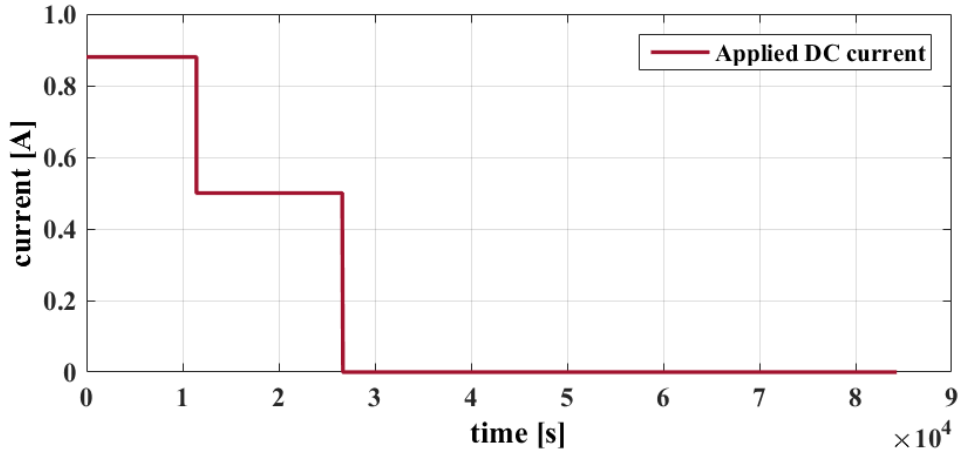


Figure 4.21: Test DC current applied for investigating thermal model's performance.

Figure 4.22 shows the results of this operating cycle and also compares the experimental results with the LPTN prediction for the same case. The maximum absolute temperature prediction error for this current load is equal to 5.2 °C, which clearly shows the excellent performance of the tuned LPTN.

Finally, in order to verify how the LPTN response for the case of currents out of the range of DC currents considered during the tuning procedure, its performance has been evaluated for a suite of DC currents which are 1.5, 2.2, 3.6 and 4.2A DC. The results are shown in Figure 4.23, where it can be observed that for the higher current values, the accuracy of the model decreases. Nevertheless, a good temperature prediction is still achieved, since an absolute temperature error of 6.1°C is obtained in the worst case. From a thermal modelling perspective, such a discrepancy is perfectly acceptable. In Table 4.5, the maximum temperature prediction error obtained for each current considered is reported.

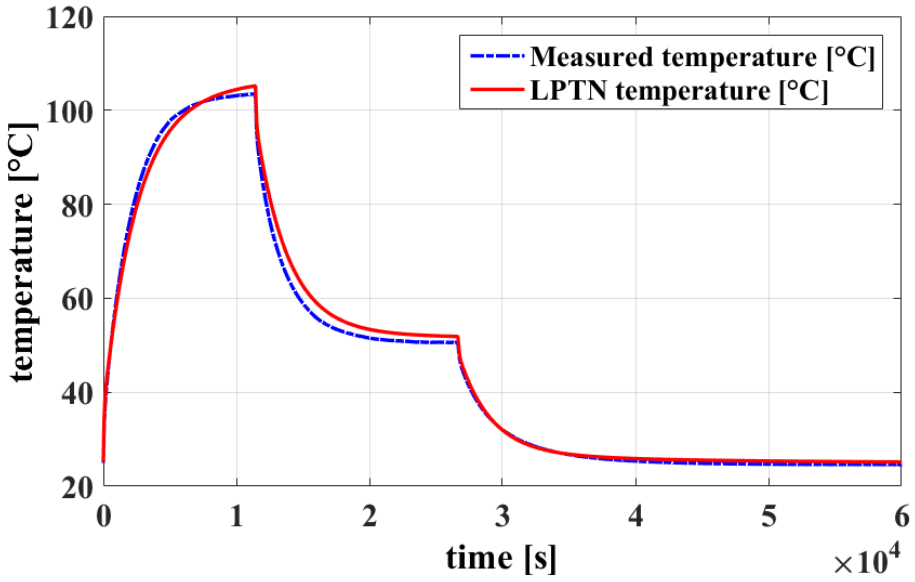


Figure 4.22: Measured and predicted using the LPTN winding temperature, when three consecutive steps of current equal to 0.9, 0.7 and 0A are applied to the phases of the SMPM motor.

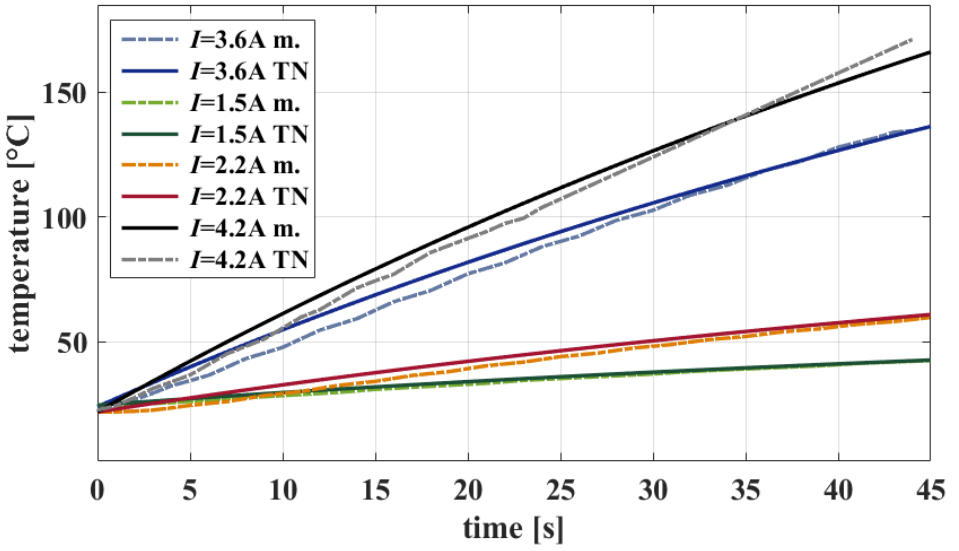


Figure 4.23: Comparison between the winding temperature experimental measurements and the LPTN predictions, for the case of DC current applied equal to 1.5,, 2.2, 3.6 and 4.2A.

DC current [A]	Maximum absolute temperature error [°C]
0.4	0.7
0.5	1.0
0.9	2.5
1..0	3.0
Cycle 0.9-0.5-0	5.2
1.5	1.2
2.2	3.7
3.6	6.4
4.2	7.4

Table 4.5: Maximum absolute temperature prediction error for each DC current considered.

4.5 Low Computational Cost Thermal Model

This section is devoted to a novel thermal modelling technique, based on an approximation/simplification of the LPTN presented above. The main feature of the proposed model is its sensibly lower computational cost, with respect to the original LPTN, with however no cost in terms of accuracy. The model can be a useful tool during the motor design stage, where the motor thermal behaviour is evaluated for each variation of the motor parameters and under different operating conditions. Also, the inherent velocity and accuracy of this technique could be ideal for its implementation on online temperature prediction platforms, such as are required for aircraft systems' health monitoring and prognostics.

As a first step for the derivation of the model, a state-space representation of the original LPTN is presented in Section 4.5.1 and an analytical solution for the

temperature distribution is derived. This allows to evidence the main drawbacks in terms of computational cost of the LPTN, which mainly derive from the fact that the system is time-variant as its state matrix is function of the electrical current in the windings.

In Section 4.5.2, the derivation of the novel low computational cost model is presented, which is based on a polynomial approximation of the dependency of the system on the phase current. The model is shown having similar performance as the original LPTN, but a lower computational cost, mainly because it does not require computation of inverse matrices or multiplications between matrices.

A further simplification of the model is obtained in Section 4.5.3, based on the observation that some of the system dynamics do not contribute significantly to the winding temperature profile. This suggests that a reduced order accurate LPTN can be obtained. The same polynomial approximation applied to the reduced order thermal network allows deriving an even faster thermal model.

4.5.1 LPTN Analytical Solution

In the previous paragraph, a LPTN was introduced for modelling the heat transfer in the SMPM motor under investigation. An analytical solution for that LPTN is derived. As shown in Figure 4.1, the proposed LPTN has some nodes at the same potential (the ones labelled with the same red number), due to the circuit symmetries. Thus, the LPTN can be represented by an equivalent 7-node LPTN as the one shown in Figure 4.24. The nodes in the circuit of Figure 4.24 are at the same potential of the ones of the original LPTN labelled with the same red number. The value of the resistances R_i and the capacitances C_i of the 7-node LPTN are reported in Table 4.6. They can be easily calculated from the

computation of the equivalent series and parallel resistances, as well as of the equivalent parallel capacitances of the original circuit.

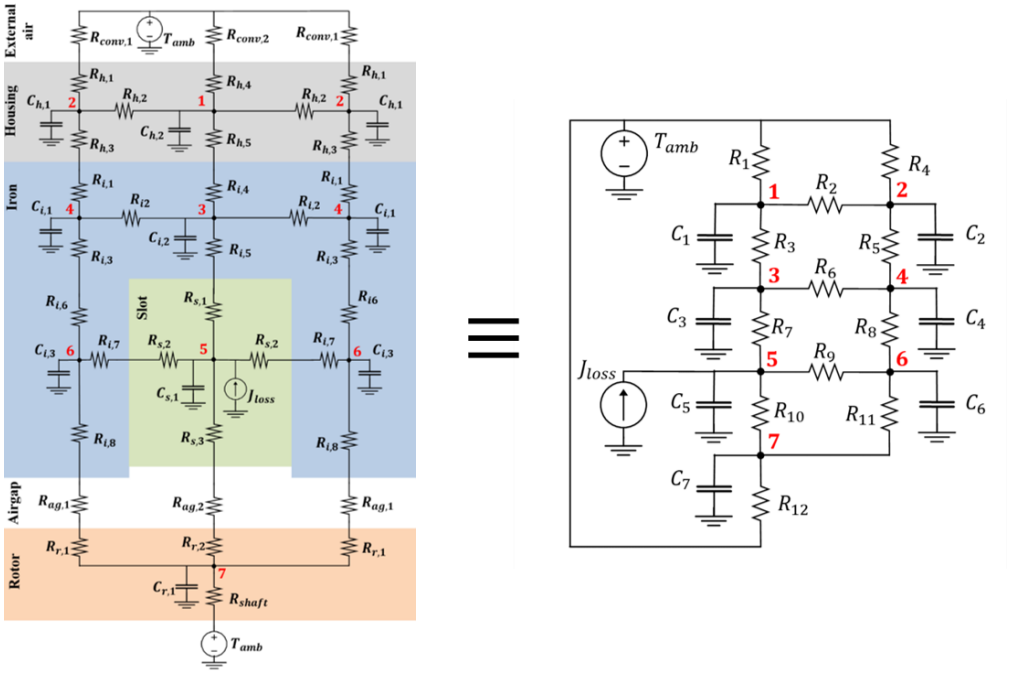


Figure 4.24: 7-node LPTN (on the right) equivalent to the thermal network depicted in Figure 4.1 (on the left).

R_1=23.64	R_7=10.34	C_1=86.79
R_2=0.07	R_8=1.12	C_2=26.42
R_3=0.09	R_9=4.47	C_3=8.37
R_4=77.67	R_{10}=240.29	C_4=2.55
R_5=0.29	R_{11}=747.93	C_5=16.74
R_6=0.48	R_{12}=160.79	C_6=5.49
		C_7=144.32

Table 4.6: Values of the resistances [°C/W] and capacitances [J/°C] of the 7-node thermal network.

Using the well-known node potential method for the resolution of circuits, the 7-node LPTN can be represented by system of first order differential equations, as described in (4.10), where *T* is the vector of the temperatures in the 7 nodes of the LPTN (i.e. vector of the unknowns), *u* is the input vector $[T_{amb}, I^2]^{\mathrm{T}}$ with T_{amb} ambient temperature and *I* electric current flowing in the windings.

$$\dot{T} = AT + Bu \tag{4.10}$$

$$A = C^{-1}A_1$$

$$B = C^{-1}B_1$$

The matrices A_1, B_1 and *C* are as shown in (4.11), where *C* is a diagonal matrix and A_1 is a symmetric matrix.

$$A_1 = \begin{bmatrix} a_{11} & R_2^{-1} & R_3^{-1} & 0 & 0 & 0 & 0 \\ R_2^{-1} & a_{22} & 0 & R_5^{-1} & 0 & 0 & 0 \\ R_3^{-1} & 0 & a_{33} & R_6^{-1} & R_7^{-1} & 0 & 0 \\ 0 & R_5^{-1} & R_6^{-1} & a_{44} & 0 & R_8^{-1} & 0 \\ 0 & 0 & R_7^{-1} & 0 & a_{55} & R_9^{-1} & R_{10}^{-1} \\ 0 & 0 & 0 & R_8^{-1} & R_9^{-1} & a_{66} & R_{11}^{-1} \\ 0 & 0 & 0 & 0 & R_{10}^{-1} & R_{11}^{-1} & a_{77} \end{bmatrix}$$

$$a_{11} = -(R_1^{-1} + R_2^{-1} + R_3^{-1})$$

$$a_{22} = -(R_2^{-1} + R_4^{-1} + R_5^{-1})$$

$$a_{33} = -(R_3^{-1} + R_6^{-1} + R_7^{-1})$$

$$a_{44} = -(R_5^{-1} + R_6^{-1} + R_8^{-1})$$

$$a_{55} = -(R_7^{-1} + R_9^{-1} + R_{10}^{-1}) + R_{el20} I^2 \alpha_0$$

$$a_{66} = -(R_8^{-1} + R_9^{-1} + R_{11}^{-1})$$

$$a_{77} = -(R_{10}^{-1} + R_{11}^{-1} + R_{12}^{-1})$$

$$B_1 = \begin{bmatrix} 0 & R_1^{-1} \\ 0 & R_4^{-1} \\ 0 & 0 \\ 0 & 0 \\ R_{el20}(1 - 20\alpha_0) & 0 \\ 0 & 0 \\ 0 & R_{12}^{-1} \end{bmatrix}$$

$$C = \mathbf{diag}(C_1, \dots, C_7) \tag{4.11}$$

Matrix A_1 is linearly dependent on I^2 through the element a_{55}, since the heat source related to the Joule losses J_{loss} is represented by (4.12), where R_{el20} and α_0 are physical constants and T_5 is the fifth element of vector *T*, which represents the temperature in the slot.

$$J_{loss} = R_{el20}\big(1 + \alpha_0(T_5 - 20)\big) I^2 \tag{4.12}$$

Thus, if the current is not constant, the matrix A_1 will be time-variant. Under the preliminary hypothesis of constant current *I*, the system is time-invariant, and the general solution of the system (4.10) at the generic time *t* is given by (4.13), where t_0 represents the initial time.

$$T(t) = e^{A(t-t_0)}T(t_0) + \int_{t_0}^{t} e^{A(t-\tau)}Bu\, d\tau \tag{4.13}$$

$$e^{A(t-t_0)} = \sum_{n=0}^{\infty} \frac{A^n(t-t_0)^n}{n!}$$

Assuming that *A* has 7 distinct eigenvalues (the original LPTN can be designed in order that this assumption is valid), then a linear transformation represented by the orthonormal matrix *M* exists, such that (4.14) is valid.

$$A = M^{-1}\Lambda M, \quad \Lambda = \mathbf{diag}(\lambda_1, \dots, \lambda_7) \tag{4.14}$$

λ_i is the i-th eigenvalue of the matrix *A*, whereas the columns of *M* are the eigenvectors of *A*. Thus, by introducing the change of variables $z = M^{-1}T$, the system (4.10) becomes $\dot{z} = \Lambda z + M^{-1}Bu$, whose solution is given by (4.15).

$$z(t) = e^{\Lambda(t-t_0)}z(t_0) + \int_{t_0}^{t} e^{\Lambda(t-\tau)}M^{-1}Bu\, d\tau \tag{4.15}$$

$$e^{\Lambda(t-t_0)} = \mathbf{diag}\left(e^{\lambda_1(t-t_0)}, \dots, e^{\lambda_7(t-t_0)}\right) = K(t)$$

It can be observed that the exponential matrix in (4.15) is a diagonal matrix. Therefore, assuming also constant ambient temperature T_{amb}, then the integral in (4.15) can be explicitly calculated and the solution of system (4.10) can be rewritten as in (4.16), where $S(t)$ is defined in (4.17).

$$T(t) = MK(t)M^{-1}T(t_0) + MS(t)M^{-1}Bu \tag{4.16}$$

$$S(t) = \mathbf{diag}\left(-\frac{1}{\lambda_1}\left(1 - e^{\lambda_1(t-t_0)}\right), \dots, -\frac{1}{\lambda_7}\left(1 - e^{\lambda_7(t-t_0)}\right)\right) \qquad (4.17)$$

Thus, in (4.16), the temperature profiles in the nodes of the LPTN for the case of constant current *I* are expressed as a linear combination of exponential functions of time *t*. If a discrete time domain is considered, the temperature prediction in case of time-varying current *I* and ambient temperature T_0 can be computed as follows. Defining t_j and t_{j+1} as two consecutive time instants, and assuming the current *I* and the ambient temperature T_0 as constant in the interval $[t_j, t_{j+1})$ and equal to their initial value at time t_j, then by considering (4.16) with $t_0 = t_j$ and $t = t_{j+1}$, the temperature can be iteratively predicted as shown in (4.18).

$$T(t_{j+1}) = M(I_j)K(I_j)M^{-1}(I_j)T(t_j) + M(I_j)S(I_j)M^{-1}(I_j)Bu(T_{0,j}, I_j) \qquad (4.18)$$

$$I_j = I(t_j)$$

$$T_{0,j} = T_0(t_j)$$

The assumption of ambient temperature and current constants between two consecutive instants is not critical as the approximation error can be arbitrarily reduced by reducing the sampling time and because the temperature dynamics are typically slow compared to the sampling time of a Digital Signal Processor (DSP).

It has to be noted that in (4.18) the matrixes *M*, *K* and *S* are functions of the current *I* through the eigenvalues and the eigenvectors of *A*. For this reason, when considering time varying currents, these matrices are to be updated at each instant for a correct calculation of the temperature. Therefore, the computational

effort for the temperature prediction could be unsatisfactory. In the next sections a solution for the reduction of the model computational cost will be proposed.

4.5.2 Low Computational Cost Thermal Model

The computational cost of the analytical solution presented in the previous section is relatively high as the eigenvalues and eigenvectors of *A* need to be calculated at each time instant as well as the inverse of the matrix *M*. In this section, a solution for the reduction of the computational cost of (4.18) is proposed and investigated. The main steps which lead to the simplified thermal model are the following:

- Calculation of the matrices elements in (4.18) for the current *I* in a specified domain;
- Computation of the 2nd order polynomial approximation of the relationship between the matrices elements and the current *I;*
- Exploitation of the coefficients of the computed polynomial functions for representing each matrix of (4.18) as 2nd order matrix polynomials of the variable *I;*
- Substitution in (4.18) of the approximating matrix polynomials for obtaining the simplified model.

As a first step, a maximum current I_{MAX} is fixed and the elements of the matrices *K*, *S*, *M* and M^{-1} are calculated for *I* between 0 and I_{MAX}. For the sake of clarity, Figure 4.25 shows only the variation of the last four diagonal elements $k_{i,i}, i = 4, \dots, 7$ of the matrix *K* in the range of current considered, normalized to their value at zero current, showing an almost parabolic behaviour. However, a similar

parabolic behaviour can be observed for each of the coefficients of matrix *K*, as well as for each element of matrices *S*, *M* and of its inverse M^{-1}.

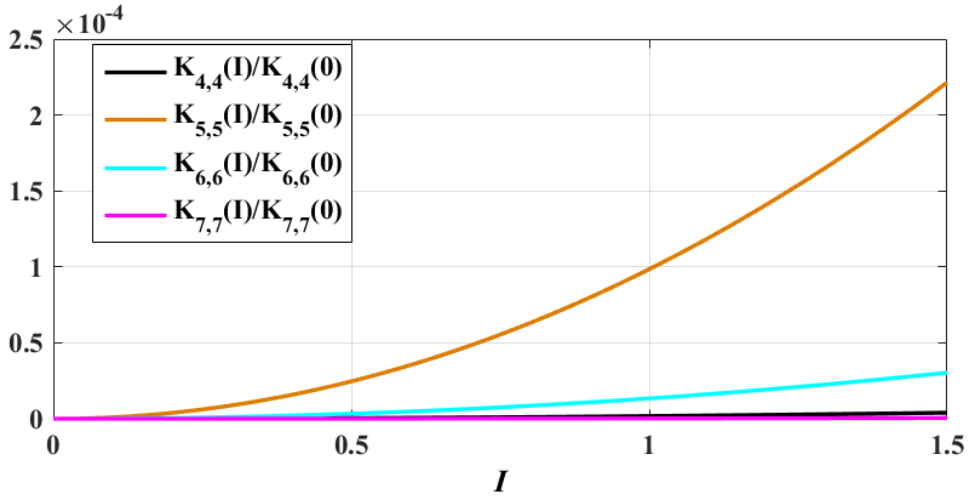


Figure 4.25: Last four elements of the diagonal of K respect to current I normalized by their value for I=0.

The relationship between each element of *K* and the current can be well approximated with a 2nd order polynomial as in (4.19). The coefficients $c_{Ki,i,n}$ of the approximating polynomial for the i-th element on the diagonal of *K* are calculated using the least squares method.

$$k_{i,i}(I) \cong c_{Ki,i,2}I^2 + c_{Ki,i,1}I + c_{Ki,i,0} \tag{4.19}$$

Similar results were then obtained for the relationship of each element of the matrices *S*, *M* and of its inverse M^{-1} respect to current *I*. The same approximating polynomials were therefore used as in (4.20), where $c_{Si,i,n}$, $c_{Mi,j,n}$, and $c_{-Mi,j,n}$ are the coefficient of the polynomial functions for the i-th diagonal element of *S* and the i-th row, j-th column of the matrixes *M* and M^{-1}, respectively.

$$s_{i,i}(I) \cong c_{Si,i,2}I^2 + c_{Si,i,1}I + c_{Si,i,0}$$

$$m_{i,j}(I) \cong c_{Mi,j,2}I^2 + c_{Mi,j,1}I + c_{Mi,j,0}$$

$$m_{i,j}^{-1}(I) \cong c_{-Mi,j,2}I^2 + c_{-Mi,j,1}I + c_{-Mi,j,0} \qquad (4.20)$$

From (4.19) and (4.20), the matrices K, S, M and M^{-1} can therefore be represented as in (4.21).

$$K \cong K_2I^2 + K_1I + K_0$$

$$S \cong S_2I^2 + S_1I + S_0$$

$$M \cong M_2I^2 + M_1I + M_0$$

$$M^{-1} \cong \bar{M}_2I^2 + \bar{M}_1I + \bar{M}_0 \qquad (4.21)$$

The elements of the constant matrices at the right side of (4.21) are the coefficients of the polynomials introduced in (4.19) and (4.20), as summarized in (4.22), where $k_{n_{i,i}}$, $s_{n_{i,i}}$, $m_{n_{i,j}}$ and $\bar{m}_{n_{i,j}}$ are the elements of K_n, S_n, M_n and $\bar{M}_n$, respectively.

$$k_{n_{i,i}} = c_{Ki,i,n}$$

$$s_{n_{i,i}} = c_{Si,i,n}$$

$$m_{n_{i,j}} = c_{Mi,j,n}$$

$$\bar{m}_{n_{i,j}} = c_{\bar{M}i,j,n} \quad , \quad n = 0,1,2 \qquad (4.22)$$

Finally, if the approximations presented in (4.21) are applied to the matrices of (4.18), the new Low Computational Cost (LCC) model for the temperature prediction is obtained as in (4.23), where W_i and V_i are constant matrices of

dimension 7x7 and 7x2, respectively, which are obtained from the multiplications between the approximating matrices on the right side of (4.21).

$$T(t_{j+1}) = \sum_{i=0}^{6} \left(W_i I_j^i T(t_j) + V_i I_j^i u(I_j) \right) \tag{4.23}$$

Since the matrices involved in (4.23) are constant matrices which can be calculated once at all, this model significantly decreases the computational cost of the temperature prediction, compared to the LPTN, as at each instant it is not required to compute any matrix inversion or products between matrices.

Although the proposed model considers only Joule losses as a heat source, it is important to note that it can be easily extended to applications where the stator iron losses are not negligible. Indeed, with the original LPTN these losses can be modelled as heat sources in the nodes of the stator teeth and the stator yoke [132]. Under the common assumption of temperature independent iron losses, they can then be represented as a function of the electrical frequency *f* and the current *I* [138]. It follows that the matrix *A* in (4.10) is unchanged if the heat sources representing the temperature independent iron losses are included in the original LPTN, and only the input vector u and the input matrix *B* would be modified. Thus, a procedure similar to the one presented can still be adopted for the new system, with the only difference that in (4.23) the input *u* will be function of *I* and *f*.

The LCC thermal model described by (4.23) for the fast winding temperature prediction is tested for the same DC currents as done for the original LPTN in Section 4.4.3. This also serves to compare the accuracy of the original LPTN to

that of the simplified analytical model. The mean relative and the maximum absolute errors of the predicted temperature using (4.23) and using the original LPTN, respect to the measured slot temperature, are reported for each DC current considered. It can be seen that the simplification of the LPTN does not affect sensibly the accuracy of the slot temperature prediction.

DC current	Mean relative error %		Max. Absolute error [°C]	
	LPTN	LCC	LPTN	LCC
1A	1.5	1.5	3	2.7
0.9A	1.7	1.6	2.5	3
0.5A	0.7	2.2	1	1.3
0.4A	0.9	2.3	0.7	1.3

Table 4.7: Mean relative and maximum absolute winding temperature prediction error with the LPTN and the LCC model, for different DC current loads.

The proposed model as described by (4.23) has similar accuracy as the original LPTN and lower computational cost (details of the comparison are given in Table 4.9) since it is characterized by reduced complexity. However, its complexity can be further reduced by decreasing the number of nodes of the original LPTN, which would reduce the dimension of the matrices in (4.23). Thus, in the next section a 3-node LPTN deriving from the original 7-node LPTN is evaluated, from which an even lower computational cost model will be obtained.

4.5.3 Lower order models

Equations (4.16) and (4.17) show that the motor temperatures can be represented as linear combination of exponential functions of time *t*. In particular, the exponents of the exponential functions are in the form $\lambda_i t$, with λ_i i-th eigenvalue of the matrix *A*. Since in the considered application the magnitudes of these eigenvalues are significantly different, in this section reduced dynamics models are evaluated in order to further reduce the computational cost of the winding temperature prediction.

Assuming that the eigenvalues λ_i of matrix *A* are ordered such that $\lambda_i < \lambda_j$ for $i < j$, the performance of the reduced dynamics model is investigated by incrementally setting to zero the diagonal elements of matrices *K* and *S* in (4.18). In this way, for instance by setting $k_{1,1}$ and $s_{1,1}$ equal to zero, the exponential functions relative to λ_1 can be neglected. By testing the reduced models against the experimental temperature profiles considered so far, it was found that, by neglecting the dynamics related to $\lambda_i, i = 1, \dots, 4$ the prediction of the stator temperature is similar to the output of the original LPTN. However, if the dynamics associated to λ_5 are also neglected, then the system accuracy is reduced with a maximum relative error of 22%. This can be observed in Figure 4.26, where for the same test sequence as that used for obtaining Figure 4.22, the stator temperature calculated with the 3rd order ($k_{i,i}$ and $s_{i,i}$ equal to zero for $i = 1, \dots, 4$) and the 2nd order (also $k_{5,5}$ and $s_{5,5}$ equal to zero) models are plotted along with the measured temperature.

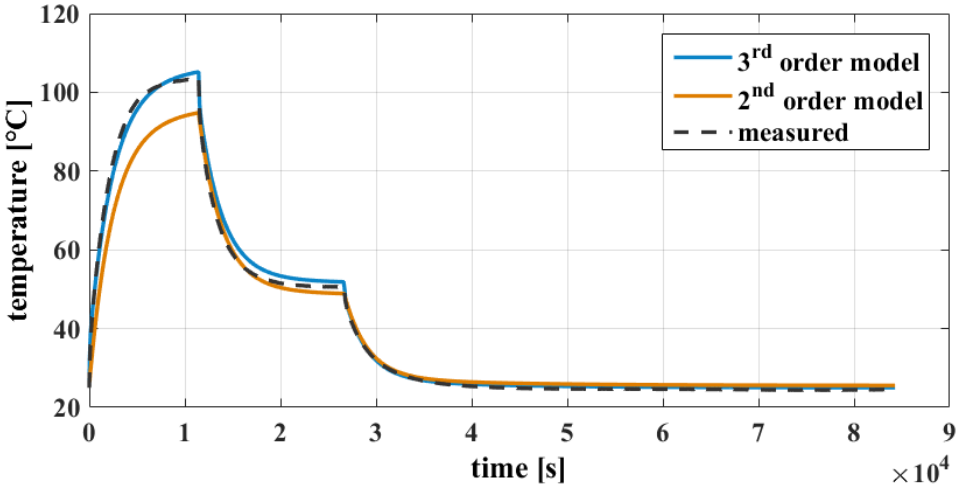


Figure 4.26: Measured winding temperature and predicted temperature using second and third order thermal models.

It is important to note that the benefits obtained in terms of computational cost by setting the appropriate elements of K and S to zero are limited as only the initial calculation time of the constant matrices of (4.23) is reduced, but there is no impact on the amount of operations to be computed online at each iteration. However, a perceived advantage is that high accuracy could be achieved also with a lower order LPTN.

According to these considerations, then the 7-node equivalent circuit of Figure 4.24 is reduced to a 3-node circuit by removing its less significant components for the winding temperature prediction. It can be noticed from Table 4.6 that the resistances R_2, R_3, R_5, R_6 and R_8, and the thermal masses C_3, C_4 and C_6 are the components with less significance to the overall circuit. In particular, these resistances can be approximated with a short circuit, whereas the capacitances can be discarded. Thus, the 7-node LPTN is reduced to the 3-node LPTN as

shown in Figure 4.27. The new resistances and thermal masses are defined by (4.24).

$$R_I = \frac{R_1 R_4}{R_1 + R_4} \qquad R_{II} = \frac{R_7 R_9}{R_7 + R_9}$$

$$R_{III} = \frac{R_{10} R_{11}}{R_{10} + R_{11}} \qquad R_{IV} = R_{12}$$

$$C_I = C_1 + C_2 \quad C_{II} = C_5 \quad C_{III} = C_7 \tag{4.24}$$

The same procedure described in Section 4.5.2 can thus be applied also to the 3-node LPTN. Thus, an analytical model similar to the one of (4.23) can be obtained also from the new 3-node LPTN, where now T is the vector of the temperatures in the 3 nodes of the LPTN, W_i and V_i are constant matrices of dimension 3x3 and 3x2, respectively, whereas current I_j and input vector u are unchanged. The second element of T represents the temperature in the stator slots. The computational cost of the new model will be lower compared to the one of (4.23) as the dimensions of the matrices involved are more than halved.

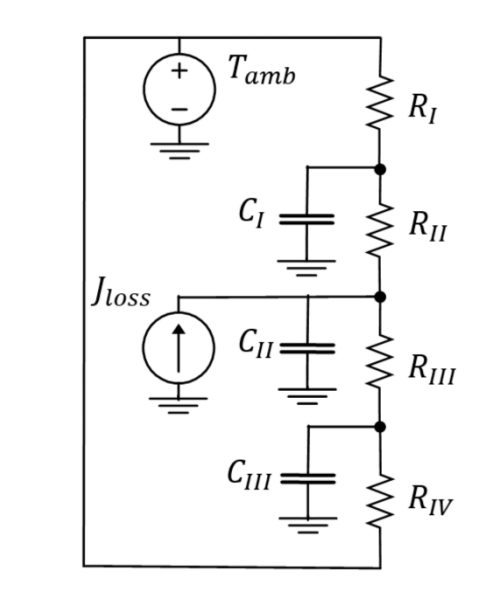


Figure 4.27: 3-node LPTN equivalent circuit.

The reduced computational cost analytical model derived from the 3-node LPTN shown in Figure 4.27 is tested for the same DC currents as done for the original LPTN in Section 4.4.3. Figure 4.28 shows the measured temperature and the predicted temperature for step currents of 0.4, 0.5, 0.9 and 1A DC. Figure 4.29 shows measured and predicted temperatures for the current cycle of Figure 4.22.

In Table 4.8, the mean relative and the maximum absolute errors between measured slot temperature and the predicted temperature using the reduced computational cost analytical model are reported for each current profile considered, along with the same error obtained with the original LPTN and with the 7-node LCC model. It can be noticed that in this case the errors remains below 3.3 °C.

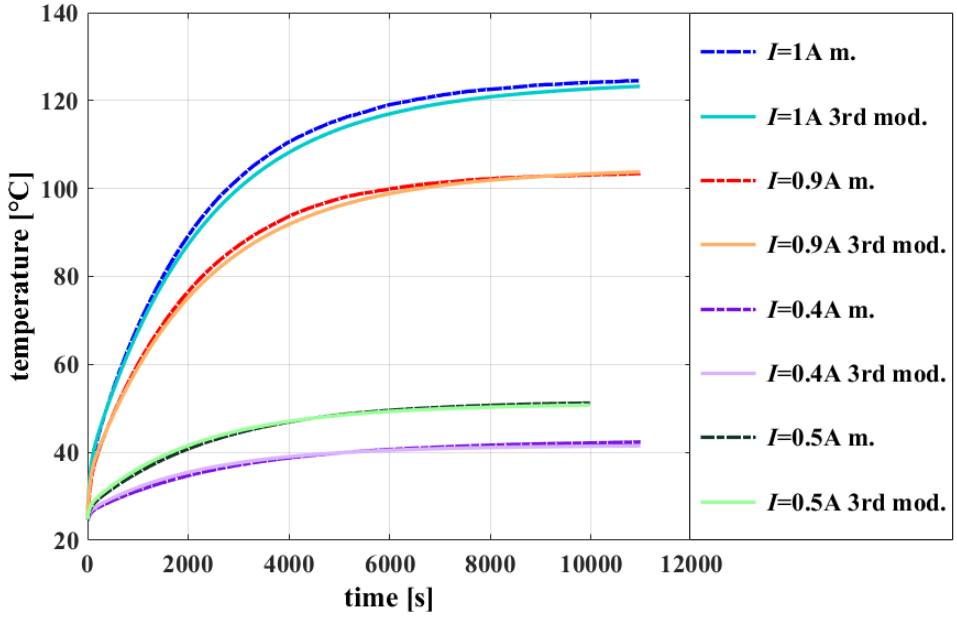


Figure 4.28: Measured winding temperatures (m.) compared to the temperatures predicted by the 3rd order analytical model for current I equal to 0.4, 0.5, 0.9 and 1A DC.

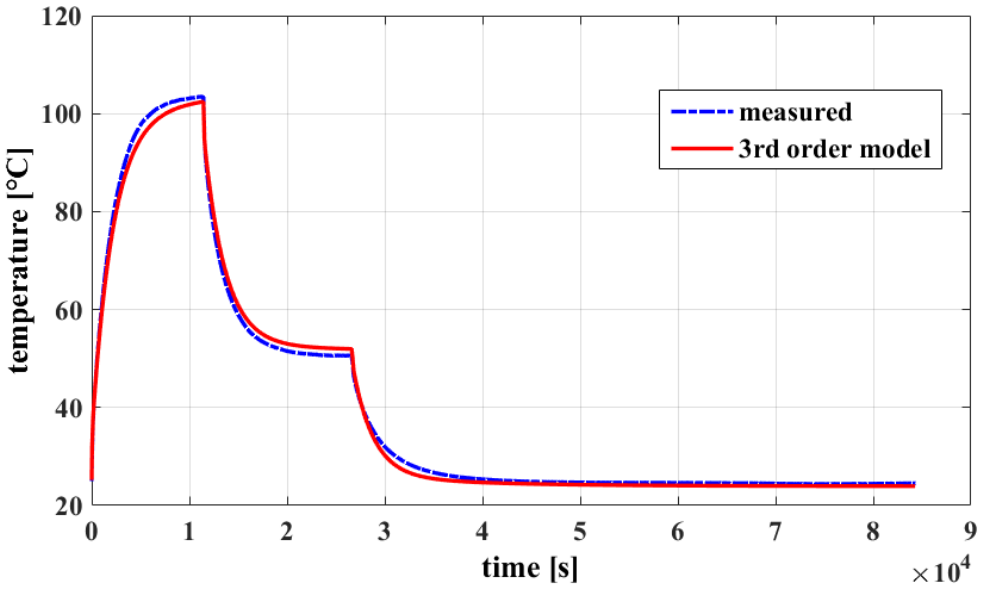


Figure 4.29: Measured winding temperature and temperature predicted with the 3rd order analytical model for three consecutive current steps of 0.9, 0.7 and 0A DC.

DC current	Mean relative error %			Max. Absolute error [°C]		
	LPTN	7th order LCC	3rd order LCC	LPTN	7th order LCC	3rd order LCC
1A	1.5	1.5	2.4	3	2.7	3.3
0.9A	1.7	1.6	1.4	2.5	3	2.2
0.5A	0.7	2.2	1.4	1	1.3	1.1
0.4A	0.9	2.3	1.4	0.7	1.3	1.1

Table 4.8: Comparison between mean relative and maximum absolute winding temperature prediction error of reduced dimensions analytical models and original LPTN for different DC currents applied.

Finally, a comparative study between the computational speeds of all the models presented in this chapter has been done. The models were implemented on MATLAB and run on a standard desktop PC, processor i3-4150 @3.50 GHz, 8GB RAM. The time required at each iteration for the calculation of the winding temperature was recorded using the MATLAB start stopwatcher timer. The results are illustrated in Table 4.9, and show that the simplification of the 7-node LPTN with the 3rd order LCC model allows for an almost 7 times faster computation.

Model	Computational time [10^{-6}s]
7-node LPTN	45
3-node LPTN	25
7th order LCC model	9
3rd order LCC model	7

Table 4.9: Computational time required for the temperature prediction at each iteration for the thermal models considered.

All the above highlights that the analytical solution presented does give significant advantages in terms of required computational resources without any negative impact on the overall model accuracy.

4.6 Conclusions

In this Chapter, the thermal analysis of SMPM machine designed has been illustrated. The analysis was required for evaluating the thermal behaviour of the motor during operations. In particular, the main focus was the prediction of the motor windings temperature, because of the concerns arising for the specific application.

As a first step, a LPTN has been introduced in Section 4.2. This thermal model was selected because of its potential low computational cost and high accuracy. The determination of its parameters has been explained, which was based on the physical properties of the motor materials implemented and on the motor geometry. The model was used during the design stage as a fundamental tool for

the prediction of the temperature distribution within the motor during operations, for different design solutions of the machine.

In Section 4.3, the results of an experimental thermal analysis of the motor are reported. In particular, some preliminary tests were conducted for confirming the assumptions regarding the heat transfer in the motor, which were made during the design stage. Moreover, with the aid of a thermal chamber, the motor operating conditions were reproduced, where an ambient temperature equal to the maximum ambient considered was set. The winding temperature has been measured for each operating condition, in order to verify that the threshold temperature set by the insulation temperature rating is not exceeded. Although during the emergency operations, when a three-phase star is shorted, the temperature slightly exceeds the maximum temperature allowed, it has to be considered that, during the real operating conditions, the current loads will be less severe.

From a comparison between measured and predicted with the LPTN winding temperatures, it could be noticed that the prediction error could be not acceptable. This is consequence of the inherent uncertainties of some parameters of the LPTN. For this reason, in Section 4.4, a tuning procedure of the LPTN critical parameters based on experimental temperature measurements, has been proposed in order to improve the accuracy of the thermal model. The procedure is based on a SQP algorithm, whose scope is to minimize a cost function representing the error between measured and predicted with the LPTN winding temperatures. The tuned LPTN has been tested for different current loads, showing an extremely good accuracy.

Finally, in Section 4.5, a novel thermal model has been presented. The model derives from a polynomial approximation of the LPTN parameters dependence to the electrical current. Its main feature is its sensibly reduced computational cost respect to the original LPTN, but with a similar degree of accuracy in the temperature prediction. The procedure for the derivation of the model has been thoroughly explained. The performance of the model has been evaluated against experimental results and also compared to the temperature predictions obtained using the original LPTN. The low computational cost of the model, makes it a valid alternative to the LPTN for the evaluation of the winding temperature. Moreover, another perceived advantage of this technique, is its applicability to online monitoring of performance.

Chapter 5
Lifetime consumption of windings electrical insulation

The high current density in the slots produces high temperatures and high temperature variations, which can cause significant temperature related stresses on the winding electrical insulation. Since the winding failures are one of most common cause of failures of the motor [90], it is crucial to guarantee that the lifetime of the winding electrical insulation is long enough to respect the reliability requirements of the application. For this reason, it is common practice to design the motor with severe over-engineering in such a way that the maximum temperature reached in the stator slots is below the thermal class temperature of its electrical insulating materials [139], [5]. In fact, the lifetime of a material when it is kept at its thermal class temperature is equal to 20,000h [140]. However, for short-time duty applications, the maximum temperature is reached only for few instants. Thus, the lifetime of the insulating material related to the thermal stress is expected to be longer than 20,000h. If the traditional

design rules (for steady state operations) are kept, then a potential oversizing of the machine for the specific application is unavoidable.

On the other hand, rapid temperature variations, can cause thermo-mechanical stress on the winding electrical insulation [141]. The combined action of thermal and thermo-mechanical stresses could reduce the total lifetime of the insulating material. However, the effect of thermo-mechanical stress on random wound windings for medium voltage motors has not been completely assessed in the present literature.

Following the difficulties in assessing the lifetime of the winding electrical insulation under the typical stresses of this specific application, along with the need of maximizing the motor performance, an investigation on the relationship between winding temperature profile and lifetime consumption of its insulation has been conducted in this work.

In Section 5.1, a literature review focusing on studies conducted for assessing the ageing of the winding electrical insulation for medium voltage applications under multiple stresses is reported. From this review, it has not been found a model designed for predicting the ageing of random wound windings for the type of application under investigation. This because the implementation of high performance machines for short time duty applications is relatively novel and the analysis of ageing is time consuming, since it is typically based on the results of specific accelerated ageing tests.

Following the absence of a winding insulation lifetime consumption model for short time duty applications (such as EMA under investigation), on the base of

the ageing models present in the literature, a novel lifetime consumption model is then proposed for the winding electrical insulation under investigation. The model attempts to relate the ageing due to thermal and thermo-mechanical stresses to the temperature profile in the stator slot.

Since the proposed model is based on the result of specific accelerated ageing tests, in Section 5.2 the main standards which provide recommendation on how to perform any accelerated ageing tests are reviewed. On the base of the guidelines provided by these standards, a series of accelerated ageing tests has been performed with the aim of collecting significant results for tuning the parameters of the proposed lifetime prediction model. The experimental setup is described in detail and the results obtained are reported, as well as the model's tuning procedure based on the data collected.

Finally, in Section 5.3, an investigation on the applications of the proposed model is presented. In particular, the model is shown to be a useful tool for the punctual maintenance scheduling of the SMPM motor windings under investigation, through an online estimation of the winding insulation degradation rate.

5.1 Winding electrical insulation lifetime prediction model

In this section, an innovative lifetime consumption model of the electrical insulation for random wound windings, such as the ones employed in the SMPM motor is proposed. The model provides a relationship between the temperature profile in the slot and the time to failure of the insulating material. It takes into

account the effects of thermal and thermo-mechanical stresses, which are the main ageing factors when the winding insulation system undergoes heavy thermal cycles.

5.1.1 Literature review on ageing models

It is not trivial to quantitatively determine how severely different stresses can age the insulating materials. In fact, the physics of the ageing processes is complex due to the presence of a multitude of co-acting stresses on the insulation. Several unpredictable factors such as the amount of voids in the insulations, tolerances, and the nonhomogeneous application of stresses on the insulating materials contribute to the complexity of the problem and make it very difficult to determine a precise relationship between magnitude of the stresses applied and the consequent lifetime of the winding [142].

5.1.1.1 Single stress models

In order to understand the relationship between stress and ageing, a common practice is to investigate the effect of each single ageing factor separately. Although models are proposed which attempt to predict the insulation lifetime through a description of the physics of ageing [143], empirical approaches based on the results of specific ageing experiments are often preferred [144]. The action of multiple stresses is then approximated as combination of the lifetime models derived for each single ageing factor [145]. However, in order to reduce the complexity of the model, usually only the main ageing factors, which are different depending on the specific application, are taken into account.

Since thermal ageing is associated to a chemical reaction triggered by high temperatures, the lifetime of the insulation is typically modelled by the

Arrhenius's first order chemical reaction rate equation [101], [146], as given in (5.1), where $\mathcal{L}_T$ is the insulation lifetime under thermal stress at temperature T, $\mathcal{L}_0$ represents the lifetime at a reference temperature T_0, whereas the parameter Q is related to the activation energy of the degradation process.

$$\mathcal{L}_T(T) = \mathcal{L}_0 e^{\frac{Q}{T}-\frac{Q}{T_0}} \tag{5.1}$$

Lifetime of the insulation due to electrical stress is generally represented by an empirical inverse power law model [147], [148], as the one shown in (5.2), where V represent the applied voltage, $\mathcal{L}_V$ is the insulation lifetime under electrical stress at voltage V, whereas k_v and N_v are constants which can be determined from the results of specific accelerated ageing tests on the windings under investigation.

$$\mathcal{L}_V(V) = k_v V^{-N_v} \tag{5.2}$$

Ageing due to mechanical stress can be modelled with an inverse power law model in a similar way as for the electrical stress [149]. The main feature of the inverse power law model is that the relationship between stress applied and lifetime is linear on a log-log plot is linear. The free parameters k_v and N_v of (5.2) define the slope and the y-intercept of the straight line on the log-log plot.

The ageing caused by thermo-mechanical stress, whose nature is mechanical, is more difficult to be modelled as it is not possible to isolate experimentally its effect from the ageing due to thermal stress. In [102], an inverse power law model is proposed for the case of thermal cycling, where the life consumption is related to the maximum wire elongation during cycling. However, the determination of these maximum elongation of the winding is not trivial since it

depends on the temperature distribution in the stator slot, as well as on the materials which compose the windings [150].

Environmental stresses usually do not age directly the insulating material, but rather their effect can worsen the action of other ageing factors. For instance, moisture can facilitate partial discharge activity and thus accelerate the ageing due to electrical stress [151]. For this reason, there are not specific ageing models related to environmental stress. However, the effect of the environmental stress can be represented by properly modifying the value of the parameters of lifetime models related to other ageing factors.

Single stress life models are usually tuned on the base of the results of specific accelerated ageing tests, where specimens of the winding under investigation are aged applying a specific stress level and information is obtained from a statistical analysis of the time to failure of the single specimens, as it will be explained in detail in Section 5.2. They can achieve good accuracy in the prediction of the time to failure of the winding insulation under that specific stress. However, the applicability of these models is limited, since during operations the winding insulating materials typically experience the coaction of multiple stresses of different nature, and any single stress life model can provide accurate lifetime predictions for this case.

5.1.1.2 Multi-stress models

A possible approach for defining a multi-stress life model is to find a proper combination of the single stress life models which better represent the simultaneous action of different stresses. From experimental observations, different stresses applied at the same time usually cause an ageing rate sensibly

bigger than the sum of the ageing rates related to the single stresses applied, and slightly smaller than the multiplication of the single ageing rates [152], [153]. This means that it cannot be assumed superimposition of the single stresses. In [152] is then proposed a general formulation for lifetime models under multiple stresses, as in (5.3), where $\mathcal{L}$ is the lifetime under multiple stresses, $\mathcal{L}_i$ represents the lifetime related to the single stress model for the stress S_i, $\mathcal{L}_0$ is the lifetime expected at a temperature T_0 when any other stress is applied, and G is a correction function which accounts for the fact that the simple multiplication of the single ageing rates yields a too high overall ageing rate.

$$\frac{\mathcal{L}(S_1, \dots, S_n)}{\mathcal{L}_0} = \frac{\mathcal{L}_1(S_1)}{\mathcal{L}_0} \dots \frac{\mathcal{L}_n(S_n)}{\mathcal{L}_0} G(S_1, \dots, S_n) \tag{5.3}$$

In the next section, a lifetime prediction model is proposed which makes use of (5.3) for the determination of the ageing rate of the winding insulation of the SMPM motor under the stresses typical of the considered application.

5.1.2 Multi-stress Lifetime Consumption model for the winding electrical insulation of the SMPM motor

In this section, a model is proposed, which predicts the ageing rate of the winding electrical insulation under the main stresses applied for the application under investigation. In order to reduce the model to a reasonable complexity, the main ageing factors are firstly identified.

5.1.2.1 Considered stresses

As reported in Chapter 4, high current density in the slot causes high operating temperatures. It implies that thermal stress is expected to be the main ageing factor. Moreover, since a short-time duty application is being investigated, steep

temperature variations are expected in the slot, which indicates that thermo-mechanical stresses will also have a significant impact.

Other stresses are not considered in the proposed model since their effect should be far smaller than the ageing due to temperature related stresses. For example, environmental stress is not included in the model, as the slots are filled with a protective epoxy resin which should limit infiltration of moisture and other agents. The effect of electrical stress is supposed to be negligible, since windings with grade II enamelled coating were employed for the designed motor, which are characterized by partial discharge inception voltage higher than the maximum voltage applied, which is in the worst case equal to two times the power supply DC-Link voltage.

5.1.2.2 Thermo-mechanical stress

Several studies on the effects of thermo-mechanical stress on the life of electrical insulation are present in the literature, mainly focused on large hydroelectric generators and wind turbines ([102], [154]). This is due to the fact that the load applied to these generators is generally discontinuous, and significant temperature transients are experienced in the stator slots which cause significant dilation of the windings. Several years of investigations on these types of applications means that large hydroelectric generators failures databases are available today. Such data confirms that thermo-mechanical stress is one of the main causes of early failure of the electrical insulation of such machines [155].

On the contrary, thermo-mechanical stress for the winding electrical insulation of low voltage electrical machines has gained interest only recently, with the significant increase of performance of electric motors in the aerospace and

automotive fields [156]. In fact, traction motors operates under variable load and electric motors of electromechanical actuators for aerospace applications are often designed for intermittent and short time duty operations [100]. The effects of high temperature transients experienced by the windings for these applications must be investigated in order to assess the motor reliability. In [156], a FE model is implemented in order to determine the mechanical stress developed in random wound windings under thermo-mechanical stress. In [157], it is shown that a time varying temperature can shorten the life of small motor winding insulation. Thus, the main aim of this section is to propose and validate a novel lifetime model [158], which predicts the life of the electrical insulation for the case of random wound windings subject to variable temperature, is proposed.

Since all the stresses considered in the model are temperature related, the hot spot temperature in the slot $T(t)$, as function of time *t*, is the only input of the model. The structure of the model is based on (5.3), where it is assumed that the ageing rate due to different stresses is equal to the product of the single ageing rates multiplied by an appropriate corrective function. Thus, the first step is related to the definition of the single stress ageing models related to thermal and thermo-mechanical stresses.

Lifetime $\mathcal{L}_T$ related to the thermal stress when the temperature is equal to a constant temperature *T*, can be represented by (5.1). Its parameters can be conducted on the base of accelerated thermal ageing tests, as described by specific standards (e.g. [123], [140]). These are shown in Section 5.2.

The above is done considering an insulation system that comprises enamelled wire insulating coating. Thus, the thermo-mechanical stress is mainly concerned

with the mechanical interactions between conductor and coating. Adhesive contact can be assumed between the two materials [156]. Their thermal expansion causes a mechanical shear stress on the contact surface. This stress is related to the different thermal expansion rate of different materials. This difference is proportional both to the difference between the thermal expansion coefficients of the conductor and insulating coating, as well as to the temperature difference between the two materials [102]. Although the expansion coefficients difference is a constant typical of the materials employed, the temperature distribution will be more non-homogeneous when fast temperature transients are applied. It is then assumed that the thermo-mechanical stress is related to the first time derivative of the temperature $v = \frac{dT(t)}{dt}$.

Empirical inverse power law models show good shaping of the relationship between ageing and mechanical fatigue [159]. For this reason, the model in (5.4) has been designed for modelling the normalized lifetime $\mathcal{L}_M$ related to thermo-mechanical stress when a constant temperature variation *v* is applied. In (5.4), *k* and *N* are the free parameters of the model, which can be determined on the base of accelerated thermo-mechanical ageing tests, as it will be shown in Section 5.2.

$$\mathcal{L}_M(v) = (1 + k|v|)^{-N} \tag{5.4}$$

The lifetime due to thermo-mechanical stress is normalized between 0 and 1, in order to integrate it together with the thermal ageing model, as thermal and thermo-mechanical stresses jointly age the winding's insulation system. In particular, for the case of absence of thermo-mechanical stress, which is when

the temperature is constant (v=0), the lifetime of the winding insulation is function of temperature T through (5.1). Thus, Equation (5.4) can be used as a multiplicative factor to the thermal ageing model of (5.1), representing the effect of thermo-mechanical stress in the lifetime prediction. In particular, when the temperature is constant, then $\mathcal{L}_M = 1$ and no thermo-mechanical stress effect is included. Finally, it has to be noted that in (5.4) the absolute value of v is considered in order to include both the stress due to thermal expansion and contraction of the materials involved.

5.1.2.3 Combined stresses

Since the ageing rate due to multiple stresses can be represented as the product of the single stress ageing rates multiplied by a corrective factor, as in (5.3), then the lifetime $\mathcal{L}$ due to constant thermal and thermo-mechanical stresses can be represented as in (5.5), where G is the corrective function to be defined.

$$\mathcal{L}(T, v) = \mathcal{L}_T(T)\mathcal{L}_M(v)G(T, v) \tag{5.5}$$

For compatibility reasons $\mathcal{L}$ must be equal to $\mathcal{L}_0$ when the constant temperature is equal to T_0 by definition, and $\mathcal{L}$ has to be equal to $\mathcal{L}_T$ when the temperature is constant. Therefore, G has to be equal to 1 in both cases. Thus, G has been defined as given in (5.6), which is the simplest function that respects the compatibility conditions, as shown in [160], where a similar model for electro-thermal ageing model is presented. The similarity between the model of (5.5) and the one of [160] is that they both consider the deterioration due to thermal ageing and a second ageing factor whose deterioration rate can be modelled by an inverse power law. However, such second ageing factor is thermo-mechanical stress for (5.5) whereas is electrical stress for the model presented in [160].

$$G(T, v) = (1 + k|v|)^{N\left(\frac{Q}{T} - \frac{Q}{T_0}\right)} \tag{5.6}$$

Equation (5.5) represents the lifetime of the winding insulation under constant stresses. However, the only case in which the two stresses considered are constant is when both temperature and temperature time derivative are constant, which happens only for *v* equal to zero. Therefore, in order to propose a model which relates the winding lifetime to its temperature profile, it is necessary to find a local form of the model which estimates the instantaneous life consumption at time *t*, given the temperature profile $T(t)$ and its time derivative $v(t)$.

In order to achieve this, a function $f(t)$ is defined, which represents the insulation life remaining at time *t* if its temperature is kept constant equal to T_0. The function must be $f(t_0) = \mathcal{L}_0$ at initial time t_0 where there has not been any ageing, and $f(t_f) = 0$ at the time to failure t_f, when the whole insulation lifetime has been consumed. The function $f(t)$ will then decrease with respect to time according to (5.7), in order to be consistent with the lifetime model. It can be noticed that the derivative of f is always negative since the life of the insulation can only decrease.

$$\frac{df(t)}{dt} = -\frac{\mathcal{L}_0}{\mathcal{L}(T(t), v(t))} \tag{5.7}$$

Integrating over time from t_0 to t_f both sides of (5.7), it is then possible to obtain a relationship between lifetime t_f of the winding insulation and the temperature profile $T(t)$, which is described by (5.8).

$$\int_{t_0}^{t_f} \frac{1}{\mathcal{L}\big(T(t), v(t)\big)}\, dt = 1 \tag{5.8}$$

It is important to remark that (5.8) is true under the assumption that the deterioration of the insulation due to the stresses applied is time-independent and additive [160]. Under the same assumption, starting from (5.7), it is possible to determine an expression for the function *f* at a generic time *t* between t_0 and t_f. In fact, by integrating both sides of (5.7) between t_0 and *t*, then (5.9) is obtained.

$$f(t) = \mathcal{L}_0 - \int_{t_0}^{t} \frac{\mathcal{L}_0}{\mathcal{L}\big(T(t), v(t)\big)}\, dt \tag{5.9}$$

Equation (5.9) provides a measure of the insulation lifetime remaining at time *t*. Its form makes it suitable for implementation as online life consumption model. In fact, from (5.9), it can be obtained an iterative formula as shown in (5.10), where the function *f* at a generic time instant t_2 is represented as the value of *f* at a previous time instant t_1 minus the "amount of life consumed" during the time period $[t_1, t_2]$ which is represented by the integral on the right hand side of (5.10).

$$f(t_2) = f(t_1) - \int_{t_1}^{t_2} \frac{\mathcal{L}_0}{\mathcal{L}\big(T(t), v(t)\big)}\, dt \tag{5.10}$$

Finally, since often for short-time duty application the load is invariant over the cycles, it can be stated that for each working cycle the same amount of insulation life is consumed. Thus, the number of cycles *C* which the winding insulation will be able to withstand can be calculated as the total lifetime $\mathcal{L}_0$ divided by the

amount of life consumed over a cycle, as shown in (5.11), where t_1 and t_2 represent initial and final time of a generic duty cycle.

$$C = \frac{\mathcal{L}_0}{\int_{t_1}^{t_2} \frac{\mathcal{L}_0}{\mathcal{L}\big(T(t), v(t)\big)} dt} \tag{5.11}$$

5.1.3 Evaluation of the lifetime consumption model

In this Section, a detailed analysis of the model is conducted, with the objective of understanding how the key parameters of the model *k* and *N* affect the lifetime predictions. In order to do that, the case of a constant duty cycle has been considered, with a generic winding temperature profile for each cycle, such as the one illustrated in Figure 5.1, which considers a constant load during the first half of the duty cycle period and no load during its second half. For simplification, the temperature profile is modelled using the equation of charge and discharge of a capacitor in an RC circuit, which is analogous to consider a one node LPTN. In Figure 5.1, T_1 and T_2 are the generic minimum and maximum winding temperature, respectively, whereas t_1 and t_2 are the initial and final time of a generic cycle.

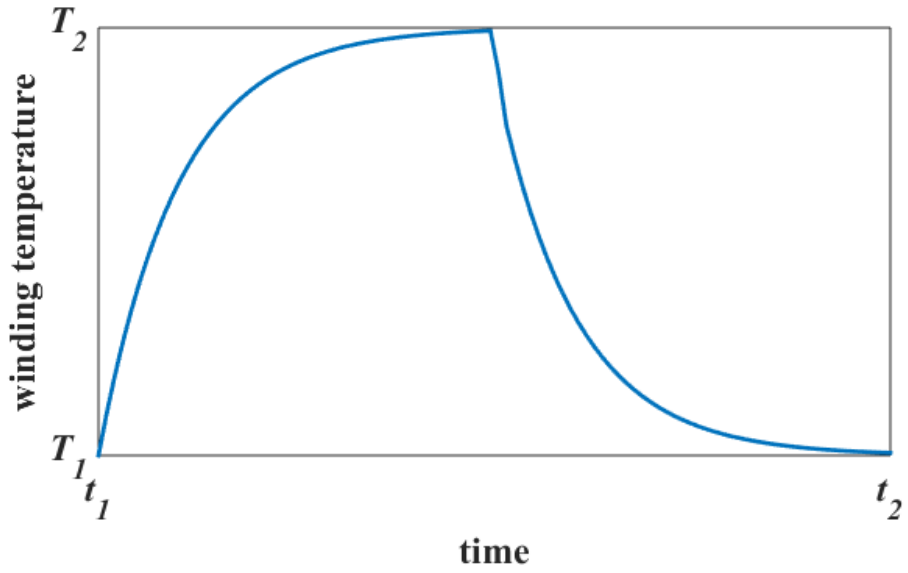


Figure 5.1: Generic winding temperature profile during one duty cycle.

In other words a sensitivity analysis on the model parameters *k* and *N* has been performed for evaluating their influence on the lifetime prediction of (5.11).

As a first step, the influence of the value of *k* on the lifetime prediction has been considered. In particular, the model represented by (5.11) has been used for calculating the lifetime for different values of *k*, and for a winding temperature cycle as the one of Figure 5.1. The value of *N* has been arbitrarily fixed equal to 1, and the computation has been repeated for different duty cycle period lengths, while keeping fixed minimum and maximum temperatures of the temperature profile. Based on the typical insulation limits for the case at hand, these temperature limits were selected to be 150 and 230°C, respectively. The temperature range $[T_1,T_2]$ is kept constant in order to obtain a proportional relationship between duty cycle period $t_2 - t_1$ and the temperature variation

respect to time. Figure 5.2 shows the computed lifetime for different values of k, and for different duty cycle periods $t_2 - t_1$.

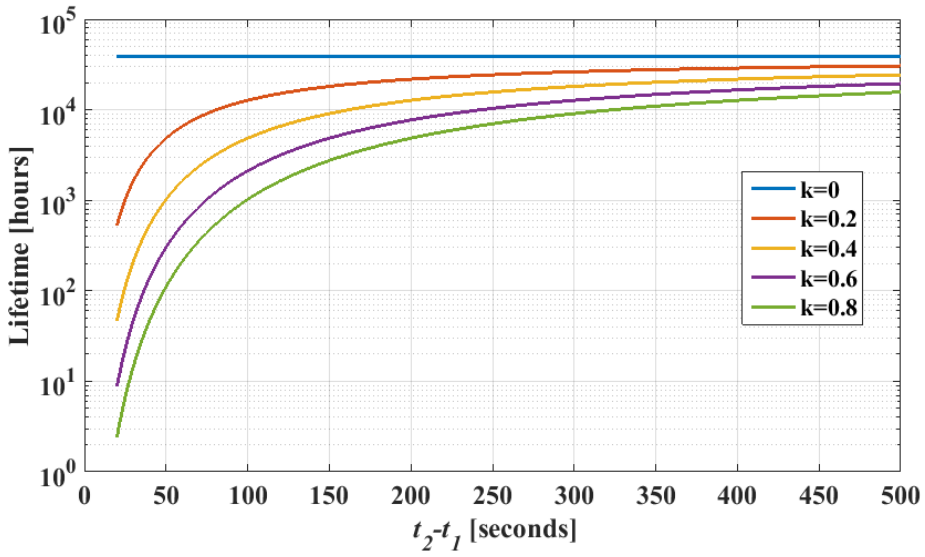


Figure 5.2: Lifetime vs. duty cycle period, for different values of k, when N is equal to 1 and the temperature cycle temperature range is fixed.

As expected, for the case of *k* equal to 1, the lifetime prediction is nearly constant for different duty cycle period lengths. In fact, for that value of *k*, the effect of thermo-mechanical ageing is not taken into account by the model, and the lifetime is determined only by considering the insulation degradation due to thermal ageing. Since the temperature range is kept constant over the cycle, whereas only the frequency of cycles is changed, the lifetime due to only thermal ageing will be nearly constant. For higher values of *k*, the degradation due to thermo-mechanical stress will be more significant and the lifetime will shorten consequently. In particular, when thermo-mechanical ageing is included, the insulation degradation is faster for a shorter duty cycle period as the temperature variations respect to time during the cycle will be higher.

The same analysis has been conducted by varying the value of *N* while keeping the parameter *k* equal to 1. The results of the analysis are illustrated in Figure 5.3, where a similar behaviour as above is easily observed.

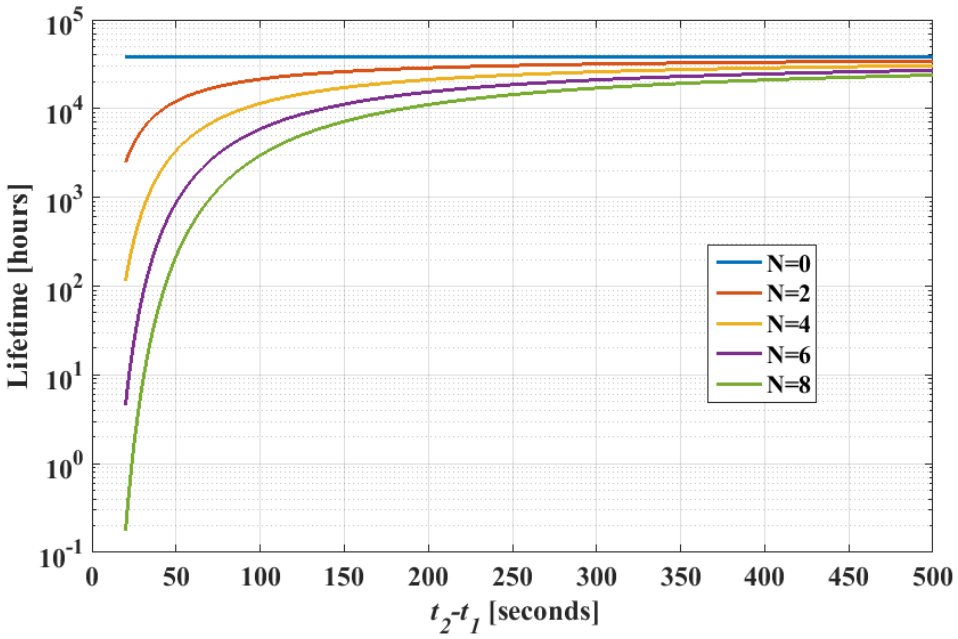


Figure 5.3: Lifetime vs. duty cycle period, for different values of N,, when k is equal to 1 and the temperature cycle temperature range is fixed.

This analysis highlights the importance of defining correctly the shaping parameters of the model. In fact, a small variation of a parameter can lead to a significant insulation lifetime insulation error. In the next section a procedure, based on experimental testing, for the determination of the model parameters is proposed.

5.2 Accelerated ageing tests for the tuning of the lifetime consumption model parameters

The tuning procedure for the free parameters of the model presented in the last section is based on the experimental results of accelerated ageing tests, which were conducted in order to assess how significantly the stresses applied deteriorate the winding insulation materials under study.

Accelerated ageing tests are commonly used in order to find out a relationship between stresses and ageing of a component. During an accelerated ageing test, stresses of higher magnitude with respect to the operating conditions are applied to specimens of the components under investigation. The time to failure of the specimens is determined through the measurement of particular properties of the materials, which correlate to the deterioration level of the component. From an analysis of the times to failure for each stress level applied, a projection of the results is done in order to estimate the time to failure, which reflects and emulates the lifetime of the same components for the stress level experienced under operating conditions [160].

Although the accuracy of the projected time to failure of the component cannot be guaranteed, the implementation of accelerated ageing tests is widely spread since testing over the real lifespan of the component would be unpractical both from an economical point of view and due to the unacceptable amount of time required for the specimens to fail.

In Section 5.2.1, a review of the existing standards and works which treat accelerated ageing tests for winding electrical insulation systems is conducted. Although there is not a standard providing a well-defined procedure concerning

accelerated thermo-mechanical ageing tests, valuable information can be collected from the existing standards for different type of tests which can help in the definition of the accelerated ageing tests to be conducted for this work.

In Section 5.2.2, an experimental procedure for the conduction of accelerated thermo-mechanical ageing tests is proposed. The experiment's design decisions are discussed, the tests setup is explained and the experimental results are presented and discussed. The results obtained are employed for the tuning of the lifetime prediction model free parameters, as shown in Section 5.2.3, where a tuning procedure is presented.

Finally, Section 5.2.4 provides a sensitivity analysis of the model, where it is investigated how severely the uncertainties of the tuned parameters cause inaccuracies in the insulation system lifetime prediction.

5.2.1 Accelerated ageing tests' review

The main method adopted for the assessment of the endurance to stresses of the insulation system is the collection of data from specific accelerated ageing tests. During these tests, the stresses applied to the insulation are higher than the ones generated during operations. This is done in order to increase the deterioration rate of the insulation and thus save testing time. The basic strategy adopted is to conduct tests where different stress levels are applied, with the aim to develop a law describing the relationship between the level of the stress applied and the time to failure of the insulation system. Considering the complexity of the proposed procedure, a considerable amount of ageing tests need to be performed, in order to discern the effect of each single stress and of the combined stresses on the insulation lifetime [161], [56].

5.2.1.1 The statistical approach

The outcome of an ageing test is almost never of deterministic nature. Identical specimens aged by applying the same stress level can have different time to failure. To mitigate this aspect, multiple identical specimens of the insulation system are aged under the same stress levels. A statistical analysis of the different time to failure of the tested specimens is conducted in order to determine the average behaviour of the insulation under that stress. Typically, the resulting times to failure of different specimens are assumed to be normally distributed, although any normality test can be used for verifying this assumption because of the small size of the sample [162], [163]. The sample mean $\bar{x}$ and the sample variance s^2 can be calculated as in (5.12) and (5.13), respectively, where n is the sample size and x_i is the time to failure of the i-th specimen.

$$\bar{x} = \frac{1}{n}\sum_{i=1}^{n} x_i \tag{5.12}$$

$$s^2 = \frac{1}{n-1}\sum_{i=1}^{n} (x_i - \bar{x})^2 \tag{5.13}$$

The sample mean represents the most probable time to failure for a given stress, whereas the variance provides a measure of how big is the deviation of the results from the mean value. The sample mean and sample variance tend to the normal distribution's mean and variance, respectively, as the number of specimens n tends to infinity. Thus, the higher the number of specimens, the more accurate will be the estimation of the most probable time to failure. Thus, there must be a minimum number of specimens in order to obtain statistically significant results.

In addition to the determination of the number of specimens to be aged for a specific stress level applied, it is necessary to determine how many different stress levels the accelerated ageing test should be repeated for. This is required in order to be able to extrapolate a trend of the mean time to failure respect to the stress level applied, and thus estimating the time to failure for stress levels different from the tested ones. In the main endurance assessment standards, it is recommended to conduct at least three tests for different stress levels [123]. A regression analysis can be successively performed on the data collected, in order to find the curve which best fits the points experimentally determined on the (stress level applied, mean time to failure) plane.

The selection of the curve fitting method depends on the ageing model considered for the specific stress. In general, for simplicity reasons, the models are selected in such a way that a linear representation of the relationship between stress level and time to failure can be found. For instance, this is true for the Arrhenius model, which is commonly implemented for thermal ageing lifetime modelling, as well as for the inverse power law models, which are used for electrical or mechanical ageing lifetime modelling. In the case a linear representation is available, then a linear regression analysis can be performed in order to identify a function representing the lifetime related to the stress level applied. For instance, for the Arrhenius model introduced in (5.1), which is used for representing the lifetime of the insulating material related to the thermal stress, a linear representation can be obtained as for (5.14), by applying the logarithm function at both sides of (5.1).

$$y = a + bx \tag{5.14}$$

$$y = \log(\mathcal{L}_T)\,,\;\; x = \frac{1}{T - T_0}\,,\quad a = \log(\mathcal{L}_0)\,,\quad b = Q$$

Considering (5.14), a linear regression can be used for identifying the best fitting linear function [123]. In particular, the coefficients *a* and *b* can be calculated, using the linear regression method, as shown in (5.15) and (5.16), respectively, from which the values of the free parameters $\mathcal{L}_0$ and Q of the lifetime model of (5.1) can be computed [123]. In (5.15) and (5.16), x_i and y_i are values of *x* and *y* of (5.14), calculated from the results of the i-th accelerated ageing test conducted at temperature $T = T_i$, which provides a mean time to failure $\mathcal{L} = \mathcal{L}_i$, whereas n_t is the amount of ageing tests performed.

$$a = \frac{\sum_{i=1}^{n_t} x_i y_i - \frac{1}{n_t}\sum_{i=1}^{n_t} x_i \sum_{i=1}^{n_t} y_i}{\sum_{i=1}^{n_t} x_i^2 - \frac{1}{n_t}\left(\sum_{i=1}^{n_t} x_i\right)^2} \tag{5.15}$$

$$b = \frac{1}{n_t}\sum_{i=1}^{n_t} y_i - \frac{b}{n_t}\sum_{i=1}^{n_t} x_i \tag{5.16}$$

5.2.1.2 End of life of a specimen

The accelerated ageing tests are typically conducted for determining the time to failure of the insulation under a specific stress. Thus, during the design of the tests, it is important to define what is intended for failure of a specimen. In general, in order to determine the failure of a specimen, some diagnostic tests are conducted after every ageing cycle. Thus, the test will be divided in cycles. Each cycle will be composed of an ageing sub-cycle where the stress is applied to the specimens, followed by a diagnostic sub-cycle where the conditions of the specimens are checked. In particular, during the diagnostic sub-cycles, some

specific physical properties which can indicate deterioration of the insulation are measured. The failure of the specimen is then declared when the value of one of the physical properties falls below a threshold value under which the insulation system is considered excessively weak.

Some of the most common diagnostic tests are the measurement of insulation capacitance, resistance, dissipation factor, and partial discharge activity [164], [165]. The advantage of these tests is that they are non-disruptive tests, which means that the insulation is not damaged by the measurements procedure. On the other hand, the values measured during these diagnostic tests are not completely reliable, and can lead to false detection of deterioration [166]. For these reasons, in order to assess a failure of the insulation, disruptive tests are often implemented, such as the dielectric withstanding voltage test [164]. During this test a high voltage lower than the nominal breakdown voltage is applied to the insulating material. As the material deteriorates, the actual breakdown voltage decreases. Thus, the failure of the specimen is declared when there is a breakdown when the test voltage is applied.

Another important aspect in the design of the accelerated ageing test, is the physical definition of the specimen and how to apply the stress to the specimen. In order to obtain reliable results, it is critical to use specimens which are similar or identical to the windings under investigation. The stresses applied during the ageing tests also need to be similar to the stresses applied to the windings in the real motor. The easiest solution for achieving this is to perform the ageing tests with the windings inserted in the motor. However, this solution is not cost effective as in each test an entire motor is aged. More often, in the interest of

reducing the costs of the experiment, equivalent motorettes are implemented which reproduce and emulate the winding insulation system in the most accurate possible way [140].

5.2.1.1 Existing standards

Standard procedures for the evaluation of the endurance of electrical insulation systems under specific stresses have been developed through the years, mainly for aiding manufactures in assessing the quality of the produced insulation systems. The main recognized standards are published by the International Electrotechnical Commission (IEC), the National Electrical Manufacturers Association (NEMA), and the IEEE Standards Association [167]. In particular, concerning our final scope, which is to assess the ageing of the windings under thermal and thermo-mechanical stresses, standard procedures are available for the assessment of the lifetime of the winding insulation system under thermal stress, whereas only useful guidelines are provided for the assessment of the deterioration due to thermo-mechanical ageing.

In [140], which is an IEC standard, a procedure for the evaluation of the lifetime of the winding insulation related to thermal ageing is proposed (an equivalent IEEE standard procedure can be found in [109]). This standard is often used by the windings manufacturer for certifying the thermal rating of a specific magnetic wire. According to this standard, either windings mounted in the motor or on a motorette can be implemented as specimens of the test. The temperature can be imposed indifferently by means of the Joule losses generated by forcing a DC current in the windings conductor, or by using an environmental chamber. Although with the first method the heat source is at the same position as during

operations, the oven allows setting more precisely the ageing temperature. Three accelerated ageing tests are recommended at three different temperatures in order to have reliable results from the linear regression analysis shown in (4.15) and (4.16). The temperature gap between different tests should be higher than 20 °C. At least 5 specimens should be aged for each tests, for the sake of obtaining statistically meaningful results.

The standard proposed in [140] provides also a recommendation about the length of each ageing sub-cycle. In particular, the interval between each diagnostic sub-cycle should be such that at least 10 complete cycles are performed before failure of the specimens. The length of the ageing sub-cycle is selected on the base of the expectation of the specimen endurance and it is different according to the test temperature. It is important to choose carefully this value because the length of the ageing sub-cycles set the resolution of the experiment. In fact, from the diagnostic tests performed at the end of the ageing cycle, it cannot be determined at what exact time a specimen has eventually failed. Thus, the resolution in the measurement of the time to failure of a specimen is equal to one ageing sub-cycle length.

Finally, a dielectric withstanding voltage test is recommended in [140], in order to determine the time to failure of each specimen, because it has a low risk of false failures detection.

Some guidelines for the evaluation of the effect of thermo-mechanical stress on the winding electrical insulation are proposed in [141] by the IEC and in [168] by the IEEE. In [141], similar recommendation as in [140] are provided for the selection of the test specimens, which can be either windings placed in the motor,

or assembled on a motorette, or in the simplest case the tests can be conducted on unrestrained coils. At least five specimens for each test should be aged in order to get a good statistic of the results.

Although for the accelerated ageing tests related to the thermal stress the constant temperature could be set by using an environmental chamber, this is not advisable for the assessment of thermo-mechanical ageing. In fact, thermo-mechanical stress is mainly caused by the temperature difference between conductor and insulation, which causes different expansion rate and thus shear stress on their bonding surface. Thus, in order to recreate a similar temperature distribution in the windings as during operations, in [141] it is recommended to heat up the coils by means of Joule losses generated by forcing a current flow through the conductor.

In order to age the specimens only by means of the mechanical stress caused by thermal expansion of the materials while minimizing the effect of thermal ageing, the specimens could be aged by means of thermal cycling at temperatures lower than a threshold temperature under which thermal ageing can be neglected. In this way, the complications arising when multiple stresses are applied are minimized. However, the deterioration rate caused by thermo-mechanical ageing only could be too small and thus the time to failure during this ageing tests could be unpractical. For this reason, in [141], specimens of the windings are aged for a fixed amount of thermal cycles, followed by a voltage endurance test. A procedure for the voltage endurance test is presented in [169]. During this test, a power frequency voltage of higher amplitude then the insulation system nominal voltage is applied to the specimen until breakdown of the insulation. The time to

breakdown provides information about the electrical endurance of the insulation system.

The results of the voltage endurance test conducted on the previously aged specimens by means of thermo-mechanical stress, are compared to the results of the same voltage endurance test conducted on unaged specimens. From the comparison of the time to breakdown for the two different cases, it is possible to observe the contribution of the thermo-mechanical stress in the deterioration of the winding electrical insulation.

Although the procedure allows to determine how severe is the effect of thermo-mechanical stress on the tested specimens, it does not allow to obtain a time to failure related to thermo-mechanical ageing only. Thus, this procedure cannot be implemented for the tuning of the free parameters of the multi-stress lifetime model proposed in the previous section. For this reason, in the next section, a specific accelerated ageing test procedure tailored for the tuning of the free parameters of the proposed lifetime model is presented.

5.2.2 Thermal cycling accelerated ageing test for the tuning of the lifetime consumption model

The tuning of the free parameters of the lifetime model given in (5.8) can be based on the results of specific accelerated ageing tests. In this section, an accelerated ageing test procedure is proposed, whose results will be used for the tuning of those free parameters. The procedure follows the guidelines provided in the standards presented in the last section. However, some modifications have been proposed in order to directly relate the time to failure due to thermo-

mechanical stress, without the need of disruptive voltage endurance tests, in contrast with the guidelines proposed in [141], [168].

During the accelerated ageing test, specimens of the windings implemented in the designed motor have been aged by applying repetitive temperature cycles. In [141], it is recommended to conduct the thermal cycles at sufficiently low temperatures in order to minimize the effects of thermal ageing in the deterioration process of the insulation. In contrast to this, the used ageing temperature profiles have been selected in a range of temperatures higher than the operating ones. Although in this way during the ageing test both thermal and thermo-mechanical stresses influence the insulation life consumption, the specimens will endure a reasonably short amount of time before failure, thus making unnecessary the adoption of any voltage endurance test. A direct relationship between stresses applied and time to failure of the specimens can therefore be deduced.

In the multi-stress lifetime model of (5.8) there are four free parameters, $\mathcal{L}_0$ and Q which are related to thermal ageing and k and N which shape the effect of thermo-mechanical ageing. The tuning procedure of these free parameters has been divided in two parts. Firstly, the unknowns related to thermal ageing have been tuned on the base of classic accelerated ageing tests conducted at constant temperatures, following the procedure of [140]. Successively, the remaining parameters related to the thermo-mechanical stress have been calculated on the base of the results of the accelerated ageing tests presented in this section.

The winding type which has been tested is the one implemented for the designed SMPM motor, which is the Grade 2 Magnebond CB-180, a polyesterimide

enamelled copper wire overcoated with a polyamide aromatic bondcoat. The thermal index of the selected winding is 180 °C, which means that at a constant temperature equal to 180 °C, the most probable time to failure of the winding is after 20,000 hours. The conductor diameter is equal to 0.40 mm. The minimum breakdown voltage of the unaged wire is 4.4 kV.

The thermal endurance graph for the investigated magnetic wire is provided by manufacturer and is shown in Figure 5.4, which is a log-log plot, where on the x-axis there is the inverse of temperature, whereas on the y-axis there is the average lifetime related to the temperature. In this way, it can be observed that as shown in (5.14), the relationship between the logarithm of the lifetime and the inverse of temperature is linear.

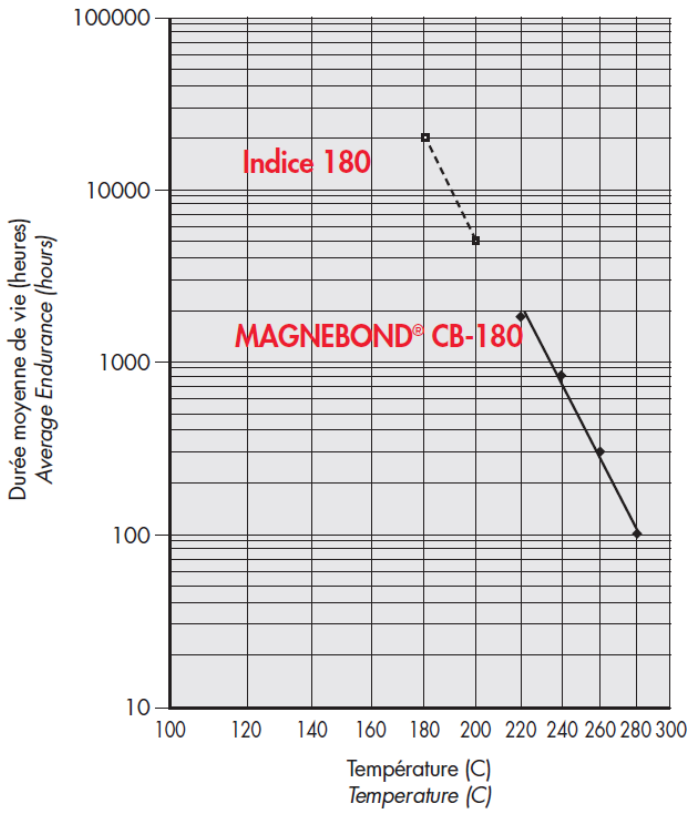


Figure 5.4: Average endurance of the Magnebond CB-180 magnetic wires for different temperatures applied [170].

From the data shown in Figure 5.4, the free parameters Q and $\mathcal{L}_0$ of the lifetime model related to thermal ageing, represented by (4.1), can be easily computed. However, these values have also been verified experimentally through the implementation of accelerated thermal ageing tests.

5.2.2.1 The experimental setup

The specimens utilized in the tests are composed of two coils of twenty turns each, wound together. The two coils are hold together using Kapton polyamide film with silicone adhesive, because of the high resistance to temperature of this tape. A picture of one specimen is shown in Figure 5.5. Two coils are required for each specimen in order to perform the diagnostic measurements on the wires' electrical insulation. For each experiment, 15 identical specimens have been

aged through the application of the same temperature profile, in order to obtain a relevant statistic of the resulting specimens' times to failure.



Figure 5.5: One specimen of the winding tested through accelerated thermo-mechanical ageing tests, composed of two coils wound together.

All the specimens have been placed in a sealed metal box, in order to prevent the risk of fire hazard and the emission in the room of toxic fumes. The specimens have been evenly distributed in the box, by hanging them to a grid, as shown in Figure 5.6.



Figure 5.6: Specimens placed in the sealed box for the accelerated ageing test.

The main advantages of adopting this configuration for the specimens are:

- Cost reduction since there is no support for the windings to be manufactured and the coils have not to be inserted in the slots;
- Minimization of the thermal interaction between different specimens, which makes the experiment modular, with respect to the use of the real motor where the number of windings are fixed and they are not thermally isolated. In particular, after one of the specimens in the motor fails, the temperature distribution would be uneven causing slightly different temperature profiles on different specimens;

Although the temperature distribution of the specimens will be different from the temperature distribution of the motor windings due to the absence of the

stator which works as a heat sink, the results of the model can be used for predicting the time to failure of the motor windings. In fact, the effects of thermo-mechanical and thermal stress have been related to the hot spot temperature profile of the system, because in that location the stress levels will be maximum. Thus, it can be supposed that the failure of the specimen is more likely to happen near its hot spot. If the hot spot of the specimen and the one of the implemented winding have the same temperature profile, then it can be assumed that they will have equal most probable time to failure.

The temperature in the specimens is measured through the use of K-type thermocouples inserted in the core of the windings. Eight different temperature measurements are recorded from eight different specimens and at different axial position. The highest temperature recorded is considered as the hot spot temperature of each specimen. This strategy allows to increase the accuracy of the measurements and at the same time prevents the test from interruptions in case of failure of a thermocouple. It has to be noted that this procedure is valid under the assumption of identical specimens heated up in the same manner.

The thermocouples tips have been fixed to the windings through the use of Thermigrease TG20030, which is a silicon based thermally conductive paste. Its function is to improve the thermal conductivity from the winding to the thermocouples tip in order to increase the temperature measurements accuracy and at the same time to ensure the contact between thermocouple tip and wire surface. The main advantages of this thermal paste are that it is high temperature resistant, it remains soft and thus does not add any mechanical stress on the windings surface. Also, it being not electrically conductive removes the risk of

accidental current flow from the winding conductor through the temperature sensor.

During the experiment, the specimens have been heated up by means of Joule losses generated by the flow of electrical current in the windings' conductor, as recommended in [141]. In order to obtain a similar temperature in each specimen, the same current has to flow through each conductor. For this reason, during each test the specimens were series connected to an EA PSI-8360 15-T Programmable DC Power Supply. The Power supply was controlled by a Raspberry Pi 3 computer. In particular, the General Purpose Input-Output interface (GPIO) of the Raspberry Pi has been utilized for setting the DC current of the Programmable Power Supply, through the control of a multiple-Channel Relays module connected to the analogue interface of the Power Supply. The GPIO has been used also for acquiring the temperature measurements from the thermocouples inserted in the specimens. In particular, the signals from the thermocouples were interfaced to the GPIO through the use of MAX31855 converters, which perform the cold junction compensation of the signal and digitalize the temperature measurements. Figure 5.7 shows the accelerated ageing tests configuration, whilst Figure 5.8 illustrates a scheme of these tests.

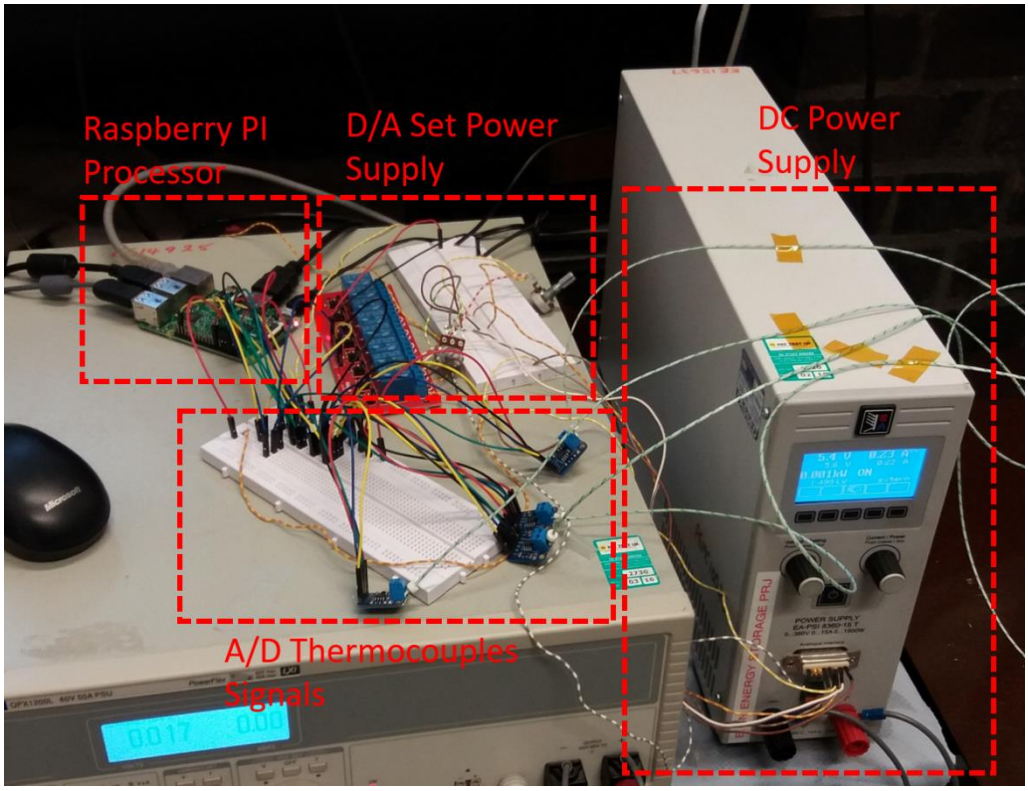


Figure 5.7: Setup of the accelerated ageing tests.

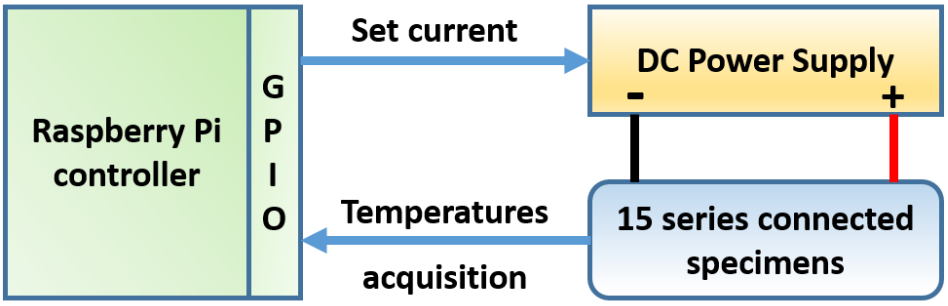


Figure 5.8: Accelerated ageing tests scheme.

For each experiment, the specimens have been aged under a specific temperature cycle imposed by a temperature controller loaded on the Raspberry Pi 3. Cycles of 24 hours tests have been performed on the specimens, followed by a diagnostic test where the specimens' insulation system conditions where checked. The diagnostic test was performed by using a Fluke 1550C Insulation

Tester, which measures the insulation resistance through the application of a DC voltage up to 1 kV and the measurement of the generated leakage current. In particular, after having disconnected all the coils, each terminal of the tester was connected to the conductor of one of the two coils of the same specimen. In this way, a measure of the electrical resistance of the insulation system of one specimen could be obtained. The resistance of the specimens was noticed to be higher than 1TΩ for most of the specimens' life, followed by a significant resistance drop below 1GΩ near the end of their lifetime, due to the reduction of the breakdown voltage as the insulating materials deteriorated. Considering this, then it was decided to declare the end of a specimen's life when its insulation resistance dropped below 1GΩ.

5.2.2.2 The tests

The test rig has been used for performing three different ageing tests under different temperature profiles.

The first type of test aims at proving the validity of the data provided by the manufacturer in Figure 5.4 concerning the thermal endurance of the insulation system stresses by a constant temperature. Thus a constant temperature is applied to the specimens during this accelerated test. The input of the algorithm is the target constant temperature T_{const} to be maintained during the ageing cycle. The DC current I_{const} flowing in the windings when the Power Supply is on has to be selected in such a way that the Joule losses generated are high enough to heat the specimens up to the temperature T_{const}. On the base of the highest temperature T_{now} measured from the thermocouples at each step, the Power Supply is switched on (PS=1) and off (PS=0) according to the conditions below,

where δ_T represents the temperature tolerance around the target constant temperature which is added in order to avoid repeated switching of the Power Supply.

- If $T_{now} < T_{target} - \delta_T$, then PS=1;
- If $T_{now} > T_{target} + \delta_T$, then PS=0.

Figure 5.9 shows the temperature acquisition over 1 minute, for the case of T_{const} equal to 265 °C and δ_T equal to 0.1 °C, where it can be see that the winding temperature oscillates around the target temperature selected.

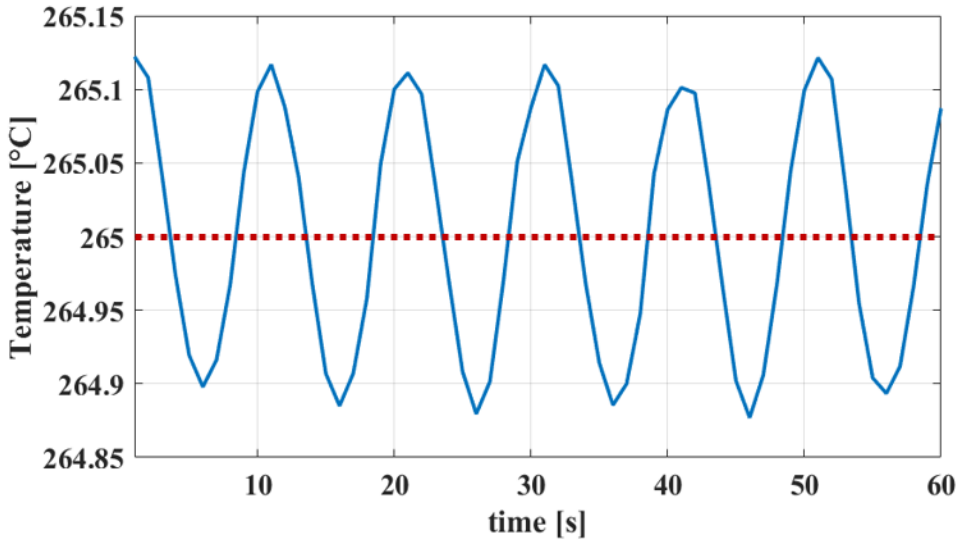


Figure 5.9: Specimens temperature acquisition when the constant target temperature is equal to 265 °C.

The second type of test is designed for ageing the specimens under thermal and thermo-mechanical stresses. The results of the tests are used for tuning the free parameters *k* and *N* of the lifetime consumption model proposed. In order to do this, the specimens are aged by applying repeated temperature cycles. During this test, the winding temperature is cycled between a minimum temperature

T_{min} and a maximum temperature T_{max}. In particular, a constant DC current I_{const} is applied for heating up the specimens, whilst no current is applied during the cooling down part of the cycle, where the accumulated heat in the specimens is dissipated by natural convection. The conditions for the temperature controller are:

- If $T_{now} < T_{min}$, then PS=1;
- If $T_{now} > T_{max}$, then PS=0.

Figure 5.10 shows the specimens temperature profile when this controller is employed, where the red dotted lines represent T_{min} and T_{max}.

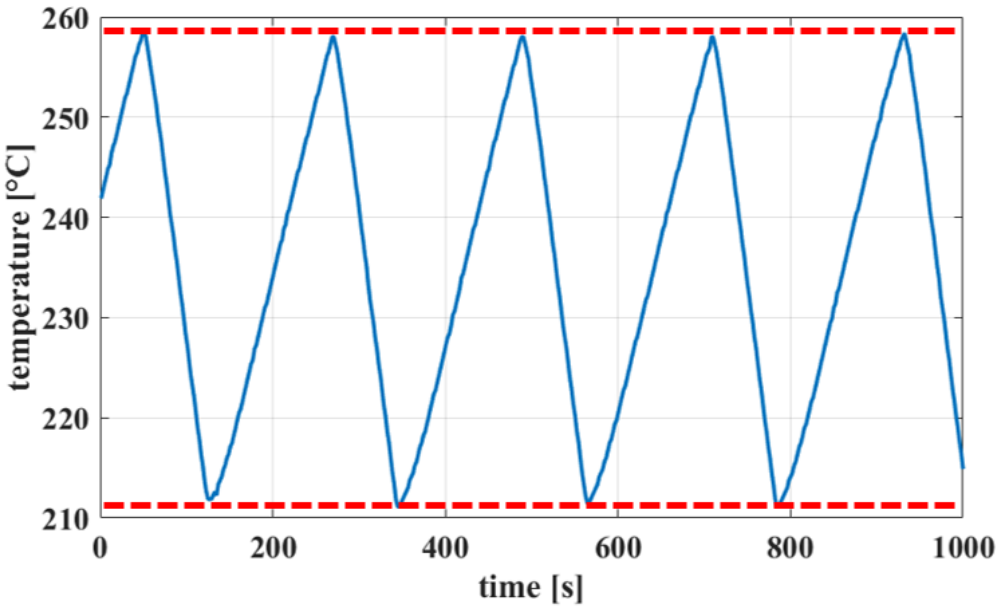


Figure 5.10: Temperature profile for the case of thermal cycling accelerated ageing test, where the dotted red lines represent the temperature limits T_{min} and T_{max}.

The higher is the current I_{const} applied, the steeper will be the temperature increase in the specimens, making the thermo-mechanical stress level more severe.

A third temperature control has been implemented for testing the specimens under a temperature cycle different from the one used for the tuning of the lifetime model. In particular, this temperature controller included a control over the temperature variation. The results of the accelerated ageing tests using this temperature control are used as validation of the tuned lifetime model. As for the previous control, a minimum and a maximum temperature T_{min} and T_{max}, respectively, are selected. The desired constant slope k_s for the temperature variation s_{now} is selected, along with a constant δ_s representing the tolerance around the target slope value. Finally, an auxiliary digital variable k_{aux} is used for keeping track of whether the temperature is in the increasing ($k_{aux} = 1$) or decreasing ($k_{aux} = 0$) part of the temperature cycle. In other words, k_{aux} sets the sign of the slope k_s. Finally, for this controller, instead of switching on and off the power supply, its DC current *I* is regulated by using the digital interface of the power supply. After having fixed a nominal current I_n, the conditions respected by the algorithm are:

- If $T_{now} < T_{min}$, then $I = I_n$, $k_s = 1$;
- If $T_{now} > T_{max}$, then $I = 0$, $k_s = 0$;
- If $T_{min} < T_{now} < T_{max}$ and $k_s = 1$ and $s_{now} < k_s - \delta_s$, then $I = I * 1.1$;
- If $T_{min} < T_{now} < T_{max}$ and $k_s = 1$ and $s_{now} > k_s + \delta_s$, then $I = I * 0.9$;
- If $T_{min} < T_{now} < T_{max}$ and $k_s = 0$ and $s_{now} < -k_s - \delta_s$, then $I = I * 1.1$;

- If $T_{min} < T_{now} < T_{max}$ and $k_s = 0$ and $s_{now} > -k_s + \delta_s$, then $I = I * 0.9$.

In the next section, the results of the accelerated ageing tests conducted following the procedures illustrated herein will be shown. On the base of these results, a tuning procedure for the free parameters of the lifetime consumption model presented will be illustrated and discussed.

5.2.3 Tuning of the lifetime consumption model on the base of the accelerated ageing tests results

5.2.3.1 Thermal ageing parameters

As explained in the last section, the parameters $\mathcal{L}_0$ and Q, which shape the ageing rate related to thermal ageing, can be derived from the graph of Figure 5.4. However, in order to validate the data Figure 5.4 for the specimens employed, two accelerated ageing tests at two different constant temperatures have been conducted, the first one at 260 °C and the last one at 240 °C. The time to failure of the 15 specimens aged at constant temperature equal to 260 °C are shown in Figure 5.11, whereas the time to failure for the case of applied temperature equal to 240 °C are reported in Figure 5.12. For the ageing test conducted at 240 °C, one of the specimens failed after only 51 hours. It was then decided not to include this value in the analysis as early failures are more likely to be due to imperfections of the insulation or to a damage caused during the specimens manufacturing, rather than to thermal ageing [159].

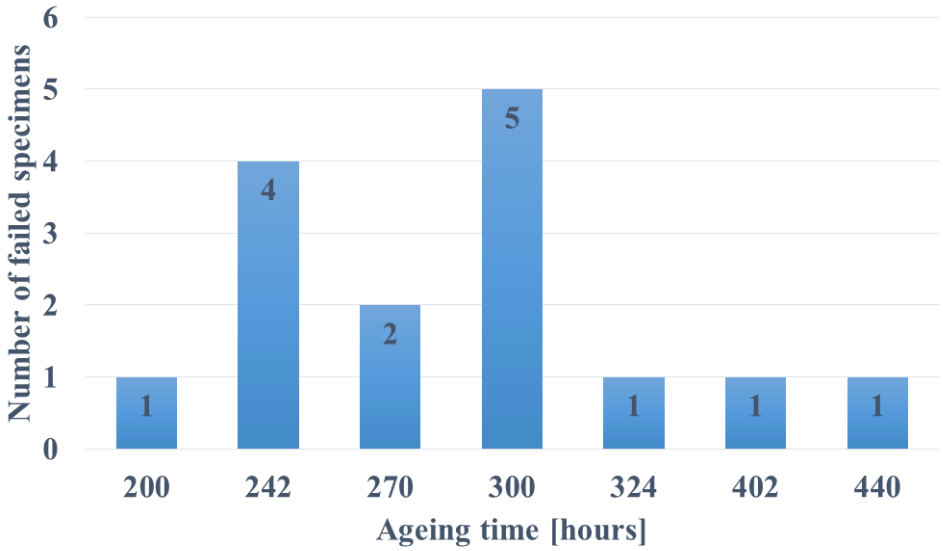


Figure 5.11: Time to failure of the specimens aged at constant temperature equal to 260 °C.

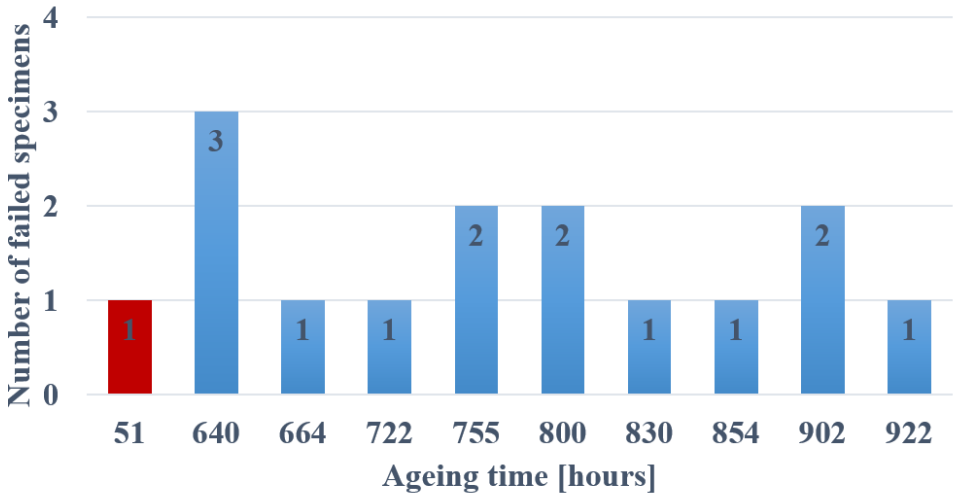


Figure 5.12: Time to failure of the specimens aged at constant temperature equal to 240 °C.

The mean time to failure of the specimens aged at 260 °C is calculated as in (5.12) and is equal to 292 hours, which is similar to the data provided by the magnetic wire manufacturer of 300 hours. If the sample variance s^2 is calculated using (5.13), then the 95% confidence interval of the results can be provided for

normally distributed samples as shown in (5.17) [159], where $\bar{x}$ is the sample mean, N_s the number of specimens, and μ is the mean of the distribution.

$$\Pr(\bar{x} - 1.96\sqrt{s^2/N_s} < \mu < \bar{x} + 1.96\sqrt{s^2/N_s}) = 0.95 \qquad (5.17)$$

Applying (5.17) for the results of the accelerated test conducted at constant temperature equal to 260°C, it can be said that with 95% probability, the mean time to failure of the distribution is between 260 and 323 hours.

Using the same equations, it was found that for the ageing test conducted at 240°C the sample mean is equal to 773 hours, which is close to the manufacturer time to failure which is equal to 800 hours. The 95% confidence interval of the mean time to failure is between 732 and 814 hours.

Since the results of the two accelerated ageing tests conducted confirm the data provided by the manufacturer for what concerns the windings lifetime related to thermal stress, than the parameters of (5.1) were calculated on the base on these data. In particular, as reference temperature, it has been chosen T_0 equal to 180°C, which is the temperature index of the magnetic wire considered herein. From Figure 5.4, it can be seen that the lifetime $\mathcal{L}$ of the specimens at temperature T_0 is equal to 20,000 hours. Finally, the parameter Q is computed by solving (5.1) for another point of the straight line of Figure 5.4, obtaining that Q is equal to 2318.

5.2.3.2 Thermo-mechanical ageing parameters

Following the tuning of the parameters which shape the ageing due to thermal stress, two accelerated ageing tests, using the second temperature control presented in the last section, are conducted with the aim of tuning the remaining

parameters of the lifetime consumption model. The two tests have been conducted between the same minimum and maximum temperature, which are equal to 215 and 265 °C, respectively, but by applying a different DC current during the heating up part of the thermal cycle. In this way, the slope of the two temperature profiles are dissimilar and thus different thermo-mechanical stress levels are applied.

During the first accelerated thermal cycling ageing test, the 15 specimens have been aged by means of temperature cycles, with a DC current applied during the heating up part of the cycles equal to 4.5 A DC. Figure 5.13 shows the temperature of the specimens on a 1000 seconds time window.

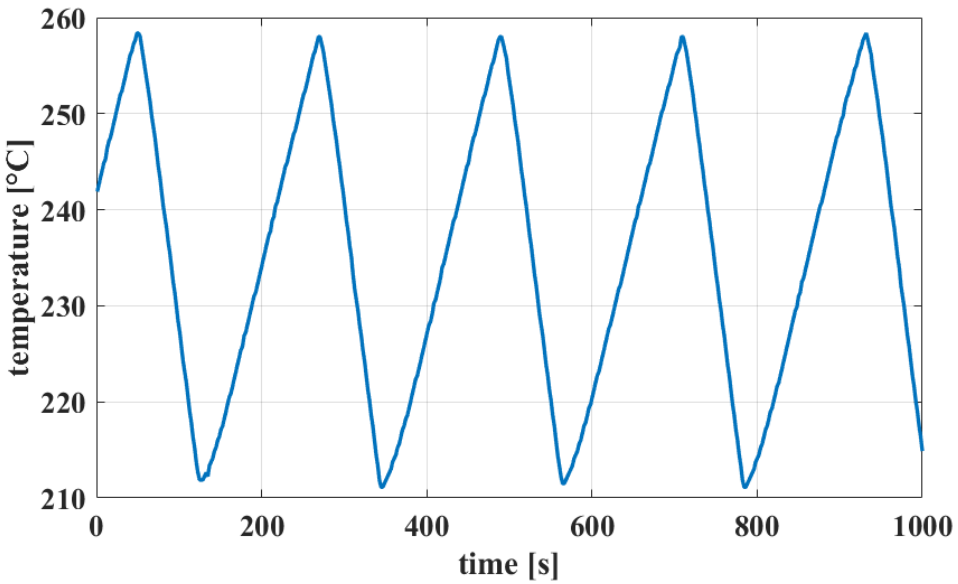


Figure 5.13: Temperature profile of the specimens during the first accelerated ageing test for the tuning of the free parameters k and N, with an applied DC current equal to 4.5 A.

The time to failure of each specimen has been acquired and the results of the accelerated ageing test are reported in Figure 5.14. The sample mean time to

failure is equal to 503 hours and the 95% probability confidence interval is between 500 and 506 hours. The narrow confidence interval is due to the fact that most of the specimens failed during the same diagnostic sub-cycle, thus causing a small variance of the specimens' time to failure.

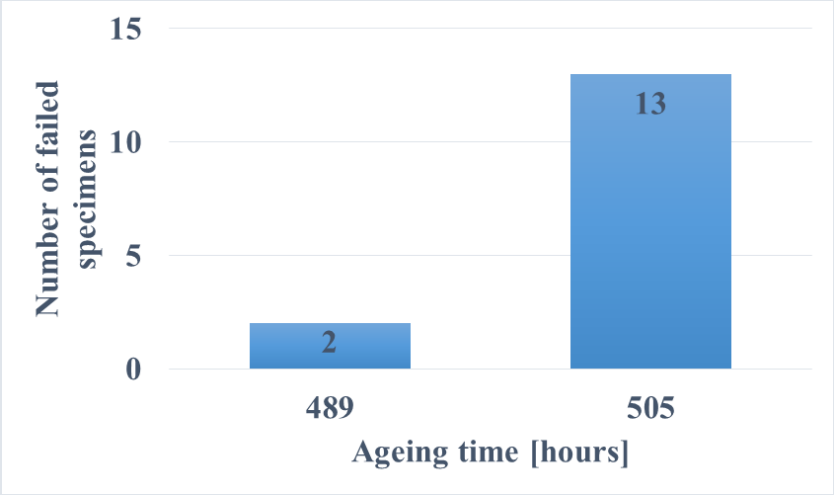


Figure 5.14: Time to failure of the specimens aged under thermal and thermo-mechanical stress applying the temperature profile of Figure 5.13.

The second accelerated ageing test has been conducted by applying a DC current equal to 8 A during the heating up part of the temperature cycles. Thus, with respect to the previous test, the temperature rise was steeper because the current applied was almost doubled. This aspect can be observed in Figure 5.15, where the specimens' temperature profile during a time window of 1000 seconds is illustrated.

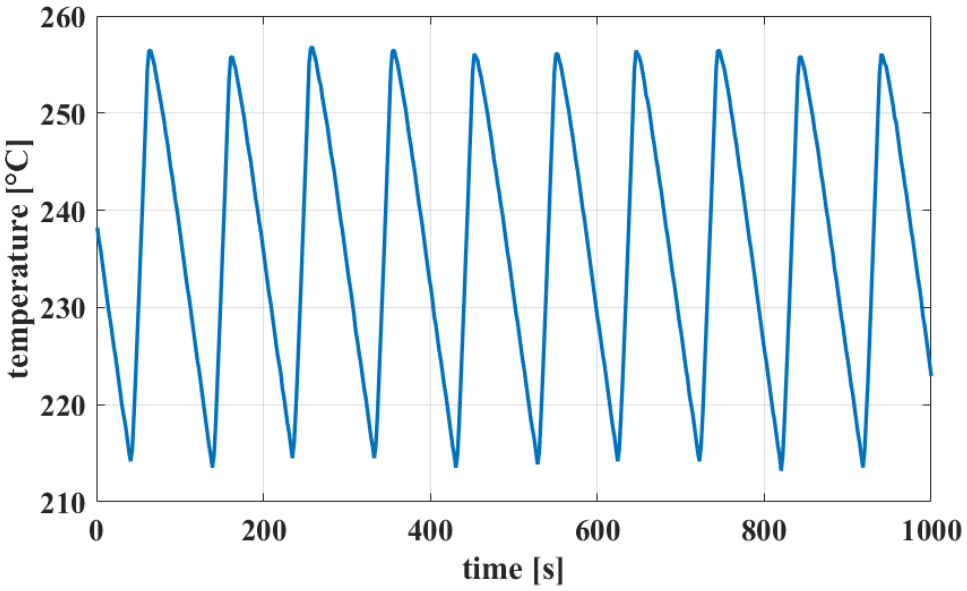


Figure 5.15: Temperature profile of the specimens during the first accelerated ageing test for the tuning of the free parameters k and N, with an applied DC current equal to 8 A.

The time to failure of the specimens for the presented accelerated test are reported in Figure 5.16. The sample mean time to failure is equal to 464 hours and the 95% probability confidence interval is between 458 and 470 hours.

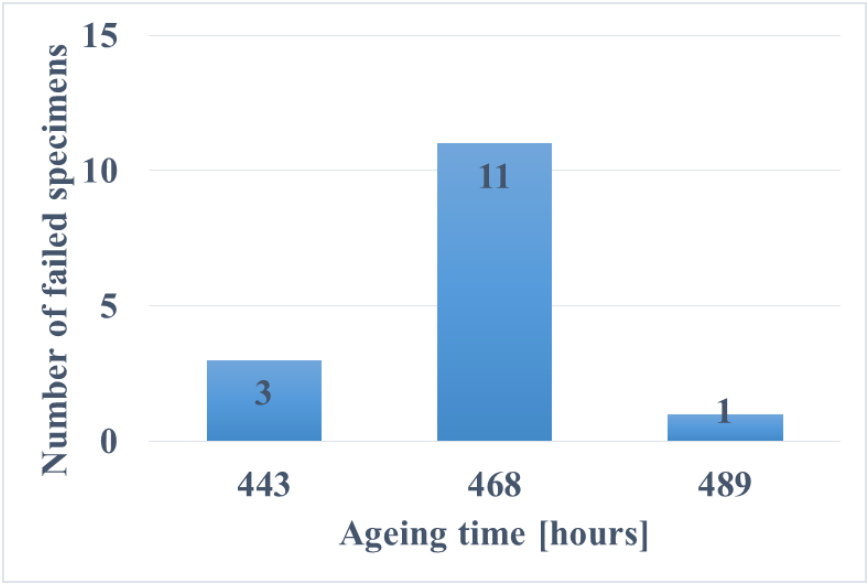


Figure 5.16: Time to failure of the specimens aged under thermal and thermo-mechanical stress applying the temperature profile of Figure 5.15.

The results obtained from the two accelerated ageing tests abovementioned have been used for tuning the parameters *k* and *N* of the lifetime consumption model. In order to do that, since for the tests conducted the same temperature cycle is repeated over the ageing sub-cycle, it was preferred to convert the mean time to failure of the specimens in mean number of cycles before failure, which is easily computed as the time to failure divided by one cycle period. In this way, the tuning procedure can be performed on the base of (5.11), which requires less computational cost, since only the integral function over one temperature cycle period has to be computed.

During the tuning procedure, (5.11) has been considered. Substituting the number of cycles *C* with the mean number of cycles before failure (from the first accelerated ageing test), then the integral on the right-hand side has been calculated for the profile of one temperature cycle of the test. The parameters of the function $\mathcal{L}$ related to thermal ageing have been fixed equal to the values determined from the accelerated ageing tests under constant thermal stress. Finally, for each value of the free parameter *N* in a specific range of values with sampling interval 0.001, the corresponding value of *k* such that the equality of (5.11) is true has been iteratively found. In other words, all the pairs (*k, N*) for which the prediction of the lifetime consumption model matches the experimental mean number of cycles have been researched.

The same procedure has been repeated using the results of the second accelerated ageing test, obtaining another set of suitable pairs of free parameters (*k, N*). Thus, the final step of the tuning procedure consisted in finding the unique pair (*k, N*) such that the lifetime model's predictions matches the mean time to failure of

the two accelerated ageing tests conducted. This solution can be found graphically by plotting the two sets of pairs (*k*, *N*) and determining the intersection of the two curves, as shown in Figure 5.17. The values of the free parameters following the proposed tuning procedure are *k* equal to 2.361 and *N* equal to 0.773.

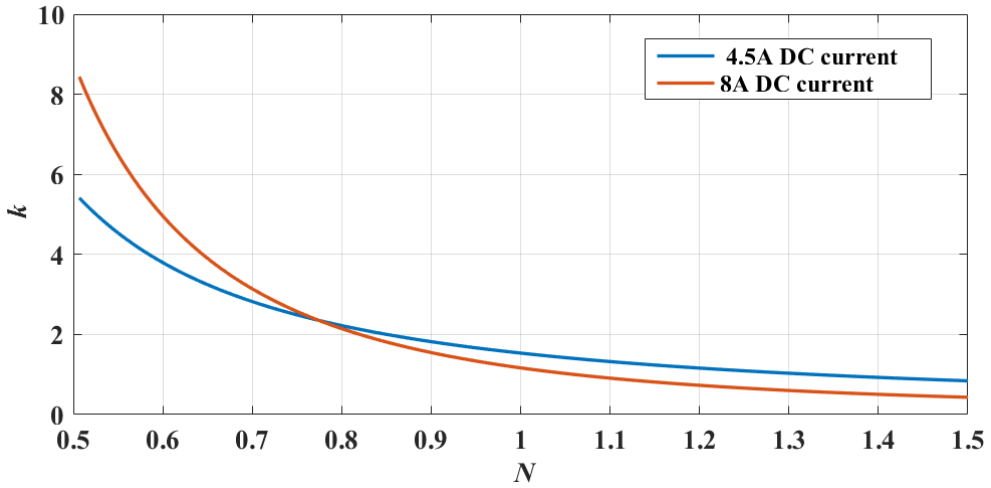


Figure 5.17: two sets of pairs (k, N) for which the lifetime model predictions and the experimental results match.

5.2.3.3 Final validation

A final accelerated ageing test has been conducted with the aim of validating the tuned model. For this test, the specimens have been aged using the third temperature control proposed in the last section, in such a way to age the specimens under a temperature cycle of different shape when compared to the ones employed for the accelerated ageing tests of the tuning procedure. The temperature cycle is shown in Figure 5.18. The time to failure of the specimens for this accelerated ageing test are reported in Figure 5.19. The sample mean

time to failure is equal to 84 hours and the 95% probability confidence interval is between 68 and 101 hours.

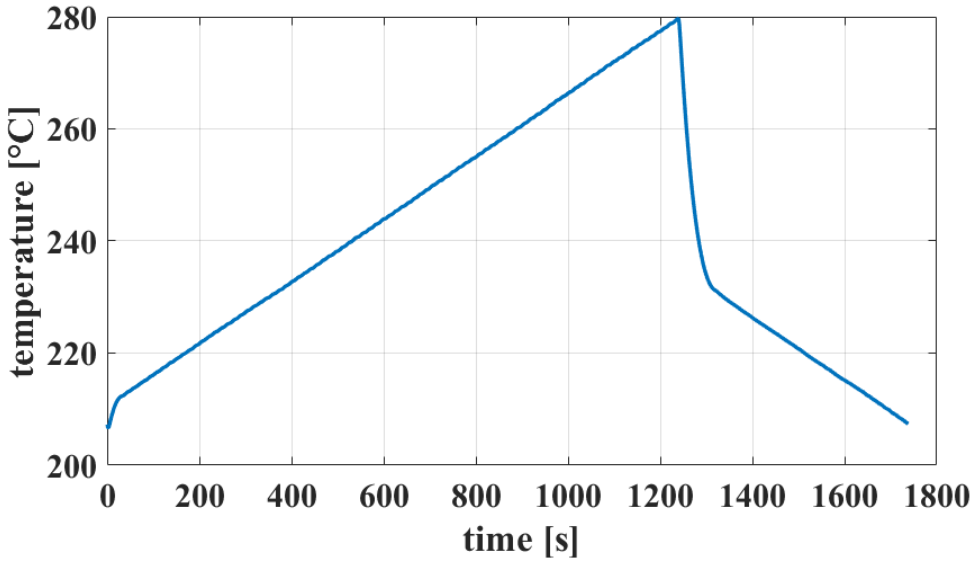


Figure 5.18: Temperature profile of the specimens during one cycle for the accelerated ageing test conducted for validating the lifetime consumption model.

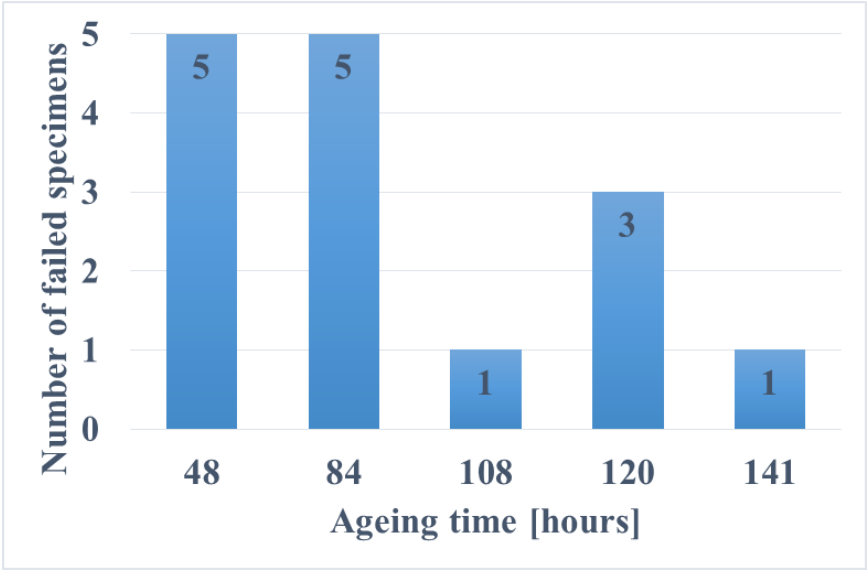


Figure 5.19: Time to failure of the specimens aged under thermal and thermo-mechanical stress applying the temperature profile of Figure 5.18.

The temperature profile of Figure 5.18 has been used as input of the tuned lifetime prediction model of (5.11). The predicted number of cycles before failure equal to 149, which corresponds to a time to failure equal to 72 hours. Although the prediction does not perfectly match the experimental mean time to failure of 84 hours, it can be seen that it falls in the 95% confidence interval experimentally obtained, thus validating the model and showing its adequateness for the proposed work.

In the next section, a sensitivity analysis of the lifetime model parameters *k* and *N* is reported, in order to understand how the uncertainties deriving from the tuning procedure can affect lifetime predictions.

5.2.4 Sensitivity analysis of the tuned parameters of the lifetime consumption model

The tuning procedure proposed in the last section for the free parameters of the lifetime consumption model is based on the results of accelerated ageing tests. These tests are conditioned by a number of intrinsic uncertainties deriving from the specimens manufacturing process, the temperature measurements and the inherent stochastic nature of the ageing process. The uncertainties of the results of the tests could be reflected in some tuning error for the free parameters which could compromise the accuracy of the lifetime predictions.

For this reason, in this section the relationship between uncertainties in the tuning of the free parameters and consequent inaccuracy in the model's predictions is investigated. In particular, since the insulation system ageing relative to thermal stress is well assessed on the base of reliable standards procedure, the sensitivity analysis is focused on the inaccuracies of the model's

parameters *k* and *N*, which are relative to the ageing due to thermo-mechanical stress.

During the first part of the analysis, the temperature cycles of the two accelerated ageing tests conducted for the tuning of the parameters *k* and *N* have been considered. Equation (5.11) has been used for predicting the winding lifetime related to the two temperature cycles in the case of deviation of a single parameter between an arbitrary range reasonably large, comprised between -10% and 10% of its tuned value. For each variation of the parameters, the difference between the lifetime prediction obtained with the tuned parameters and the one calculated with the perturbed parameters have been computed.

The results of the analysis conducted for the case of temperature profile as in Figure 5.13, are reported in Figure 5.20, where the lifetime prediction error is shown for variations of the parameter *k* around its tuned value of 2.361. The prediction error is between -18.2% and +20.8% respect to the prediction obtained using the tuned parameters. Figure 5.21 shows the same results, for the case of variations of the parameter *N* from its tuned value of 0.773. The prediction error with respect to the one obtained using the tuned parameters is between -28.8% and +41.6%.

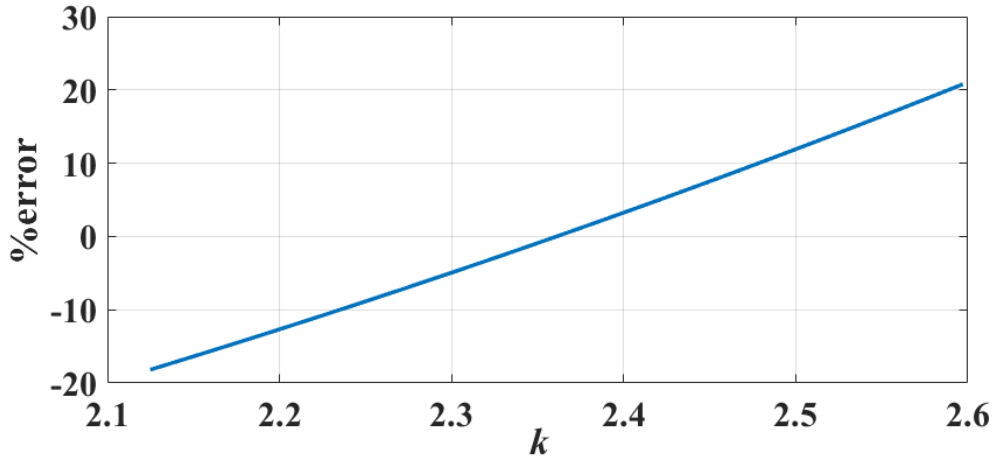


Figure 5.20: Percentage error of the lifetime prediction for different values of the parameter k respect to the lifetime calculated with the tuned parameters, for the temperature profile of Figure 5.13.

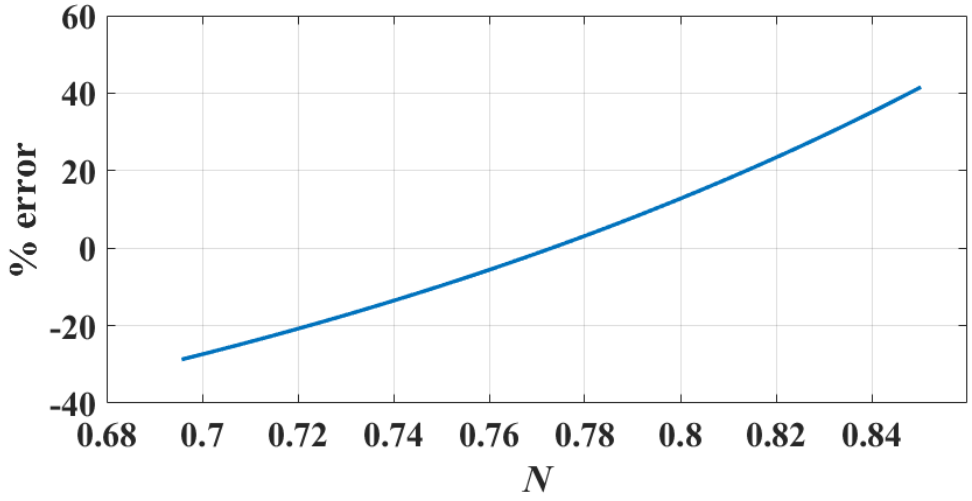


Figure 5.21: Percentage error of the lifetime prediction for different values of the parameter N respect to the lifetime calculated with the tuned parameters, for the temperature profile of Figure 5.13.

The same analysis has been conducted for the temperature cycle of the second tuning accelerated ageing experiment shown in Figure 5.15. The prediction error relative to the prediction obtained using the tuned parameters is shown for the case of variation of the parameter *k* in Figure 5.22, and of *N* in Figure 5.23. It can be noticed that the percentage error of the predictions in case of perturbations

of the parameter *k* is between -20.7% and +24.1%, whereas when the parameter *N* is deviated from its tuned value the range of percentage error in the lifetime prediction is between -44.1% and 99.9%.

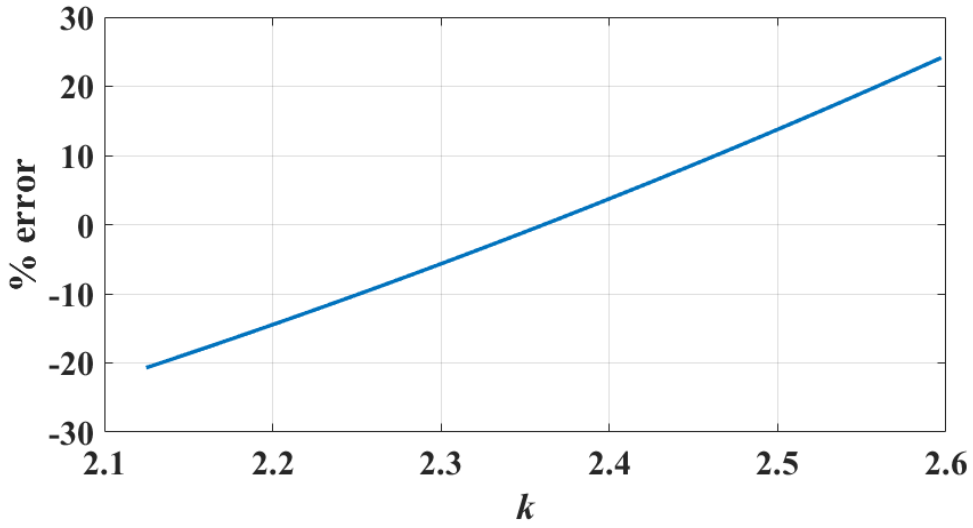


Figure 5.22: Percentage error of the lifetime prediction for different values of the parameter k respect to the lifetime calculated with the tuned parameters, for the temperature profile of Figure 5.15.

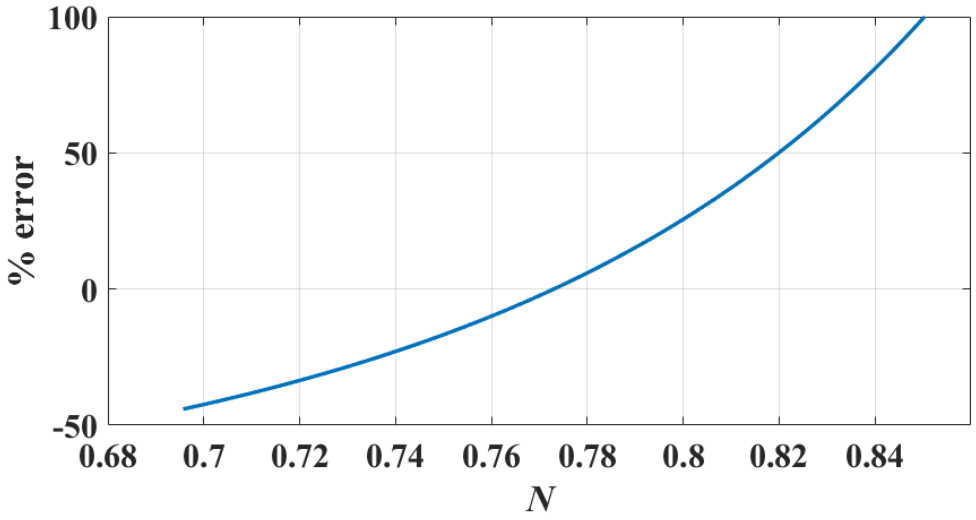


Figure 5.23: Percentage error of the lifetime prediction for different values of the parameter N respect to the lifetime calculated with the tuned parameters, for the temperature profile of Figure 5.15.

The results of the sensitivity analysis show that, for the temperature profiles considered, a variation of 10% in a parameter causes a percentage error on the lifetime prediction up to +99.9%. The error is higher for the case of variation of the parameter N with respect to the error obtained varying the parameter k, because in the model N is an exponential term whereas k is a multiplicative parameter.

The error is significantly higher for the prediction related to the second temperature profile because this profile is characterized by a steeper temperature rise respect to the other temperature profile. Thus, since the thermo-mechanical stress will be more severe for higher temperature variations, then an error in the tuning of the parameters which model this stress type will cause a higher error in the lifetime prediction.

Following these considerations, it can be argued that the high percentage error values obtained in the analysis might be amplified by the specific selection of the temperature profiles, which are the ones used for the accelerated ageing tests. The stress levels generated by these temperature profiles are higher than the stresses the windings are exposed to during operations, because of the requirements of the accelerated ageing tests. Thus, it can be expected that the lifetime prediction error is smaller under operating conditions.

In order to analyse this aspect, the same analysis has been conducted considering a temperature cycle for which the winding lifetime prediction using the tuned model is equal to 20,000 hours, that is the typical target lifetime required by the standards for the classification of endurance of the insulation system under specific stresses. The temperature cycle is shown in Figure 5.24 and it is

characterized by 60 seconds of heating up period followed by 140 seconds of cooling down period. The lifetime is derived calculating the number of cycles the winding withstands before failure as predicted by (5.11).

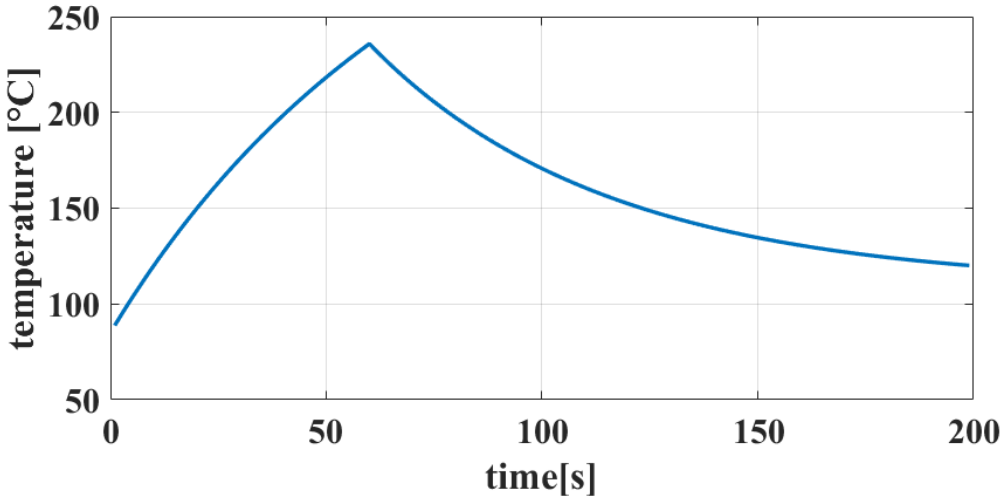


Figure 5.24: Temperature cycle considered for the sensitivity analysis of the lifetime prediction model for the case of operating stress levels.

The same analysis of the effect of the model's parameters variation on the lifetime prediction has been performed. The prediction error respect to the 20,000 hours calculated using the tuned model is shown for the case of variations of the parameter *k* and *N* in Figure 5.25 and Figure 5.26, respectively.

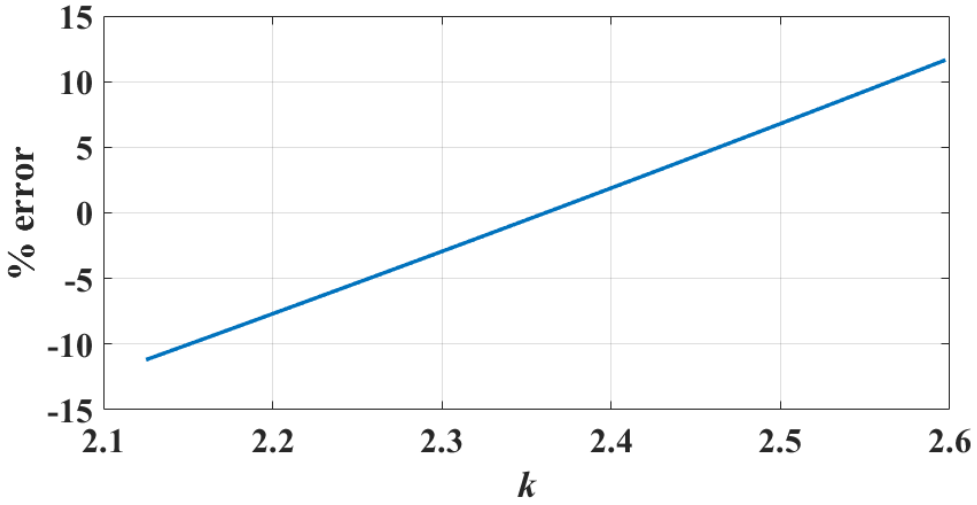


Figure 5.25: Percentage error of the lifetime prediction for different values of the parameter k respect to the lifetime calculated with the tuned parameters, for the temperature profile of Figure 5.24.

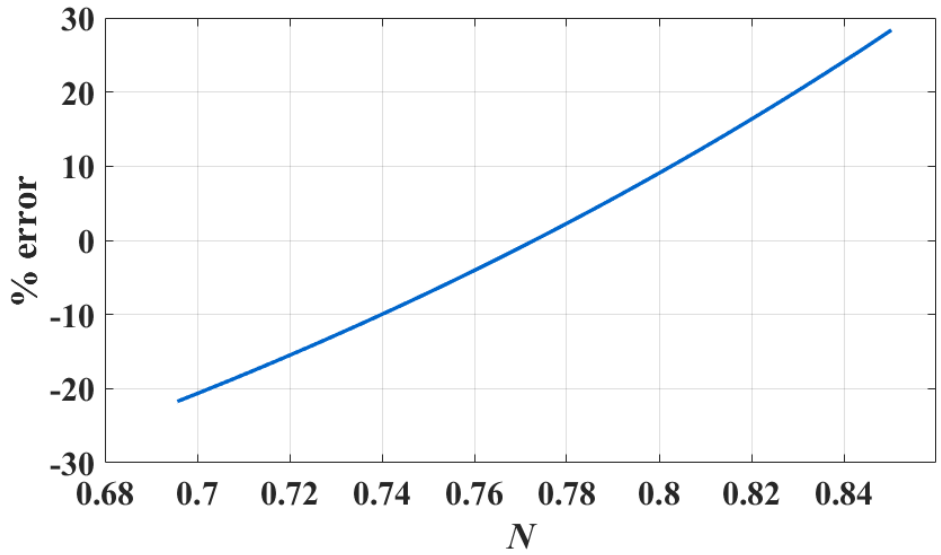


Figure 5.26: Percentage error of the lifetime prediction for different values of the parameter N respect to the lifetime calculated with the tuned parameters, for the temperature profile of Figure 5.24.

It has to be remarked that the prediction error with respect to the one calculated for the temperature profiles of the accelerated ageing tests is smaller, mainly due

to the smaller temperature time derivative. In particular, the maximum prediction error is less than 30%.

A final analysis has been conducted where the parameters k and N are simultaneously and randomly varied between -10% and +10% of their tuned value. Figure 5.27 shows the prediction error for different combination of the parameters. In the extreme cases where both the parameters k and N are underestimated by 10% of their tuned value, the lifetime prediction obtained is the 29.5% longer than the prediction obtained from the tuned model. In the opposite extreme case where the parameters are overestimated by the 10% of their tuned value, the lifetime prediction obtained is reduced by the 45% respect to the one obtained using the tuned model.

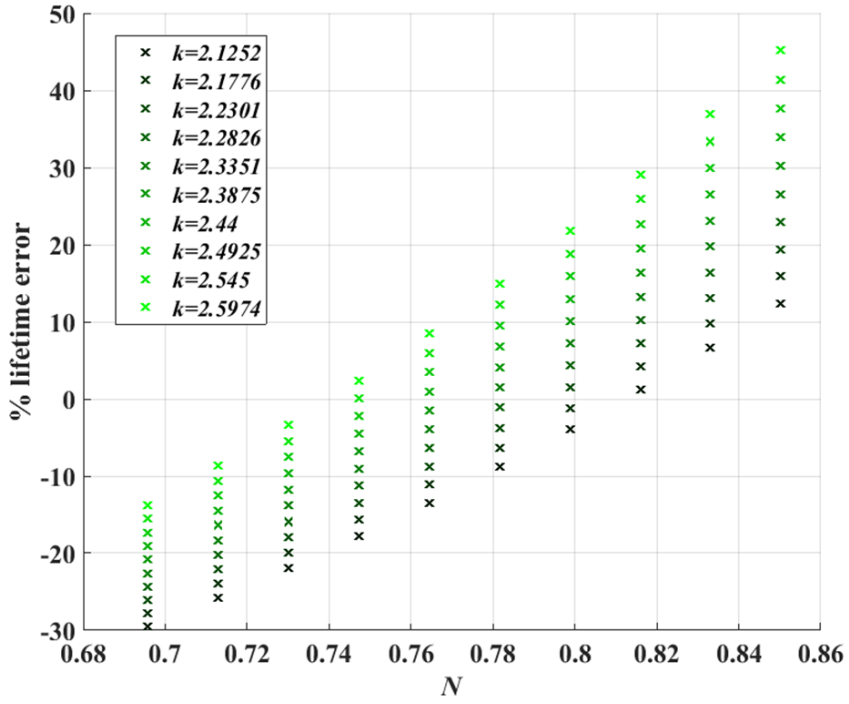


Figure 5.27: Percentage error of the lifetime prediction for different values of the parameters k and N respect to the lifetime calculated with the tuned parameters, for the temperature profile of Figure 5.24.

In this section, it has been shown that the lifetime consumption model proposed can provide fairly accurate prediction for windings under operating conditions, even in case of small errors in its tuned parameters. In order to obtain more accurate results, the accelerated tests for the tuning procedure can be conducted at lower temperatures, with the disadvantage that each test will be completed in a longer time and at a higher cost. In the next section it will be investigated how the lifetime consumption model can be utilized for analysing and improving the performance of the SMPM motor designed.

5.3 Applications of the lifetime consumption model

The analysis conducted above highlighted the importance of including the effect of thermo-mechanical stress in short time duty applications, even for small power motors, in conjunction with the thermal stress. Thus, in order to guarantee the required motor reliability, considering a maximum temperature constraint by itself is not sufficient as then only the insulation deterioration caused by thermal stress is guaranteed under control.

In this section, the flexibility and applicability of the model especially in terms of the landing gear actuation application considered in this work is explored. In particular, section 5.3.1 investigates how the maintenance scheduling of the motor can be improved by the real-time employment of the model during operation. This can lead to a general reduction of the maintenance costs. Secondly, in section 5.3.2 the model is employed for re-rating the motor designed, where the maximum winding temperature constraint is removed and the motor endurance is calculated using the lifetime model.

5.3.1 Online maintenance scheduling

The SMPM motor designed for the electro-mechanical actuation of a landing gear is a fault tolerant machine, which is composed of two sets of independent three-phase stars. A failure of one star should not jeopardise the motor's operations. In order to comply with this, the motor has been designed in such a way that in case of a failure of one star, the remaining one must be capable to safely produce the required torque. Thus, during the design stage, a careful thermal analysis of the motor and in particular of its stator windings has to be conducted in order to avoid excessive thermal stress during the emergency operations, where higher currents flow in the windings of the remaining star. In fact, depending on the operating mode, the windings temperature profile will be different, as previously shown in Figure 4.16.

In order to comply with the reliability requirements, a maximum temperature has been set for the windings temperature, equal to the windings insulation thermal index temperature. In this way, under the assumption of dominant thermal ageing for the windings insulation, the lifetime of the windings is guaranteed to be longer than the target lifetime of 20,000 hours. It follows that maintenance of the machine must be prescribed after 20,000 hours of operating time, not considering that the motor windings reach high temperatures only during emergency operating modes and not taking into account the effect of thermo-mechanical ageing.

The lifetime consumption model presented can be used as a tool for the enhancement of the motor maintenance planning. In fact, since it can provide an estimation of the life consumed for a given thermal cycle, its online

implementation would allow a more accurate prediction of when maintenance of the motor is needed in accordance with the stress levels its windings have experienced. For instance, a three phase star which have repeatedly operated in emergency mode would be signalled for maintenance earlier than a three phase star which has been always used for healthy mode operations. Thus, even in the accidental case of windings' over-temperatures, the model would provide an estimation of the life consumed during the episode. This can remove the need for unnecessary maintenance/replacing. Finally, since the motor is designed for operating at different ambient temperatures, the model would take into account also this factor, since for lower ambient temperature the calculated insulation ageing rate will be smaller.

5.3.1.1 Implementation of the model

The model can be easily implemented for online lifetime consumption estimation, by considering its iterative form as given in (5.10). In particular, if the integral function of (5.10) is approximated by using the trapezoid rule, then at each sampling time t_i, a measure of the winding lifetime remaining can be computed. This is shown in (5.18), where f is the function representing the lifetime remaining if the windings are kept at a constant temperature T_0.

$$f(t_i) = f(t_{i-1}) - \frac{t_i - t_{i-1}}{2}\left(\frac{\mathcal{L}_0}{\mathcal{L}\big(T(t_i), v(t_i)\big)} - \frac{\mathcal{L}_0}{\mathcal{L}\big(T(t_{i-1}), v(t_{i-1})\big)}\right) \quad (5.18)$$

The temperature variation v can be approximated by a backward difference approximation as in (5.19).

$$v(t_i) = \frac{T(t_i) - T(t_{i-1})}{t_i - t_{i-1}} \quad (5.19)$$

Thus, from the measurement of the winding temperature T at two consecutive sampling times, it is possible at each instant to update the measure of the remaining lifetime f by implementing (5.18-5.19). It has to be remarked that due to its iterative form, the model needs to memorize (at each sampling time) only the value of the winding temperature T and of the measure of the lifetime consumed f. Another important point is that the value of the winding temperature T is generally available either from temperature sensors placed in the motor or from online temperature prediction models.

Using (5.18), the maintenance of the motor windings can be scheduled when the value of f falls below a threshold value. At any time the value of f provides a general indication of the deterioration level of the winding insulation system. The implementation of the model allows extending the lifespan of the windings, and thus reducing the maintenance costs.

5.3.2 Motor rating using the lifetime consumption model

The IEC's Standard [51] provides a definition for rating electrical machines according to the duty cycle type. In particular, for short time duty applications, [51] defines a motor rated for a specific load over a short time period if its temperature does not exceed the thermal index temperature of its materials during the duty cycle. For this reason, during the design of the motor, the maximum winding temperature has been fixed equal to 180 °C.

However, as shown above, this definition could lead to a significant oversizing of the motor. Apart from this, it has also been shown that considering only the effects of thermal stress is not sufficient, especially for some applications where the temperature variations over the time are particularly steep. In fact, these high

temperature variations can cause significant thermo-mechanical stress levels on the winding insulation system. An important conclusion here is that, while the effects of thermal ageing can be easily controlled by setting a maximum winding temperature, however thermo-mechanical ageing is not so easily controlled. Thus, this can cause an early failure of the insulation system even if the temperature is kept under the winding thermal index temperature.

In this section, the implementation of the lifetime consumption model presented as a tool for rating the motor for a specific short time duty cycle is investigated. The constraint of maximum winding temperature is removed, whereas a more general constraint of at least 20,000 hours operating time is imposed.

As a first step, the lifetime consumption model has been implemented for the calculation of the lifespan for the windings of the designed motor, for each operating mode. In fact, since the operating modes of the motor are characterized by different winding temperature profiles, as previously shown in Figure 4.5, then their degradation rate will be different.

The operations time for each cycle is equal to 60 seconds. After operations the motor temperature decreases back to ambient temperature. Thus, there is a period after operations where the temperature is still high and the consequent insulation degradation cannot be neglected. For this reason, during the computation of the expected lifetime, the ageing during a cooling down period of other 60 seconds after the operating cycle was included in the calculation of the lifetime consumed during each cycle. The three temperature profiles considered as input of the lifetime consumption model, for the case of motor designed with the constraint

of maximum temperature equal to 180 °C, have been computed using the LPTN presented in Chapter 4 and are shown in Figure 5.28.

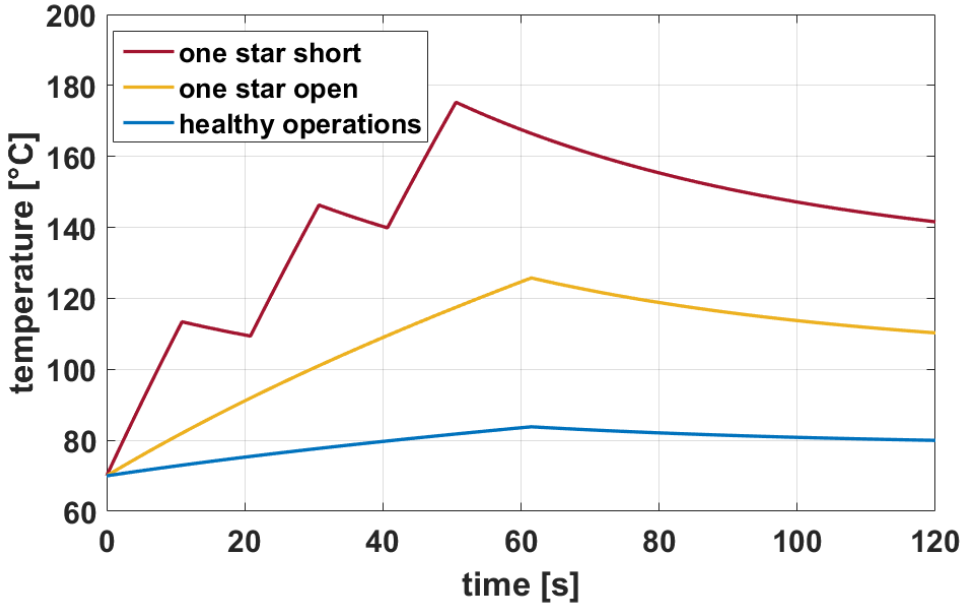


Figure 5.28: Winding temperature profiles calculated with the LPTN for the three motor operating modes.

In order to obtain an estimation of the maximum operating lifetime of the motor, each temperature profile has been used as input of the tuned lifetime consumption model. For the case of healthy operations and for the case of one star open operations, the lifetime model provided an estimated operating lifetime longer than 10^9 hours. This is due to the fact that the temperature profiles related to these two operating modes do not produce any significant stress, since the winding temperature remains well below the thermal index temperature and there are no steep temperature variations. Thus, for these operating modes it can be stated that the temperature related stresses are negligible, and the lifetime of the winding insulation system is virtually infinite.

The lifetime obtained when the temperature cycle for the case of one star shorted is used as input of the lifetime consumption model, is equal to 1.49 million hours. Thus, for each of the three operating modes, the motor predicted lifetime is much longer than the target operating lifetime of 20,000 hours. This is partially due to the constraint on the maximum allowed winding temperature.

In order to understand how restricting this constraint is, a procedure has been developed with the aim of calculating the maximum power deliverable by the motor during operations, when the constraint on the maximum winding temperature is removed and setting a more general requirement on the target lifetime duration of 20,000 hours.

Under the assumption of linear relationship between torque and i_q current, for a fixed rotor speed the relationship between the mechanical power generated and winding current can be also assumed to be linear. On the base of these assumptions, it can be stated that if for a current I_n applied to both the stars the torque produced is equal to T_n, then the same torque is produced by one star by applying twice the value of I_n when the other star is open. Similarly, twice the value of I_n plus the current necessary for compensating the braking torque of the other star is required when the latter is shorted. Thus, for a specific torque T_n, the winding current values for the three operating modes can be easily computed in the same way as it was done in Section 4.2.3.

In order to maximize the torque that the motor can produce during the three operating modes while respecting the target lifetime, both the thermal network presented in Chapter 4 and the lifetime consumption model are iteratively

employed. The strategy adopted was to select a current I_n, from which the current applied during each operating mode can be computed. Each current cycle is used as input of the thermal network for the estimation of the winding temperature profile during each operating mode. Each temperature profile is employed as input of the lifetime consumption model for predicting the lifespan of the windings under each temperature cycle considered. On the base of the obtained lifetime prediction, the current I_n is increased or decreased, and the procedure is repeated until the maximum current I_n, such that the lifetime predicted for each operating mode considered is longer than 20,000 hours, is identified.

Following this procedure, it has been found that for a winding current I_n which is 19% higher than the ones used in the original design (where only a maximum winding temperature is imposed), then the predicted winding lifetime relative to operations with one star shorted is equal to 21,500 hours. The ageing under the other two operating modes is still negligible. It follows that, if the power rating for the duty cycles is conducted by employing the lifetime consumption model, then the same motor can be qualified for delivering 19% more power while respecting the reliability constraints.

Figure 5.29 shows the temperature cycles for the maximized current I_n , obtained using the thermal network for the three operating modes considered.

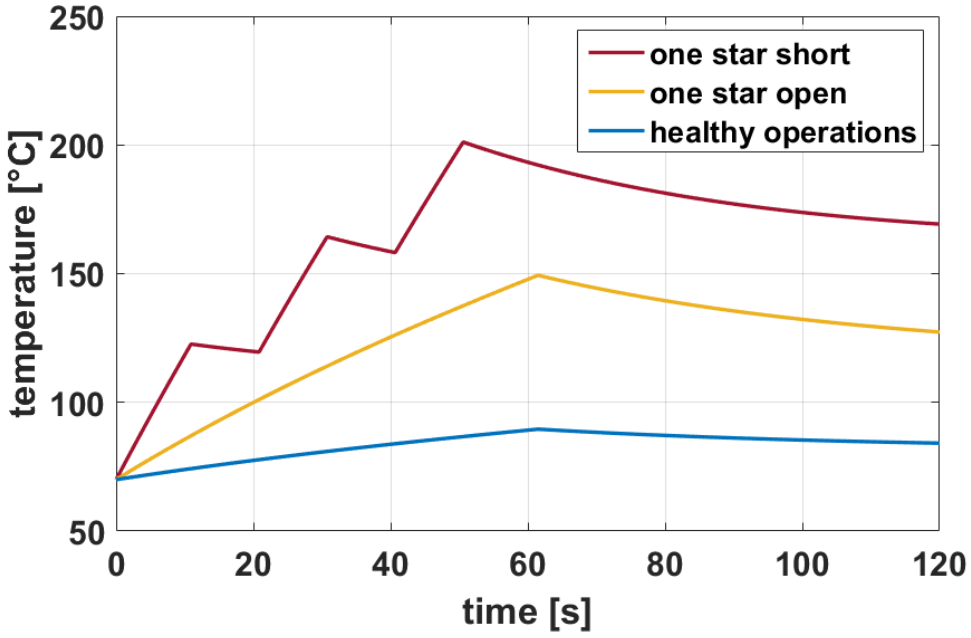


Figure 5.29: Winding temperature profiles calculated with the LPTN for the three motor operating modes for the case of motor rated for 20,000 hours lifetime.

From this analysis, it can be noticed that the emergency operating modes are the bottleneck for the motor performance. In fact, the stress levels applied to the winding insulation system during healthy operations are negligible, whereas the most demanding operation is the one when one three-phase star is shorted. However, the reliability constraint of operating lifetime equal to 20,000 hours even for the case of emergency operations could be argued being too conservative, as the motor is unlikely to operate for most of its lifespan with only one active star. For this reason, an analysis is conducted where it is evaluated how the motor power rating can be further increased if the target lifetime during emergency operations is reduced.

The analysis has been conducted by employing the same strategy adopted above, where the thermal network and the lifetime consumption model are iteratively

used with the aim of maximizing the winding current. However, in this case, the computation has been done by keeping unchanged the target lifetime equal to 20,000 hours for healthy operations, but by setting a shorter lifetime $\mathcal{L}_{em}$ for the case of emergency operations. Figure 5.30 shows the results of this analysis, where it is reported for each value of $\mathcal{L}_{em}$ the percentage increase of power respect to the power required by the application. Thus, an improvement of the motor power rating can be obtained if the reliability constraints of the emergency operations are reduced, whilst maintaining the target lifetime for healthy operations. It should be remarked that, for a fixed power rating, a reduction of $\mathcal{L}_{em}$ leads to an increase of the torque density (and thus a reduction of the motor dimensions) as a consequence of the less stringent reliability requirements.

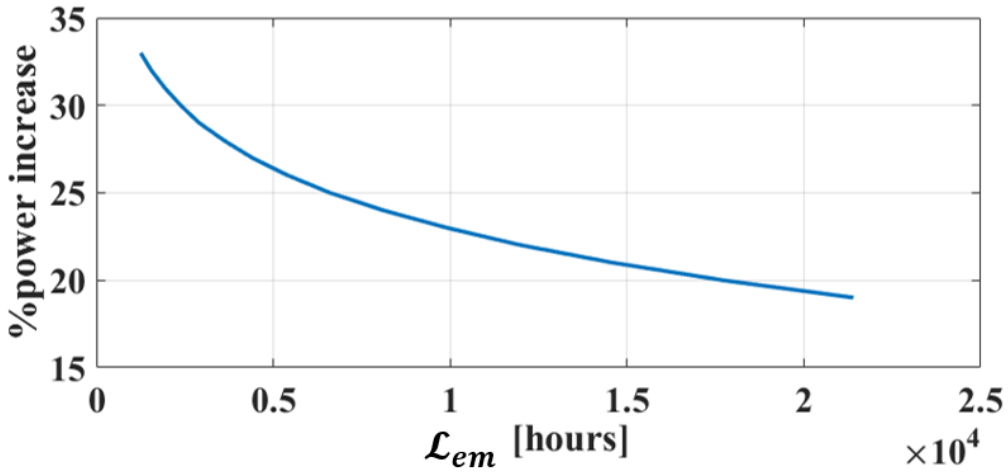


Figure 5.30: Percentage motor power rating increase for different lifetime constraints of the emergency operating modes.

5.4 Conclusions

In this Chapter, an investigation on the ageing process of the windings' insulation system of the designed motor has been conducted. The study has been

focused on applications where the dominant ageing factors are temperature related, since the motor designed in this work is a short-time duty applications which experience demanding temperature cycles.

A novel multi-stress model for the estimation of the windings' electrical insulation lifetime under thermal and thermo-mechanical stresses has been proposed. In particular, this model provides the insulation ageing rate once provided the winding temperature and winding temperature variation respect to time.

The lifetime consumption model presented needs proper tuning of some free parameters. For this reason, a tuning procedure based on the results of specific accelerated ageing tests have been presented. The ageing tests setup has been thoroughly explained. The experiment has been based on the guidelines provided by specific standards for the evaluation of the electrical insulation endurance. The results of the accelerated ageing tests allowed to highlight the importance of including the effect of thermo-mechanical stress as dominant ageing factor for short time duty applications.

The lifetime consumption model has been implemented for investigating the constraints imposed on the winding temperature during the motor design for the sake of obtaining a reliable dispositive. In particular, it has been shown that constraining the winding temperature during operations to be below the temperature index temperature of the insulation system might lead to an oversized machine. In fact, if the constraint on the maximum winding temperature is substituted by the requirement that the winding lifetime has to

endure a specific amount of operating time, than the motor can be rated for higher power levels with the aid of the proposed lifetime consumption model.

Chapter 6
Conclusions

6.1 Summary of the undertaken work

In this work, an analysis of the most critical aspects in the design of high torque density low-rate duty electrical machines has been conducted. These type of applications are of major interest in the aerospace sector, as ever-increasing performance solutions are being developed for the electro-mechanical actuation of aircraft components. As vessel to investigate the main challenges of such applications, an EMA for the deployment and retraction of a helicopter landing gear has been considered, which can be classified as short-time duty application. The main objective has been to explore the design constraints with the aim of maximizing the motor torque density, whilst guaranteeing the reliability level required.

The EMA's architecture has been defined, which includes redundant power lanes for the fault tolerance capabilities of the electrical subsystem. The results of a trade-off study, conducted for the definition of the optimal drive train and

DC-Link voltage configurations in terms of overall system weight, have been presented.

A fault tolerant 12-slots/10 pole SMPM machine has been proposed for this actuator. A structured design procedure has been presented, which takes into account the machine's behaviour during both healthy and faulty operations. A FE model has been used for the evaluation of the electromagnetic performance, whilst a LPTN model has been implemented for a thermal analysis of the motor.

Since for low-rate applications the main characteristic is that the motor does not reach a thermal equilibrium during operations, then the thermal limits of the employed materials represent one of the major constraints as opposed to the magnetic limitations. This characteristic has been exploited by maximizing the windings current density (which can be assumed proportional to the torque density) in such a way that the temperature in the slot during operations is within the thermal rating temperature of the winding's electrical insulation. Following this strategy, the thermal boundaries of the machines are fully exploited whilst the winding's insulation degradation rate is kept under control, thus guaranteeing reliability against short circuits faults. A prototype of the machine has been manufactured and experimental tests have allowed comparing the motor's performance to the models' predictions.

From an analysis of the design constraints, a main area of improvement has been identified, which is the determination of the maximum temperature cycle sustainable by the winding electrical insulation. In fact, the common strategy of constraining the maximum temperature to be below the thermal index temperature of the insulating materials might be too conservative, since high

temperatures are reached only for a short portion of the duty cycle. On the other hand, reliable models assessing the lifetime of such materials under thermal and thermo-mechanical stresses for this type of applications are not available in literature. With the aim of marking an improvement in this area, two fundamental aspects have been investigated, which are the thermal modelling of the winding temperature and the assessment of the winding insulation ageing rate under the stresses typical of such applications. Thus, in this work it has been shown that careful understanding of these aspects can lead to more efficient and reliable designs of machines for such applications.

From the experiments conducted on the prototype of the motor, a discrepancy between the experimental temperatures and the LPTN predictions was observed. This was traced back to typical uncertainties of some model parameters. Since the accuracy of the thermal model is of extreme importance for the motor performance maximization for low-rate duty applications, a novel tuning procedure has been proposed. This procedure is focused on the enhancement of the windings temperature accuracy, which represents the motor hot spot, through the implementation of an optimization SQP algorithm which minimizes the mismatch between model's predictions and experimental temperature profiles. Starting from the tuned model, a simplified analytical thermal model has been then proposed, which provides similar accuracy but sensibly lower computational cost. The model has been experimentally validated.

Windings insulation short circuits represent one of the most frequent motor failure causes. In low-rate duty applications, this is worsened by the severe temperature cycles due to the high slot current density typically employed, which

can increase the insulation ageing rate as consequence of the combined effect of thermal and thermo-mechanical stresses. Since there is no standard available for the rating of insulating materials under this ageing factors, a major part of the work has been focused on investigation of the ageing process of the windings' electrical insulation for low-rate duty motors. A series of accelerated ageing tests on samples of the employed windings have been aged through the application of specific thermal cycles. A winding lifetime consumption model has been proposed, which relates the time to failure of the winding to its temperature profile during operations. The model is tuned on the base of the results of the conducted accelerated ageing tests.

Both the analytical thermal model and the winding lifetime consumption model are valuable tools for increasing the performance of low-rate duty motors. In fact, an accurate thermal model is required for high performance machines where the thermal limits are one the most restraining constraints. The proposed winding lifetime consumption model relates the winding insulation ageing rate to the winding temperature profile, thus potentially allowing for the substitution of the maximum winding temperature design constraint with a less restrictive minimum winding insulation lifetime design constraint.

In general, both the solutions lead as a first consequence to an increase of the winding current density, and thus to a higher torque density, whilst still guaranteeing the required reliability level. In fact, the motor presented in Chapter 3, which has been designed setting the winding temperature below the thermal rating temperature of the winding insulation materials, has a torque performance of 1 Nm for a phase peak current of 1.56 A under healthy operations. Its

maximum temperature reached during emergency operations is 185.7 °C. The winding lifetime consumption model proposed in Chapter 6 shows that under such operating conditions the predicted insulation lifetime is longer than 10^9 operating hours, while the minimum lifetime required is 20,000 hours. If the maximum winding temperature constraint is removed and the winding lifetime consumption model is implemented for the maximization of the motor performance whilst respecting the reliability constraint, then for the same motor the torque performance can be increased to 1.19 Nm for a phase peak current of 1.86 A under healthy operations, obtaining a maximum temperature during emergency operations of 203 °C and a predicted winding insulation lifetime of 21,500 operating hours.

Thus, for the application considered it has been found that a 19 % increase of the torque density can be achieved through careful implementation of the winding lifetime consumption model proposed.

6.2 Major contributions to research

The major contributions to technical research developed during the course of this work are:

- a structured methodology for the design of fault tolerant SMPM machines for low-rate duty applications, which aims at maximizing the torque density and at the same time guaranteeing a certain degree of reliability.

- A tuning procedure for Lumped Parameter Thermal Network (LPTN) models based on a SQP algorithm, which sensibly increases the accuracy in the prediction of the stator winding temperature.
- A novel analytical thermal model derived from a simplification of the LPTN model, which features similar accuracy but sensibly lower computational effort respect to the original LPTN.
- An accelerated ageing test procedure developed for the investigation of the windings' electrical insulation system deterioration related to thermal and thermo-mechanical stress.
- A winding electrical insulation lifetime consumption model, tuned on the base of the accelerated ageing tests' results, is presented for the prediction of the windings' electrical insulation lifetime under temperature related stresses.

Part of the work presented in this thesis has been published in peer reviewed journals [171] and conference proceedings ([116], [158]), one of which ([116]) has also resulted in the top 20 student papers award of its respective conference.

6.3 Future works

There are several research opportunities for improvement and extension of the work presented in this thesis.

- The proposed LCC thermal model takes into account the winding Joule losses only as heat source. Although for the investigated motor this was a fair simplification because the contribution of other heat sources to the

winding temperature increase was minimal, the model could be generalized to the case where also stator iron losses are relevant.

- The winding insulation lifetime consumption model takes into account thermal and thermo-mechanical stresses. The model could be extended to the case where also electrical stress due to PD activity significantly contributes to the insulation ageing process. This requires further accelerated ageing tests where the combined stress sources are applied to samples of the winding.
- In order to further validate the results of the accelerated ageing tests conducted on the windings' specimens, equivalent ageing tests could be performed on the windings mounted in the actual motor. Moreover, the accelerated ageing tests could be replicated on windings with different insulating coating materials with the aim of generalizing the obtained results.
- Thanks to its low computational cost, it could be evaluated the implementation of the proposed analytical thermal model for the online winding temperature estimation. One of the advantages of this solution would be the reduction of the risks deriving from a temperature sensor failure.
- Also the winding lifetime consumption model could be implemented for the online estimation of the life consumed during operations, providing a valuable tool for maintenance scheduling.

- A thermal analysis of the motor mounted in the EMA could be conducted, where heat exchange between different components is included.
- The methodology presented in this thesis has been implemented for a short-time duty application. The procedure could be adapted for intermittent duty applications such as in flight control surface EMAs.

[1] C. Gerada and K. J. Bradley, "Integrated PM Machine Design for an Aircraft EMA," *IEEE Transactions on Industrial Electronics,* vol. 55, no. 9, pp. 3300-3306, 2008.

[2] P. Wheeler and S. Bozhko, "The More Electric Aircraft: Technology and challenges," *IEEE Electrification Magazine,* vol. 2, no. 4, pp. 6-12, 2014.

[3] T. Raminosoa, T. Hamiti, M. Galea and C. Gerada, "Feasibility and electromagnetic design of direct drive wheel actuator for green taxiing," in *2011 IEEE Energy Conversion Congress and Exposition*, Phoenix, AZ, 2011.

[4] M. Rottach, C. Gerada and P. W. Wheeler, "Design optimisation of a fault-tolerant PM motor drive for an aerospace actuation application," in *Power Electronics, Machines and Drives (PEMD 2014), 7th IET International Conference on,* Manchester, 2014.

[5] M. A. Valenzuela, P. V. Verbakel and J. A. Rooks, "Thermal evaluation for applying TEFC induction motors on short-time and intermittent duty cycles," *IEEE Transactions on Industry Applications,* vol. 39, no. 1, pp. 45-52, 2003.

[6] B. Sarlioglu and C. T. Morris, "More Electric Aircraft: Review, Challenges, and Opportunities for Commercial Transport Aircraft,"

IEEE Transactions on Transportation Electrification, vol. 1, no. 1, pp. 54-64, 2015.

[7] J. A. Rosero, J. A. Ortega, E. Aldabas and L. Romeral, "Moving towards a more electric aircraft," *IEEE Aerospace and Electronic Systems Magazine*, vol. 22, no. 3, pp. 3-9, 2007.

[8] J. A. Weimer, "The role of electric machines and drives in the more electric aircraft," in *Electric Machines and Drives Conference, 2003. IEMDC'03. IEEE International*, 2003.

[9] M. A. Maldonado and G. J. Korba, "Power management and distribution system for a more-electric aircraft (MADMEL)," *IEEE Aerospace and Electronic Systems Magazine*, vol. 14, no. 12, pp. 3-8, 1999.

[10] D. Barater et al., "Multistress Characterization of Fault Mechanisms in Aerospace Electric Actuators," *IEEE Transactions on Industry Applications*, vol. 53, no. 2, pp. 1106-1115, 2017.

[11] R. D. Telford, S. J. Galloway and G. M. Burt, "Evaluating the reliability & availability of more-electric aircraft power systems," in *2012 47th International Universities Power Engineering Conference (UPEC)*, London, 2012.

[12] R. I. Jones, "The More Electric Aircraft: the past and the future?," in *Electrical Machines and Systems for the More Electric Aircraft (Ref. No. 1999/180), IEE Colloquium on*, London, 1999.

[13] S. C. Jensen, G. D. Jenney and D. Dawson, “Flight test experience with an electromechanical actuator on the F-18 Systems Research Aircraft,” in *Digital Avionics Systems Conference, 2000. Proceedings. DASC. The 19th*, Philadelphia, PA, 2000.

[14] A. Boglietti, A. Cavagnino, A. Tenconi and S. Vaschetto, “The safety critical electric machines and drives in the more electric aircraft: A survey,” in *Industrial Electronics, 2009. IECON '09. 35th Annual Conference of IEEE*, Porto, 2009.

[15] J. W. Bennett, B. C. Mecrow, A. G. Jack and D. J. Atkinson, “A Prototype Electrical Actuator for Aircraft Flaps,” *IEEE Transactions on Industry Applications,* vol. 46, no. 3, pp. 915-921, 2010.

[16] M. Villani, M. Tursini, G. Fabri and L. Castellini, “High Reliability Permanent Magnet Brushless Motor Drive for Aircraft Application,” *IEEE Transactions on Industrial Electronics,* vol. 59, no. 5, pp. 2073-2081, 2012.

[17] G. Brando, A. Dannier, L. P. D. Noia, R. Rizzo and S. I. Hamasaki, “Design of a PMSM for the electric steering of the nose landing gear,” in *2016 International Symposium on Power Electronics, Electrical Drives, Automation and Motion (SPEEDAM)*, Anacapri, 2016.

[18] T. Wijekoon, L. Empringham, P. Wheeler and J. Clare, “Compact dual-output power converter for an Aerospace electrical landing gear

actuation system," in *2009 13th European Conference on Power Electronics and Applications*, Barcelona, 2009.

[19] G. Altare, A. Vacca and C. Richter, "A novel pump design for an efficient and compact Electro-Hydraulic Actuator," in *2014 IEEE Aerospace Conference*, Big Sky, MT, 2014.

[20] A. Garcia, I. Cusido, J. A. Rosero, J. A. Ortega and L. Romeral, "Reliable electro-mechanical actuators in aircraft," *IEEE Aerospace and Electronic Systems Magazine*, vol. 23, no. 8, pp. 19-25, 2008.

[21] S. E. Lyshevski, V. A. Skormin and R. D. Colgren, "High-torque density integrated electro-mechanical flight actuators," *IEEE Transactions on Aerospace and Electronic Systems*, vol. 38, no. 1, pp. 174-182, 2002.

[22] J. W. Bennett, G. J. Atkinson, B. C. Mecrow and D. J. Atkinson, "Fault-Tolerant Design Considerations and Control Strategies for Aerospace Drives," *IEEE Transactions on Industrial Electronics*, vol. 59, no. 5, pp. 2049-2058, 2012.

[23] N. Wang and Y. Zhou, "Research on reliability of a hybrid Three-Redundant Electro-Mechanical Actuator," in *2009 International Conference on Mechatronics and Automation*, Changchun, 2009.

[24] C. Gerada, K. Bradley, C. Whitley and G. Towers, "Integrated Machine design for Electro Mechanical Actuation," in *2007 IEEE International Symposium on Industrial Electronics*, Vigo, 2007.

[25] M. Christmann, S. Seemann and P. Jänker, “Innovative Approaches to Electromechanical Flight Control Actuators and Systems,” in *4th International Conference on Recent Advances in Aerospace Actuation Systems and Components*, Toulouse, France, 2010.

[26] M. Galea, C. Gerada, T. Raminosoa and P. Wheeler, “Design of a high force density tubular permanent magnet motor,” in *Electrical Machines (ICEM), 2010 XIX International Conference on*, Rome, 2010.

[27] B. C. Mecrow et al., “Design and testing of a four-phase fault-tolerant permanent-magnet machine for an engine fuel pump,” *IEEE Transactions on Energy Conversion,* vol. 19, no. 4, pp. 671-678, 2004.

[28] X. Huang, A. Goodman, C. Gerada, Y. Fang and Q. Lu, “Design of a Five-Phase Brushless DC Motor for a Safety Critical Aerospace Application,” *IEEE Transactions on Industrial Electronics,* vol. 59, no. 9, pp. 3532-3541, 2012.

[29] G. J. Atkinson, J. W. Bennett, B. C. Mecrow, D. J. Atkinson, A. G. Jack and V. Pickert, “Fault tolerant drives for aerospace applications,” in *Integrated Power Electronics Systems (CIPS), 2010 6th International Conference on*, Nuremberg, 2010.

[30] X. Jiang, W. Huang, R. Cao, Z. Hao and W. Jiang, “Electric Drive System of Dual-Winding Fault-Tolerant Permanent-Magnet Motor for

Aerospace Applications," *IEEE Transactions on Industrial Electronics,* vol. 62, no. 12, pp. 7322-7330, 2015.

[31] W. Cao, B. C. Mecrow, G. J. Atkinson, J. W. Bennett and D. J. Atkinson, "Overview of Electric Motor Technologies Used for More Electric Aircraft (MEA)," *IEEE Transactions on Industrial Electronics,* vol. 59, no. 9, pp. 3523-3531, 2012.

[32] R. Krishnan, D. Blanding, A. Bhanot, A. M. Staley and N. S. Lobo, "High reliability SRM drive system for aerospace applications," in *Industrial Electronics Society, 2003. IECON '03. The 29th Annual Conference of the IEEE,* 2003.

[33] A. G. Jack, B. C. Mecrow and J. A. Haylock, "A comparative study of permanent magnet and switched reluctance motors for high-performance fault-tolerant applications," *IEEE Transactions on Industry Applications,* vol. 32, no. 4, pp. 889-895, 1996.

[34] D. N. Brown, "Fabrication, Processing Technologies, and New Advances for RE-Fe-B Magnets," *IEEE Transactions on Magnetics,* vol. 52, no. 7, pp. 1-9, 2016.

[35] N. Bianchi, M. D. Pre, G. Grezzani and S. Bolognani, "Design considerations on fractional-slot fault-tolerant synchronous motors," in *IEEE International Conference on Electric Machines and Drives, 2005.*, San Antonio, TX, 2005.

[36] A. Mohammadpour, S. Sadeghi and L. Parsa, “A Generalized Fault-Tolerant Control Strategy for Five-Phase PM Motor Drives Considering Star, Pentagon, and Pentacle Connections of Stator Windings,” *IEEE Transactions on Industrial Electronics,* vol. 61, no. 1, pp. 63-75, 2014.

[37] G. Liu, M. Shao, W. Zhao, Q. Chen and L. Mo, “Cost Reduction of a New Fault-Tolerant Halbach Permanent Magnet Machine Using Ferrite Magnet,” *IEEE Transactions on Magnetics,* vol. 50, no. 11, pp. 1-4, 2014.

[38] J. Dong, Y. Huang, L. Jin and H. Lin, “Comparative Study of Surface-Mounted and Interior Permanent-Magnet Motors for High-Speed Applications,” *IEEE Transactions on Applied Superconductivity,* vol. 26, no. 4, pp. 1-4, 2016.

[39] G. Pellegrino, A. Vagati, P. Guglielmi and B. Boazzo, “Performance Comparison Between Surface-Mounted and Interior PM Motor Drives for Electric Vehicle Application,” *IEEE Transactions on Industrial Electronics,* vol. 59, no. 2, pp. 803-811, 2012.

[40] N. Zhao and W. Liu, “Loss Calculation and Thermal Analysis of Surface-Mounted PM Motor and Interior PM Motor,” *IEEE Transactions on Magnetics,* vol. 51, no. 11, pp. 1-4, 2015.

[41] M. Barcaro, N. Bianchi and F. Magnussen, “Analysis and Tests of a Dual Three-Phase 12-Slot 10-Pole Permanent-Magnet Motor,” *IEEE*

Transactions on Industry Applications, vol. 46, no. 6, pp. 2355-2362, 2010.

[42] A. M. El-Refaie and T. M. Jahns, "Comparison of synchronous PM machine types for wide constant-power speed range operation," in *Fourtieth IAS Annual Meeting. Conference Record of the 2005 Industry Applications Conference,* 2005.

[43] S. C. Yang, S. M. Yang and J. H. Hu, "Design Consideration on the Square-Wave Voltage Injection for Sensorless Drive of Interior Permanent-Magnet Machines," *IEEE Transactions on Industrial Electronics,* vol. 64, no. 1, pp. 159-168, 2017.

[44] W. L. Soong and T. J. E. Miller, "Field-weakening performance of brushless synchronous AC motor drives," *IEE Proceedings - Electric Power Applications,* vol. 141, no. 6, pp. 331-340, 1994.

[45] J. Cros, P. Viarouge and C. Gelinas, "Design of PM brushless motors using iron-resin composites for automotive applications," in *Industry Applications Conference, 1998. Thirty-Third IAS Annual Meeting. The 1998 IEEE,* 1998.

[46] J. Cros and P. Viarouge, "Synthesis of high performance PM motors with concentrated windings," *Energy Conversion, IEEE Transactions on,* vol. 17, pp. 248-253, 2002.

[47] L. Hao and C. S. Namuduri, “High Torque Density and Low Torque Ripple Actuator System”. US Patent US20120194040 A1, 31 Jan 2011.

[48] J. Pyrhonen, T. Jokinen and V. Hrabovcova, Design of rotating electrical machines, John Wiley & Sons, 2008.

[49] A. G. Sarigiannidis, M. E. Beniakar, P. E. Kakosimos, A. G. Kladas, L. Papini and C. Gerada, “Fault Tolerant Design of Fractional Slot Winding Permanent Magnet Aerospace Actuator,” *IEEE Transactions on Transportation Electrification,* vol. 2, no. 3, pp. 380-390, 2016.

[50] P. S. Sangha and T. Sawata, “Design and test results for dual-lane fault-tolerant PM motor for safety critical aircraft actuator,” in *2015 IEEE Energy Conversion Congress and Exposition (ECCE),* Montreal, QC, 2015.

[51] IEC, “Rotating Electrical Machines Part I: Rating and Performance,” in *60034-1,* 2010.

[52] M. Galea, C. Gerada, T. Raminosoa and P. Wheeler, “A Thermal Improvement Technique for the Phase Windings of Electrical Machines,” *IEEE Transactions on Industry Applications,* vol. 48, no. 1, pp. 79-87, 2012.

[53] V. T. Buyukdegirmenci and P. T. Krein, “Machine characterization for short-term or instantaneous torque capabilities: An approach based on

transient thermal response," in *Electric Machines & Drives Conference (IEMDC), 2013 IEEE International*, Chicago, IL, 2013.

[54] M. F. Momen and A. I. Husain, "Design and performance analysis of a switched reluctance motor for low duty cycle operation," in *Industry Applications Conference, 2004. 39th IAS Annual Meeting. Conference Record of the 2004 IEEE*, 2004.

[55] W. M. Arshad, Y. K. Chin, T. Backstrom, J. Soulard, S. Ostlund and C. Sadarangani, "On finding compact motor solutions for transient applications," in *Electric Machines and Drives Conference, 2001. IEMDC 2001. IEEE International*, Cambridge, MA, 2001.

[56] T. Munih and D. Miljavec, "A method for accelerated ageing of electric machine insulation," in *Proceedings of the 16th International Conference on Mechatronics - Mechatronika 2014*, Brno, 2014.

[57] V. I. J. Kokko, "Ageing due to thermal cycling by power regulation cycles in lifetime estimation of hydroelectric generator stator windings," in *Electrical Machines (ICEM), 2012 XXth International Conference on,*, Marseille, 2012.

[58] A. Boglietti, E. Carpaneto, M. Cossale and S. Vaschetto, "Stator-Winding Thermal Models for Short-Time Thermal Transients: Definition and Validation," *IEEE Transactions on Industrial Electronics*, vol. 63, no. 5, pp. 2713-2721, 2016.

[59] A. Boglietti, A. Cavagnino, D. Staton, M. Shanel, M. Mueller and C. Mejuto, “Evolution and Modern Approaches for Thermal Analysis of Electrical Machines,” *IEEE Transactions on Industrial Electronics*, vol. 56, no. 3, pp. 871-882, 2009.

[60] R. Wrobel, P. H. Mellor, M. Popescu and D. A. Staton, “Power Loss Analysis in Thermal Design of Permanent-Magnet Machines—A Review,” *IEEE Transactions on Industry Applications*, vol. 52, no. 2, pp. 1359-1368, 2016.

[61] R. W. Lewis, K. Morgan, H. R. Thomas and K. N. Seetharamu, The Finite Element Method in Heat Transfer Analysis, Wiley, 1996.

[62] B. M. Dinh and D. H. Linh, “Electromagnetic and thermal calculation of surface mounted permanent magnet motor using finite element method,” in *2016 IEEE International Conference on Sustainable Energy Technologies (ICSET)*, Hanoi, 2016.

[63] W. Wu, J. B. Dunlop, S. J. Collocott and B. A. Kalan, “Design optimization of a switched reluctance motor by electromagnetic and thermal finite-element analysis,” *IEEE Transactions on Magnetics*, vol. 39, no. 5, pp. 3334-3336, 2003.

[64] S. Nategh, Z. Huang, A. Krings, O. Wallmark and M. Leksell, “Thermal Modeling of Directly Cooled Electric Machines Using Lumped Parameter and Limited CFD Analysis,” *IEEE Transactions on Energy Conversion*, vol. 28, no. 4, pp. 979-990, 2013.

[65] C. Kral, A. Haumer, M. Haigis, H. Lang and H. Kapeller, “Comparison of a CFD Analysis and a Thermal Equivalent Circuit Model of a TEFC Induction Machine With Measurements,” *IEEE Transactions on Energy Conversion,* vol. 24, no. 4, pp. 809-818, 2009.

[66] J. Mugglestone, S. J. Pickering and D. Lampard, “Effect of geometric changes on the flow and heat transfer in the end region of a TEFC induction motor,” in *1999. Ninth International Conference on Electrical Machines and Drives,* Canterbury, 1999.

[67] A. Tiwari and S. Yavuzkurt, “Iterative conjugate heat transfer analysis for heat transfer enhancement of an externally cooled three-phase induction motor,” *IET Electric Power Applications,* vol. 11, no. 1, pp. 99-107, 2017.

[68] P. Mellor, D. Roberts and D. Turner, “Lumped parameter thermal model for electrical machines of TEFC design,” *Proc. Inst. Elect. Eng.,* vol. 138, no. 5, pp. 205-218, 1991.

[69] A. Tessarolo and C. Bruzzese, “Computationally Efficient Thermal Analysis of a Low-Speed High-Thrust Linear Electric Actuator With a Three-Dimensional Thermal Network Approach,” *IEEE Transactions on Industrial Electronics,* vol. 62, no. 3, pp. 1410-1420, 2015.

[70] O. Wallscheid and J. Böcker, “Global Identification of a Low-Order Lumped-Parameter Thermal Network for Permanent Magnet

Synchronous Motors," *IEEE Transactions on Energy Conversion,* vol. 31, no. 1, pp. 354-365, 2016.

[71] D. G. Dorrell, D. A. Staton, J. Kahout, D. Hawkins and M. I. McGilp, "Linked electromagnetic and thermal modelling of a permanent magnet motor," in *The 3rd IET International Conference on Power Electronics, Machines and Drives, 2006*, 2006.

[72] H. K. Yeo, H. J. Park, J. M. Seo, S. Y. Jung, J. S. Ro and H. K. Jung, "Coupled Electromagnetic-Thermal Analysis of a Surface-Mounted Permanent-Magnet Motor with Overhang Structure," *IEEE Transactions on Magnetics,* vol. PP, no. 99, 2017.

[73] G. Huang, Z. Li, Y. Yu and Z. Bu, "Finite element calculation and analysis on thermal field in flat permanent magnet linear synchronous motor," in *World Automation Congress 2012*, Puerto Vallarta, Mexico, 2012.

[74] B. Guo, Y. Huang, Y. Guo and J. Zhu, "Thermal Analysis of the Conical Rotor Motor Using LPTN With Accurate Heat Transfer Coefficients," *IEEE Transactions on Applied Superconductivity*, vol. 26, no. 7, pp. 1-7, 2016.

[75] D. Staton, A. Boglietti and A. Cavagnino, "Solving the More Difficult Aspects of Electric Motor Thermal Analysis in Small and Medium Size Industrial Induction Motors," *IEEE Transactions on Energy Conversion,* vol. 20, no. 3, pp. 620-628, 2005.

[76] D. Gerada, A. Mebarki, N. L. Brown, C. Gerada, A. Cavagnino and A. Boglietti, “High-Speed Electrical Machines: Technologies, Trends, and Developments,” *IEEE Transactions on Industrial Electronics*, vol. 61, no. 6, pp. 2946-2959, 2014.

[77] L. Idoughi, X. Mininger, F. Bouillault, L. Bernard and E. Hoang, “Thermal Model With Winding Homogenization and FIT Discretization for Stator Slot,” *IEEE Transactions on Magnetics*, vol. 47, no. 12, pp. 4822-4826, 2011.

[78] N. Simpson, R. Wrobel and P. H. Mellor, “Estimation of Equivalent Thermal Parameters of Impregnated Electrical Windings,” *IEEE Transactions on Industry Applications*, vol. 49, no. 6, pp. 2505-2515, 2013.

[79] J. P. Holman, Heat transfer, McGraw-Hill Education, 2009.

[80] T. S. Lee, “Laminar fluid convection between concentric and eccentric heated horizontal rotating cylinders for low-Prandtl-number fluids,” *International Journal for Numerical Methods in Fluids*, vol. 14, no. 9, 1992.

[81] A. B. Nachouane, A. Abdelli, G. Friedrich and S. Vivier, “Numerical approach for thermal analysis of heat transfer into a very narrow air gap of a totally enclosed permanent magnet integrated starter generator,” in *2015 IEEE Energy Conversion Congress and Exposition (ECCE)*, Montreal, QC, 2015.

[82] P. Romanazzi and D. A. Howey, “Air-gap convection in a switched reluctance machine,” in *2015 Tenth International Conference on Ecological Vehicles and Renewable Energies (EVER)*, Monte Carlo, 2015.

[83] T. D. Kefalas and A. G. Kladas, “Transient heat transfer analysis of housing and PMM using 3-D FE code,” in *2016 XXII International Conference on Electrical Machines (ICEM)*, Lausanne, 2016.

[84] M. Grabowski, K. Urbaniec, J. Wernik and K. J. Wołosz, “Numerical simulation and experimental verification of heat transfer from a finned housing of an electric motor,” *Energy Conversion and Management*, vol. 125, no. 1, pp. 91-96, 2016.

[85] D. V. d. Pol and J. Tierney, “Free Convection Heat Transfer from Vertical Fin-Arrays,” *IEEE Transactions on Parts, Hybrids, and Packaging*, vol. 10, no. 4, pp. 267-271, 1974.

[86] A. Boglietti and A. Vallan, “Measurement of Housing Thermal Resistances in Industrial Motors,” in *2006 IEEE Instrumentation and Measurement Technology Conference Proceedings*, Sorrento, 2006.

[87] A. Boglietti, A. Cavagnino and D. Staton, “Determination of Critical Parameters in Electrical Machine Thermal Models,” *IEEE Transactions on Industry Applications*, vol. 44, no. 4, pp. 1150-1159, 2008.

[88] T. Lange, F. Qi, J. Dehn and R. W. D. Doncker, “Synchronous machine model considering dynamic losses and thermal behavior,” in *2015 IEEE International Electric Machines & Drives Conference (IEMDC)*, Coeur d'Alene, ID, 2015.

[89] C. Zhang, Z. Tian, Y. Dong and S. Zhang, “Analysis of losses and thermal model in a surface-mounted permanent-magnet synchronous machine over a wide- voltage range of rated output power operation,” in *2014 IEEE Conference and Expo Transportation Electrification Asia-Pacific (ITEC Asia-Pacific)*, Beijing, 2014.

[90] Y. Da, X. Shi and M. Krishnamurthy, “Health monitoring, fault diagnosis and failure prognosis techniques for Brushless Permanent Magnet Machines,” in *2011 IEEE Vehicle Power and Propulsion Conference*, Chicago, IL, 2011.

[91] A. J. Bazurto, E. C. Quispe and R. C. Mendoza, “Causes and failures classification of industrial electric motor,” in *2016 IEEE ANDESCON*, Arequipa, 2016.

[92] G. J. Paoletti and A. Rose, “Improving existing motor protection for medium voltage motors,” *IEEE Transactions on Industry Applications*, vol. 25, no. 3, pp. 456-464, 1989.

[93] R. S. Araújo, R. A. Rodrigues, H. d. Paula, L. M. R. Baccarini and A. V. Rocha, “Premature wear and recurring bearing failures in an inverter driven induction motor — Part I: Investigation of the

problem," in *Industry Applications Society Annual Meeting, 2013 IEEE,* Lake Buena Vista, FL, 2013.

[94] J. R. Stack, T. G. Habetler and R. G. Harley, "Fault classification and fault signature production for rolling element bearings in electric machines," *IEEE Transactions on Industry Applications,* vol. 40, no. 3, pp. 735-739, 2004.

[95] A. Boudiaf, A. Djebala, H. Bendjma, A. Balaska and A. Dahane, "A summary of vibration analysis techniques for fault detection and diagnosis in bearing," in *2016 8th International Conference on Modelling, Identification and Control (ICMIC),* Algiers, 2016.

[96] R. R. Schoen, T. G. Habetler, F. Kamran and R. G. Bartfield, "Motor bearing damage detection using stator current monitoring," *IEEE Transactions on Industry Applications,* vol. 31, no. 6, pp. 1274-1279, 1995.

[97] W. Zhou, B. Lu, T. G. Habetler and R. G. Harley, "Incipient Bearing Fault Detection via Motor Stator Current Noise Cancellation Using Wiener Filter," *IEEE Transactions on Industry Applications,* vol. 45, no. 4, pp. 1309-1317, 2009.

[98] S. Nandi, H. A. Toliyat and X. Li, "Condition monitoring and fault diagnosis of electrical motors-a review," *IEEE Transactions on Energy Conversion,* vol. 20, no. 4, pp. 719-729, 2005.

[99] J. H. Dymond, N. Stranges, K. Younsi and J. E. Hayward, “Stator winding failures: contamination, surface discharge, tracking,” *IEEE Transactions on Industry Applications,* vol. 38, no. 2, pp. 577-583, 2002.

[100] S. J. Williamson, R. Wrobel, J. D. Booker, J. Yon and P. H. Mellor, “Effects of insulation ageing on the conductive heat transfer from the winding body into machine periphery/stator core pack,” in *8th IET International Conference on Power Electronics, Machines and Drives (PEMD 2016),* Glasgow, 2016.

[101] K. N. Gyftakis, M. Sumislawska, D. F. Kavanagh, D. A. Howey and M. McCulloch, “Dielectric characteristics of electric vehicle traction motor winding insulation under thermal ageing,” *IEEE Transactions on Industry Applications,* vol. 52, no. 2, pp. 1398-1404, 2016.

[102] V. I. J. Kokko, “Ageing due to thermal cycling by start and stop cycles in lifetime estimation of hydroelectric generator stator windings,” in *Electric Machines & Drives Conference (IEMDC), 2011 IEEE International,* 2011.

[103] M. Kaufhold, H. Aninger, M. Berth, J. Speck and M. Eberhardt, “Electrical stress and failure mechanism of the winding insulation in PWM-inverter-fed low-voltage induction motors,” *IEEE Transactions on Industrial Electronics,* vol. 47, no. 2, pp. 396-402, 2000.

[104] P. Bidan, T. Lebey and G. Montseny, “Transient voltage distribution in motor winding fed by inverter: experimental study and modelling,” *IEEE Trans. Power Electronics,* vol. 16, no. 1, pp. 92-100, 2001.

[105] M. Tozzi, G. C. Montanari, D. Fabiani, A. Cavallini and G. Gao, “Off-Line and On-Line PD Measurements on Induction Motors Fed by Power Electronic Impulses,” in *IEEE Electr. Insul. Conf. (EIC),* Quebec, Canada, 2009.

[106] T. Billard, T. Lebey and F. Fresnet, “Partial discharge in electric motor fed by a PWM inverter: off-line and on-line detection,” *IEEE Transactions on Dielectrics and Electrical Insulation,* vol. 21, no. 3, pp. 1235-1242, 2014.

[107] W. Tong, Mechanical Design of Electric Motors, Boca Raton, FL: CRC Press, 2014.

[108] A. H. Bonnett, “A comparison between insulation systems available for PWM-inverter-fed motors,” *IEEE Transactions on Industry Applications,* vol. 33, no. 5, pp. 1331-1341, 1997.

[109] IEEE, “IEEE Standard Test Procedure for Thermal Evaluation of Systems of Insulating Materials for Random-Wound AC Electric Machinery,” in *IEEE Std 117-2015 (Revision of IEEE Std 117-1974),* 2016.

[110] T. Wakimoto, H. Kojima and N. Hayakawa, “Measurement and evaluation of partial discharge inception voltage for enameled

rectangular wires under AC voltage," *IEEE Transactions on Dielectrics and Electrical Insulation,* vol. 23, no. 6, pp. 3566-3574, 2016.

[111] T. Weege, "Basic impregnation techniques [for windings]," in *Electrical Insulation Conference and Electrical Manufacturing and Coil Winding Conference*, Rosemont, IL, 1997.

[112] S. Yang, "On-line turn fault detection of interior permanent magnet machines using the pulsating-type voltage injection," *IEEE Trans. Ind. Appl.,* vol. 52, no. 3, p. 2340–2349, 2016.

[113] F. Briz, M. W. Degner, A. Zamarron and J. M. Guerrero, "Online stator winding fault diagnosis in inverter-fed AC machines using high-frequency signal injection," *IEEE Transactions on Industry Applications,* vol. 39, no. 4, pp. 1109-1117, 2003.

[114] Q. Wu and S. Nandi, "Fast Single-Turn Sensitive Stator Interturn Fault Detection of Induction Machines Based on Positive- and Negative-Sequence Third Harmonic Components of Line Currents," *IEEE Transactions on Industry Applications,* vol. 46, no. 3, pp. 974-983, 2010.

[115] R. M. Tallam et al., "A Survey of Methods for Detection of Stator-Related Faults in Induction Machines," *IEEE Transactions on Industry Applications,* vol. 43, no. 4, pp. 920-933, 2007.

[116] C. Sciascera, P. Giangrande, C. Brunson, M. Galea and C. Gerada, "Optimal design of an electro-mechanical actuator for aerospace application," in *IECON 2015 - 41st Annual Conference of the IEEE Industrial Electronics Society*, Yokohama, 2015.

[117] J. A. Tapia, J. Pyrhonen, J. Puranen, P. Lindh and S. Nyman, "Optimal Design of Large Permanent Magnet Synchronous Generators," *IEEE Transactions on Magnetics,* vol. 49, no. 1, pp. 642-650, 2013.

[118] J. R. Hendershot and T. J. E. Miller, Design of Brushless Permanent-magnet Machines, Motor Design Books, 2010.

[119] R. H. Park, "Two-Reaction Theory of Synchronous Machines: Generalized Method of Analysis - Part I," *Transactions of the AIEE*, vol. 48, p. 716–730, 1929.

[120] M. Barcaro, N. Bianchi, E. Fornasiero and F. Magnussen, "Experimental comparison between two fault-tolerant fractional-slot multiphase PM motor drives," in *2010 IEEE International Symposium on Industrial Electronics*, Bari, 2010.

[121] B. Mecrow, A. Jack, J. Haylock and J. Coles, "Fault-Tolerant Permanent Magnet Machine Drives," *IEE Proceedings – Electric Power Applications,* vol. 143, no. 6, p. 437 – 442, 1996.

[122] P. Arumugam, "Design Optimization on Conductor Placement in the Slot of Permanent Magnet Machines to Restrict Turn–Turn Short-

Circuit Fault Current," *IEEE Transactions on Magnetics,* vol. 52, no. 5, pp. 1-8, 2016.

[123] IEC, "Electrical insulating materials – Properties of thermal endurance - Part 1: Ageing procedures and evaluation of test results," in *60216-1,* ed. 2001.

[124] P. E. Kakosimos, A. G. Sarigiannidis, M. E. Beniakar, A. G. Kladas and C. Gerada, "Induction Motors Versus Permanent-Magnet Actuators for Aerospace Applications," *Industrial Electronics, IEEE Transactions on,* vol. 61, pp. 4315-4325, 2014.

[125] Q. A. Acton, Advances in ecology environment and conservation research and application, Atlanta, Georgia: ScholarlyEditions, 2011.

[126] A. O. Di Tommaso, F. Genduso, R. Miceli and C. Nevoloso, "Fast procedure for the calculation of maximum slot filling factors in electrical machines," in *Twelfth International Conference on Ecological Vehicles and Renewable Energies (EVER),* Monte Carlo, 2017.

[127] P. Zhang, D. M. Ionel and N. A. O. Demerdash, "Saliency Ratio and Power Factor of IPM Motors With Distributed Windings Optimally Designed for High Efficiency and Low-Cost Applications," *IEEE Transactions on Industry Applications,* vol. 52, no. 6, pp. 4730-4739, 2016.

[128] Z. Zhang, Y. Wang, Y. Sang and L. Yu, “Efficiency Improvement and Thermal Analysis of a Totally Enclosed Self-Cooling Doubly Salient Generator With Optimized Stator Yoke,” *IEEE Transactions on Magnetics*, vol. 52, no. 7, pp. 1-5, 2016.

[129] A. M. El-Refaie, T. M. Jahns and D. W. Novotny, “Analysis of surface permanent magnet machines with fractional-slot concentrated windings,” *IEEE Transactions on Energy Conversion,* vol. 21, no. 1, pp. 34-43, 2006.

[130] N. Bianchi, M. D. Pre and S. Bolognani, “Design of a fault-tolerant IPM motor for electric power steering,” *IEEE Transactions on Vehicular Technology*, vol. 55, no. 4, pp. 1102-1111, 2006.

[131] M. Rottach, C. Gerada, T. Hamiti and P. W. Wheeler, “Fault tolerant electrical machine design within a Rotorcraft Actuation Drive System optimisation,” in *Power Electronics, Machines and Drives (PEMD 2012), 6th IET International Conference on,* 2012.

[132] A. Boglietti, A. Cavagnino, M. Lazzari and M. Pastorelli, “A simplified thermal model for variable-speed self-cooled industrial induction motor,” *IEEE Transactions on Industry Applications,* vol. 39, no. 4, pp. 945-952, 2003.

[133] P. R. N. Childs. and C. A. Long, “Review of Forced Convective Heat Transfer in Stationary and Rotating Annuli,” *Proc. IMechE C: Mech. Eng. Sci.,* vol. 210, pp. 123-134, 1996.

[134] F. Ahmed, E. Ghosh and N. C. Kar, “Transient thermal analysis of a copper rotor induction motor using a lumped parameter temperature network model,” in *IEEE Transportation Electrification Conference and Expo (ITEC),* Dearborn, MI, 2016.

[135] M. Popescu, D. G. Dorrell, L. Alberti, N. Bianchi, D. A. Staton and D. Hawkins, “Thermal Analysis of Duplex Three-Phase Induction Motor Under Fault Operating Conditions,” *IEEE Transactions on Industry Applications,* vol. 49, no. 4, pp. 1523-1530, 2013.

[136] H. Igarashi, “Semi-Analytical Approach for Finite-Element Analysis of Multi-Turn Coil Considering Skin and Proximity Effects,” *IEEE Transactions on Magnetics,* vol. 53, no. 1, pp. 1-7, 2017.

[137] J. Nocedal and S. J. Wright, Numerical Optimization, Second Edition, Springer Verlag, 2006.

[138] S. Küttler, K. E. K. Benkara, G. Friedrich, F. Vangraefschèpe and A. Abdelli, “Impact of the field weakening on the iron losses in the stator of an internal permanent magnet synchronous machine,” in *2014 IEEE Energy Conversion Congress and Exposition (ECCE),* Pittsburgh, PA, 2014.

[139] S. Trujillo and M. Cutkosky, “Thermally constrained motor operation for a climbing robot,” in *2009 IEEE International Conference on Robotics and Automation,* Kobe, 2009.

[140] IEC, “Rotating electrical machines Part 18-21: Functional evaluation of insulation systems- Test procedures for wire-wound windings – Thermal evaluation and classification,” in *60034-18-21*, ed. 2013.

[141] IEC, “Rotating electrical machines Part 18-34: Functional evaluation of insulation systems - Test procedures for form-wound windings - Evaluation of thermomechanical endurance of insulation systems,” in *60034-18-34*, 2012.

[142] N. Lahoud, J. Faucher, D. Malec and P. Maussion, “Electrical ageing modeling of the insulation of low voltage rotating machines fed by inverters with the design of experiments (DoE) method,” in *8th IEEE Symposium on Diagnostics for Electrical Machines, Power Electronics & Drives*, Bologna, 2011.

[143] H. Z. Ding, “Electrodamage mechanics of dielectric ageing,” *Proceedings of the 7th International Conference on Properties and Applications of Dielectric Materials (Cat. No.03CH37417),* vol. 1, pp. 377-380, 2003.

[144] L. Xuezhong and e. al., “Evaluation method of insulation system for wind turbine generator based on accelerated multi-factor ageing test,” in *2013 Annual Report Conference on Electrical Insulation and Dielectric Phenomena*, Shenzhen, 2013.

[145] L. Simoni, “A General Approach to the Endurance of Electrical Insulation under Temperature and Voltage,” *IEEE Transactions on Electrical Insulation,* Vols. EI-16, no. 4, pp. 277-289, 1981.

[146] T. W. Dakin, “Electrical Insulation Deterioration Treated as a Chemical Rate Phenomenon,” *American Institute of Electrical Engineers, Transactions of the,* vol. 67, pp. 113-122, 1948.

[147] P. Cygan and J. R. Laghari, “Models for insulation aging under electrical and thermal multistress,” *IEEE Transactions on Electrical Insulation,* vol. 25, no. 5, pp. 923-934, 1990.

[148] T. S. Ramu, “On the Estimation of Life of Power Apparatus Insulation Under Combined Electrical and Thermal Stress,” *IEEE Transactions on Electrical Insulation,* Vols. EI-20, no. 1, pp. 70-78, 1985.

[149] M. B. Srinivas and T. S. Ramu, “Multifactor aging of HV generator stator insulation including mechanical vibrations,” *IEEE Transactions on Electrical Insulation,* vol. 27, no. 5, pp. 1009-1021, 1992.

[150] Z. Huang, A. Reinap and M. Alaküla, “Degradation and fatigue of epoxy impregnated traction motors due to thermal and thermal induced mechanical stress - part II: Thermal mechanical simulation of multiple wires due to evenly and unevenly distributed temperature,” in *8th IET International Conference on Power Electronics, Machines and Drives (PEMD 2016),* Glasgow, 2016.

[151] G. C. Stone, I. Culbert, E. A. Boulter and H. Dhirani, Stator Winding Insulation Systems in Current Use in Electrical Insulation for Rotating Machines:Design, Evaluation, Aging, Testing, and Repair, Wiley-IEEE Press, 2014.

[152] G. C. Montanari and L. Simoni, "Aging phenomenology and modeling," *IEEE Transactions on Electrical Insulation*, vol. 28, no. 5, pp. 755-776, 1993.

[153] Y. Cui, G. Wu, K. Cao and Y. Luo, "Life models of polyimide film under combined thermal and electrical stresses used in inverter-fed traction motor," in *2011 Annual Report Conference on Electrical Insulation and Dielectric Phenomena*, Cancun, 2011.

[154] R. Liang and e. al., "Determination of thermal and thermo-mechanical stresses in stator insulation of wind turbine generator based on online monitoring temperatures," in *2016 IEEE International Conference on Dielectrics (ICD)*, Montpellier, 2016.

[155] W. McDermid, "Experience with thermal cycling of stator coils and bars," in *Conference Record of the 2006 IEEE International Symposium on Electrical Insulation*, Toronto, Ont., 2006.

[156] Z. Huang, A. Reinap and M. Alaküla, "Degradation and fatigue of epoxy impregnated traction motors due to thermal and thermal induced mechanical stress - part I: Thermal mechanical simulation of single wire due to evenly distributed temperature," in *8th IET International*

Conference on Power Electronics, Machines and Drives (PEMD 2016), Glasgow, 2016.

[157] I. Y. Braslavsky, V. P. Metelkov, S. Valtchev, D. V. Esaulkova, A. V. Kostylev and A. V. Kirillov, "Some aspects of the reliability increasing of the transport electric drives," in *2016 IEEE International Power Electronics and Motion Control Conference (PEMC)*, Varna, 2016.

[158] C. Sciascera, M. Galea, P. Giangrande and C. Gerada, "Lifetime consumption and degradation analysis of the winding insulation of electrical machines," in *8th IET International Conference on Power Electronics, Machines and Drives (PEMD 2016)*, Glasgow, 2016.

[159] W. B. Nelson, Accelerated Testing: Statistical Models, Test Plans, and Data Analysis, Wiley-Interscience, 1990.

[160] L. Lefebre, G. Mazzanti and L. Simoni, "Critical examination of the life models for electrical insulation under combined stresses in the light of the boundary conditions," in *Proceedings of the 4th International Conference on Conduction and Breakdown in Solid Dielectrics*, Sestri Levante, 1992.

[161] W. Nelson, "Analysis of Accelerated Life Test Data - Part II: Numerical Methods and Test Planning," *IEEE Transactions on Electrical Insulation,* Vols. EI-7, no. 1, pp. 36-55, 1972.

[162] A. G. Levit, O. N. Grechko and N. P. Shchipunova, "Allowance for insulation ageing in the new concept of accelerated life tests of high-

voltage power transformers," *IEEE Transactions on Power Delivery,* vol. 7, no. 3, pp. 1089-1096, 1992.

[163] IEC, "Guide for the statistical analysis of ageing test data Part 1: Methods based on mean values of normally distributed test results," in *60493-1,* ed. 2011.

[164] H. Zhu, C. Morton and S. Cherukupalli, "Quality evaluation of stator coils and bars under thermal cycling stress," in *Conference Record of the 2006 IEEE International Symposium on Electrical Insulation,* Toronto, Ont., 2006.

[165] M. Istad, M. Runde and A. Nysveen, "A Review of Results From Thermal Cycling Tests of Hydrogenerator Stator Windings," *IEEE Transactions on Energy Conversion,* vol. 26, no. 3, pp. 890-903, 2011.

[166] G. C. Stone, "Recent important changes in IEEE motor and generator winding insulation diagnostic testing standards," *IEEE Transactions on Industry Applications,* vol. 41, no. 1, pp. 91-100, 2005.

[167] T. Dang and N. Sainato, "NEMA and IEC Standards: A Practical Approach," *IEEE Transactions on Industry Applications,* vol. 50, no. 5, pp. 3079-3085, 2014.

[168] IEEE, "IEEE Recommended Practice for Thermal Cycle Testing of Form-Wound Stator Bars and Coils for Large Rotating Machines," in *IEEE Std 1310-2012 (Revision of IEEE Std 1310-1996),* 2012.

[169] IEC, “Rotating electrical machines Part 18-32: Functional evaluation of insulation systems - Test procedures for form-wound windings - Evaluation by electrical endurance,” in *60034-18-32*, 2010.

[170] S. Essex, “MAGNEBOND CB-180,” [Online]. Available: http://www.spsx.com/uploadedFiles/Europe/Essex_Nexans/magnebond%20cb%20180.pdf.

[171] C. Sciascera, P. Giangrande, L. Papini, C. Gerada and M. Galea, “Analytical Thermal Model for Fast Stator Winding Temperature Prediction,” *IEEE Transactions on Industrial Electronics*, vol. 64, no. 8, 2017.